The Effect of the Internal Layout of Hydrogen Combustion Blended Wing Body Concepts on Performance

G.J.A. di Summa

Delft University of Technology

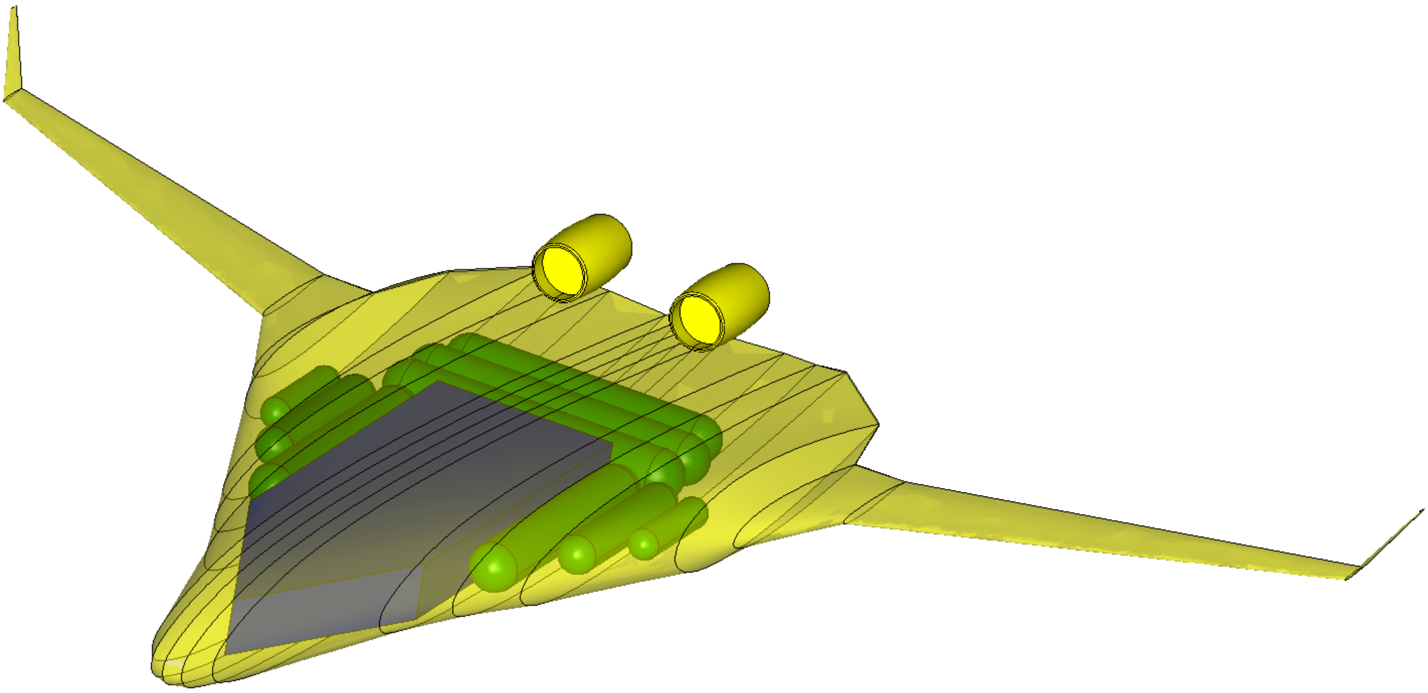

TUDelft

The Effect of the Internal Layout of Hydrogen Combustion Blended Wing Body Concepts on Performance

by

G.J.A. di Summa

to obtain the degree of Master of Science
in Aerospace Engineering

at the Delft University of Technology,
to be defended publicly on Tuesday June 10, 2025 at 10:30 AM.

Student Number:	4654870	
Supervisors:	Dr. ir. F. Oliviero	Delft University of Technology
	W. Lammen	Royal Netherlands Aerospace Centre
Thesis committee:	Dr. ir. M. Hoogreef,	Delft University of Technology, chair
	Dr. F. Oliviero	Delft University of Technology
	Ir. P. Roling,	Delft University of Technology
	W. Lammen	Royal Netherlands Aerospace Centre

Cover: Liquid Hydrogen Blended Wing Body Render Created in ParaPy

An electronic version of this thesis is available at `http://repository.tudelft.nl/`.

TU Delft

Preface

This thesis, conducted at the NLR, concludes my time as a student at the Delft University of Technology. It was a time of hard work, struggles, a lot of learning opportunities but above all, a time I thoroughly enjoyed. I would like to take this opportunity to sincerely thank my supervisors, Fabrizio Oliviero and Wim Lammen, for their support and guidance during my thesis project. During update meetings Fabrizio Oliviero gave hard but fair feedback which pushed me to improve my work, which I am grateful for. I also highly appreciate the lengthy discussions I have had with Wim Lammen, my supervisor at the NLR, which provided me with very useful insights. I would also like to thank the friends I made at the AeroDelft student team. The countless coffee breaks and study sessions together pulled me through my masters degree. My time studying would definitely have been a lot more boring if it wasn't for you guys. Not only my friends in Delft pulled me through, but my friends at home also did by offering a place to recharge and refresh. Lastly, I would like to thank my parents and brother for always supporting me, dealing with my frustrations and for doing everything to make things easier for me. Without their love and care it would not have been possible to achieve this.

Gianni di Summa
Delft, May 2025

Abstract

Long haul flights cause over half of total yearly aviation carbon emissions, while only accounting for 6 % of yearly flights. The Royal Netherlands Aerospace Centre (NLR) is researching radical aircraft configurations with novel propulsion technologies, one of which is liquid hydrogen combustion blended wing body aircraft. The goal of this thesis is to research the effect of the internal layout of long range hydrogen combustion blended wing body concepts on their aircraft level performance. The internal layout consists of the cabin design and placement of the hydrogen tanks with respect to the cabin. This thesis includes the creation of a conceptual design tool, evaluation of the concepts with optimal aircraft level performance, effects of top level requirements on the concept performance and a sensitivity analysis of the performance metrics to the design inputs. The aircraft level performance metrics that are considered are the operational empty mass, cruise L/D ratio, maximum L/D ratio, fuel mass and the static margin.

A conceptual design tool is created using the ParaPy package for Python. The tool includes analysis models and methods to evaluate the performance of the concepts. The fidelity of those analysis models and methods allows for a computationally efficient evaluation of the concepts, while maintaining sufficient accuracy for the purpose of the design tool. Limitations with respect to the aerodynamic analysis model are found, which stem from inaccuracies in the wave drag estimation. These limitations arise at high Mach numbers (> 0.85) and high lift coefficients (> 0.3). Limitations with respect to the structural weight estimations are also found.

The internal layout depends on the cabin exit option and hydrogen tank placement with respect to the cabin. The exit options are option 1 (additional leading edge doors, no rear doors), option 2 (ventral exits at the rear) or option 3 (maximum length constraint, no rear doors). The cabin can then have a different number of spanwise bays, which defines the geometry of the cabin.

The concepts with the minimum fuel burn for two considered design ranges and payloads are found to be concepts with 3 cabin bays and between 40 and 45 % of the hydrogen fuel placed next to the cabin. The considered design ranges and payloads are: 350 passengers and a range of 10 000 km and 250 passengers and a range of 7000 km. Exit options 1 and 2 result in the best fuel burn, while exit option 3 resulted in a higher fuel burn compared to the other two options for both design points. For the 350 passenger concepts exit option 3 resulted in a 3.6 % higher fuel burn, for the 250 passenger the fuel burn difference is 1.3 %. The 250 passenger concepts have a smaller spread in fuel burn, indicating the internal layout has a smaller effect on performance for these concepts. The differences in maximum L/D are small, with a maximum difference between the optimal designs for each cabin option being 2 %. The differences in OEM are higher, with the maximum difference being 8.4 %.

The cruise conditions of the concepts are optimised, after which the optimal concepts for each exit option are compared. For the 350 passenger concepts a reduction in fuel burn of around 10 % is observed for all three optimal cabin option concepts. For the 250 passenger concepts this reduction is slightly less than 20 %. The model presents limitations in terms of the effects of flying at different cruise conditions, however it is expected that optimising the cruise conditions for 250 passenger concepts results in larger fuel burn reductions compared to the 350 passenger concepts.

In the sensitivity analysis it is found the cabin leading edge sweep angle (which also defines the transition region sweep) and ratio of the fuel placed next to or behind the cabin have the largest effect on the performance metrics. The wave drag estimation method used in this work reduces the certainty of the conclusions that are drawn with respect to those parameters.

Contents

Abstract ii

List of Figures v

List of Tables viii

Nomenclature ix

1 Introduction 1
1.1 Motivation 1
1.2 Research Scope, Objective and Questions 2

2 Literature Review 3
2.1 BWB Concept 3
2.1.1 Flying Wings 3
2.1.2 Boeing Baseline BWB-450 4
2.1.3 Other Concepts 6
2.2 LH2 In Aircraft 8
2.2.1 LH2 Storage 8
2.2.2 LH2 Combustion 10
2.3 Previous Work on LH2 BWBs 13
2.3.1 Top Level Requirements of Considered Studies 13
2.3.2 Findings of LH2 BWB Studies 13
2.3.3 Comparison of Different Studies 19
2.4 BWB Modelling Aspects 20
2.4.1 Aerodynamic Models 21
2.4.2 Structural Mass Models 25
2.4.3 Propulsion Models 25
2.4.4 Tank Sizing and Internal Layout Models 25
2.4.5 Mission Analysis Models 27
2.4.6 Weight and Balance 28

3 Methodology 29
3.1 Parametric Model Framework 29
3.2 Preliminary Sizing 30
3.2.1 Class 1 Weight Estimation 30
3.2.2 Constraint Analysis 32
3.3 BWB Geometry Definition 35
3.3.1 Cabin Sizing and Exit Design 35
3.3.2 Geometry Parameterisation 37
3.3.3 Baseline External Geometry 38
3.3.4 Fuel Tank and Airfoil Fitting 39
3.4 Aerodynamic Analysis Model 43
3.4.1 Pressure Forces 43
3.4.2 Drag Components 43
3.4.3 Optimal Lift Coefficient Estimate 45
3.5 Liquid Hydrogen Tank Sizing 46
3.5.1 Structural Sizing 47
3.5.2 Thermal Sizing 47

3.6 Engine Sizing . . . 50
3.7 Component Weight Estimation . . . 51
3.7.1 Centerbody and Aft Body Weight . . . 51
3.7.2 Outer Wing Weight . . . 53
3.7.3 Center of Gravity Estimation. . . . 53
3.8 Stability Analysis . . . 54
3.9 Concept Optimisation . . . 54
3.9.1 Planform Optimisation 350 Passengers . . . 55
3.9.2 Planform Optimisation 250 Passengers . . . 57
3.9.3 Cruise Conditions Optimisation. . . . 58
3.10 Summary of Assumptions . . . 58

4 Verification & Validation 60
4.1 Verification . . . 60
4.2 Validation . . . 64

5 Results & Discussions 71
5.1 Sensitivity Analysis . . . 71
5.1.1 Baseline Designs for Sensitivity Analysis . . . 71
5.1.2 Planform Sensitivity . . . 73
5.1.3 Twist Angle Sensitivity . . . 77
5.1.4 Cruise Conditions Sensitivity . . . 79
5.1.5 Gravimetric Efficiency Sensitivity . . . 81
5.2 Planform Optimisation . . . 82
5.2.1 350 Passenger TLR Point . . . 82
5.2.2 250 Passenger TLR Point . . . 86
5.3 Cruise Conditions Optimisation . . . 89
5.3.1 350 Passengers TLR Point . . . 89
5.3.2 250 Passenger TLR Point . . . 92

6 Conclusions & Recommendations 96
6.1 Conclusions. . . . 96
6.2 Recommendations . . . 98

Bibliography 100

A Additional Sensitivity Analysis Results 106

List of Figures

1.1 Estimated aviation CO_2 emissions between 2005 and 2050 1

2.1 The Horten 229 in flight 3
2.2 The Northrop XB-35 flying wing 4
2.3 The Northrop jet powered YB-49 flying wing 4
2.4 The Northrop B-2 Spirit heavy bomber 4
2.5 Second generation 800 passenger BWB concept 5
2.6 Boeing baseline BWB-450 concept 5
2.7 The VELA BWB design 6
2.8 The SAX-40 BWB design 7
2.9 The ACFA 2020 BWB design 7
2.10 Energy usage of a conventional aircraft powered by hydrogen, relative to kerosene for different ranges and gravimetric efficiencies 8
2.11 Gravimetric efficiency and energy density of various hydrogen tanks 9
2.12 Flame temperature of kerosene and hydrogen combustion at different equivalence ratios . 11
2.13 NO_x emissions for kerosene and hydrogen combustion, with and without mixing 11
2.14 Change in TSFC of hydrogen temperature, compared to a temperature of 25K 12
2.15 Scaled planform comparison of kerosene and LH_2 BWBs 15
2.16 Absolute planform comparison of kerosene (black) and LH_2 (blue) BWBs 15
2.17 Planforms of kerosene and LH_2 BWBs 16
2.18 Aircraft energy consumption vs LH_2 tank gravimetric efficiency 16
2.19 LH_2 designs for different passenger capacities 17
2.20 Energy consumption of different BWB aircraft designs for a span of ranges 17
2.21 ONERA hydrogen BWB concept 18
2.22 Energy efficiency vs gravimetric index for ONERA hydrogen aircraft 19
2.23 Relative energy efficiency vs gravimetric index for ONERA hydrogen aircraft, compared to kerosene reference aircraft 19
2.24 BWB concept drag polars, from wind tunnel tests and CFD 22
2.25 Computed pressure distributions of SAX-29 concept at a Mach number of 0.8 23
2.26 Aerodynamic characteristics of BWB computed by a high fidelity CFD (ADFlow) analysis and low fidelity aerodynamic model 24
2.27 Drag polar of the SMILE BWB concept computed by a low fidelity aerodynamic model and a high fidelity CFD analysis ($M = 0.78$) 24
2.28 Pressure evolution inside a hydrogen fuel tank during a mission of a conventional LH_2 aircraft 26
2.29 Payload and range design space for different tank designs 27
2.30 Yaw and roll moment characteristics of a BWB aircraft, computed by a CFD solver and AVL 28

3.1 N2 chart showing Class 1 – Class 2 iteration framework 30
3.2 Trendline of OEM and MTOM of H2 BWB concepts from literature 32
3.3 Example constraint map of a 250 passenger BWB concept aircraft 35
3.4 BWB cabin layout with 3 bays 36
3.5 Diagram showing the different cabin exit design options 37
3.6 Planform parameterisation of generated BWB concepts 38
3.7 Reflexed centerbody airfoil profile 39
3.8 Supercritical outer wing airfoil profile 39

3.9 Twist distribution of the reference BWB geometry 39
3.10 Baseline twist distribution of a typical BWB concept generated by own design tool 39
3.11 Top view of side tank region 40
3.12 Rear view of side tank region 40
3.13 Top view of aft tank region 41
3.14 Side view of aft tank region 41
3.15 Example of modification of length of last aft tank to satisfy required fuel volume 41
3.16 Spanwise local wave drag coefficient distribution over a BWB aircraft 45
3.17 Shocks (indicated in gray) over a BWB aircraft surface 45
3.18 Diagram of LH_2 storage tank 46
3.19 Thermal layers used to perform thermal sizing 48
3.20 Engine TO thrust versus dry weight trendline 50
3.21 Engine TO thrust versus fan diameter trendline 50
3.22 Engine TO thrust versus length trendline 51
3.23 Front centerbody weight estimation using different methods 53
3.24 Diagram showing twist angle indices 55

4.1 Front view of side tank region for verification of the tank fitting algorithm 61
4.2 Example BWB geometry generated in ParaPy 61
4.3 Example BWB geometry generated in AVL 61
4.4 Verification of induced drag computed by AVL 62
4.5 Verification of neutral point computed by AVL 62
4.6 Class 1 – Class 2 iterations convergence from initial Class 1 sizing 63
4.7 Two sequential Class 1 – Class 2 iterations: first for another BWB variant and then for the same BWB planform as in Figure 4.6 63
4.8 L/D versus lift coefficient for the example BWB concept for verification of estimated maximum L/D 64
4.9 Validation of computed tank gravimetric efficiency for different tank radii with a constant tank volume of 100 m^3 66
4.10 BWB geometry used for validation of aerodynamic model 67
4.11 Lift and drag data for validation of aerodynamic model 68
4.12 Drag polar data for validation of aerodynamic model 68
4.13 Pitching moment data for validation of aerodynamic model 69

5.1 Planforms of the BWB concepts used for the sensitivity analysis 72
5.2 Planform sensitivity matrix for the side fuel BWB variant 73
5.3 Planform sensitivity matrix for the mixed fuel BWB variant 74
5.4 Planform sensitivity matrix for the aft fuel BWB variant 75
5.5 Sensitivity of performance metrics to engine position for different BWB variants. Differences indicate change from wing mounted to aft mounted engines 77
5.6 Cruise L/D sensitivity to airfoil twist angles for the BWB variants 78
5.7 Static margin sensitivity to airfoil twist angles for the BWB variants 79
5.8 Cruise condition sensitivity matrix for the side fuel BWB variant 80
5.9 Cruise condition sensitivity matrix for the mixed fuel BWB variant 80
5.10 Cruise condition sensitivity matrix for the aft fuel BWB variant 81
5.11 OEM, cruise L/D and fuel mass sensitivity to tank gravimetric efficiency for the side fuel BWB variant 82
5.12 Isometric view renders of the planform optimised concepts (350pax, 10 000 km) 83
5.13 Planform diagrams of the planform optimised concepts (350pax, 10 000 km) 83
5.14 Twist angle distribution of the optimal BWB concepts (350pax, 10 000 km) 85
5.15 Thickness to chord ratio distribution of the optimal BWB concepts (350pax, 10 000 km) . . 85
5.16 Isometric view renders of the planform optimised concepts (250pax, 7000 km) 86
5.17 Planform diagrams of the planform optimised concepts (250pax, 7000 km) 87

5.18 Twist angle distribution of the optimal BWB concepts (250pax, 7000 km) 89
5.19 Thickness to chord ratio distribution of the optimal BWB concepts (250pax, 7000 km) . . . 89
5.20 Isometric view renders of the cruise condition optimised concepts (350pax, 10 000 km) . . 91
5.21 Twist angle distribution of the cruise condition optimised BWB concepts (350pax, 10 000 km) 92
5.22 Thickness to chord ratio distribution of the cruise condition optimised BWB concepts (350pax, 10 000 km) 92
5.23 Planform diagrams of the cruise condition optimised concepts (350pax, 10 000 km) 92
5.24 Isometric view renders of the cruise condition optimised concepts (250pax, 7000 km) . . . 94
5.25 Twist angle distribution of the cruise condition optimised BWB concepts (250pax, 7000 km) 95
5.26 Thickness to chord ratio distribution of the cruise condition optimised BWB concepts (250pax, 7000 km) 95
5.27 Planform diagrams of the cruise condition optimised concepts (250pax, 7000 km) 95

A.1 OEM sensitivity to the tank gravimetric efficiency for the BWB variants 106
A.2 Fuel mass sensitivity to the tank gravimetric efficiency for the BWB variants 107
A.3 Cruise L/D sensitivity to the tank gravimetric efficiency for the BWB variants 107

List of Tables

2.1 Specifications of different BWB concepts . . . 7
2.2 TLRs of considered LH_2 BWB studies . . . 13
2.3 Comparison of findings of LH_2 studies . . . 20

3.1 Fuel fractions of short mission phases . . . 31
3.2 Assumed reference values for preliminary sizing . . . 34
3.3 Assumed reference values for the BWB geometry definition . . . 43
3.4 Assumed reference values for the aerodynamic analysis method . . . 46
3.5 Tank properties used for structural sizing . . . 47
3.6 Tank properties used for thermal sizing . . . 48
3.7 Engine data used for engine sizing . . . 50
3.8 Design variable bounds for the planform optimisations . . . 56
3.9 TLRs of the BWB concepts for the baseline planform optimisations . . . 57
3.10 BWB baseline cabin designs for optimisation . . . 57
3.11 TLRs of the BWB concepts for the second planform optimisations . . . 57
3.12 BWB baseline cabin designs for the optimisation with TLR changes . . . 58
3.13 Design variable bounds for the cruise conditions optimisations . . . 58

4.1 Specifications of the example BWB used for verification of the design tool . . . 60
4.2 Cabin sizing verification results . . . 64
4.3 LH_2 BWB mass breakdown as a ratio of MTOM . . . 65
4.4 Validation data of tank sizing model . . . 67
4.5 Drag breakdown validation . . . 69

5.1 Top level requirements for the BWB concepts used for the sensitivity analysis . . . 71
5.2 Baseline specifications of BWB concepts used for the sensitivity analysis . . . 72
5.3 Weight and performance specifications of the planform optimised concepts for the different exit options (350pax, 10 000 km) . . . 84
5.4 Geometrical specifications of the planform optimised concepts for the different exit options (350pax, 10 000 km) . . . 84
5.5 Weight and performance specifications of the planform optimised concepts for the different exit options (250pax, 7000 km) . . . 86
5.6 Geometrical specifications of the planform optimised concepts for the different exit options (250pax, 7000 km) . . . 88
5.7 Weight, performance and cruise condition specifications of the cruise condition optimised concepts for the different exit options (350pax, 10 000 km) . . . 90
5.8 Geometrical specifications of the cruise condition optimised concepts for the different exit options (350pax, 10 000 km) . . . 90
5.9 Weight, performance and cruise condition specifications of the cruise condition optimised concepts for the different exit options (250pax, 7000 km) . . . 93
5.10 Geometrical specifications of the cruise condition optimised concepts for the different exit options (250pax, 7000 km) . . . 93

Nomenclature

Abbreviations

Abbreviation	Definition
A/C	Aircraft
ACFA 2020	Aircraft Control for Flexible 2020 Aircraft
AEO	All Engines Operative
APU	Auxiliary Power Unit
AVL	Athena Vortex Lattice
BLI	Boundary Layer Ingestion
BWB	Blended Wing Body
CFD	Computational Fluid Dynamics
CO_2	Carbon Dioxide
DOC	Direct Operating Costs
EU	European Union
FEM	Finite Element Method
FM	Fuel Mass
LH_2	Liquid Hydrogen
LHV	Lower Heating Value
MAC	Mean Aerodynamic Chord
MTOM	Maximum Take-Off Mass
NACRE	New Aircaft Concepts Research
NASA	National Aeronautics and Space Administration
NO_x	Nitrogen Oxides
OEI	One Engine Inoperative
OEM	Operational Empty Mass
PM	Payload Mass
SEC	Specific Energy Consumption
TAW	Tube And Wing
TIT	Turbine Inlet Temperature
TLR	Top Level Requirement
TO	Take-Off
UHBPR	Ultra High Bypass Ratio
USA	United States of America
VELA	Very Efficient Large Aircraft

Symbols

Symbol	Definition	Unit
A	Aspect Ratio	-
A_{ref}	Reference Aspect Ratio	-
b	Total Wing Span	m
b_{cab}	Cabin Span	m
b_{cb}	Centerbody Span	m
b_i	Wing Element Span	m
b_{max}	Maximum Wing Span	m
b_n	Nacelle Width	m
b_{tank}	Side Tank Region Span	m
b_{tr}	Transition Region Span	m
b_{wing}	Outer Wing Span	m
C_D	Drag Coefficient	-
$C_{D_{add}}$	Additional Drag Coefficient	-
C_{D_i}	Induced Drag Coefficient	-
$C_{D_{nac}}$	Nacelle Profile Drag	-
C_{D_p}	Profile Drag Coefficient	-
$C_{D_{pr}}$	Pressure Drag Coefficient	-
C_{D_w}	Wave Drag Coefficient	-
C_{D_0}	Zero Lift Drag Coefficient	-
C_f	Flat Plate Friction Coefficient	-
$C_{f,lam}$	Laminar Flat Plate Friction Coefficient	-
$C_{f,ref}$	Reference Flat Plate Friction Coefficient	-
$C_{f,turb}$	Turbulent Flat Plate Friction Coefficient	-
C_L	Lift Coefficient	-
$C_{L_{max}}$	Maximum Lift Coefficient	-
C_{L_α}	Lift Curve Slope	rad^{-1}
$\bar{c}$	Mean Aerodynamic Chord	m
$\bar{c}_i$	Wing Element Mean Aerodynamic Chord	m
c_r	Outer Wing Root Chord	m
$c_{r,i}$	Wing Element Root Chord	m
c_t	Outer Wing Tip Chord	m
c_0	Aircraft Center Chord	m
D_{nac}	Nacelle Diameter	m
D_{tank}	Tank Diameter	m
E	Endurance Time	s
E_{loit}	Loiter Endurance Time	s
e	Span Efficiency Factor	-
e_{clean}	Clean Span Efficiency Factor	-
e_{slats}	Slats Deployed Span Efficiency Factor	-
e_w	Weld Efficiency	-
e_o	Tank Surface Emissivity	-
FF	Form Factor	-
FF_{nac}	Nacelle Form Factor	-
FF_{wing}	Wing Form Factor	-
g	Gravitational Acceleration	$\text{m}\,\text{s}^{-2}$
h_{cab}	Cabin Height	m
h_{conv}	Convection Heat Transfer Coefficient	$\text{W}\,\text{m}^{-2}\,\text{K}^{-1}$
h_{rad}	Radiation Heat Transfer Coefficient	$\text{W}\,\text{m}^{-2}\,\text{K}^{-1}$

Symbol	Definition	Unit
$h_{t,s}$	Side Tank Region Wall Height	m
k	Thermal Conductivity	$\mathrm{W\,m^{-1}\,K^{-1}}$
k_a	Thermal Conductivity of Air	$\mathrm{W\,m^{-1}\,K^{-1}}$
k_n	Nacelle Correction Factor	-
L_c	Cockpit Length	m
L_{cyl}	Tank Cylindrical Section Length	m
L_{cab}	Total Cabin Length	m
L_n	Nacelle - Mean Aerodynamic Chord Distance	m
L_{nac}	Nacelle Length	m
L_t	Tank Length	m
L_{tank}	Aft Tank Region Length	m
$L_C/2R$	Length to Diameter Ratio	-
L/D	Lift Over Drag	-
$(L/D)_{alt}$	Alternate Lift Over Drag	-
$(L/D)_{cr}$	Cruise Lift Over Drag	-
$(L/D)_{max}$	Maximum Lift Over Drag	-
$(L/D)_{ref}$	Reference Lift Over Drag	-
M	Mach Number	-
M	Mass	kg
M_{cr}	Critical Mach Number	-
M_{DD}	Drag Divergence Mach Number	-
$\dot{m}_{bo}$	Hydrogen Boil-off Rate	$\mathrm{kg\,s^{-1}}$
m_{tank}	Tank Mass	kg
N_{eng}	Number of Engines	-
N_{tank}	Number of Tanks	-
n_{bays}	Number of Cabin Bays	-
Nu	Nusselt Number	-
n_p	Number of Passengers	-
n_{ult}	Ultimate Load Factor	-
P_{amb}	Ambient Pressure	Pa
P_{max}	Maximum Tank Pressure	Pa
Pr	Prandtl Number	-
$\dot{Q}$	Heat Rate	W
Q_N	Engine Interference Coefficient	-
q	Dynamic Pressure	Pa
R	Range	m
R	Thermal Resistance	$\mathrm{K\,W^{-1}}$
Ra	Rayleigh Number	-
R_{alt}	Alternate Range	m
R_{air}	Air Thermal Resistance	$\mathrm{K\,W^{-1}}$
R_{cond}	Conduction Thermal Resistance	$\mathrm{K\,W^{-1}}$
R_{conv}	Convection Thermal Resistance	$\mathrm{K\,W^{-1}}$
R_{ins}	Insulation Layer Thermal Resistance	$\mathrm{K\,W^{-1}}$
R_{rad}	Radiation Thermal Resistance	$\mathrm{K\,W^{-1}}$
R_{struc}	Structural Shell Thermal Resistance	$\mathrm{K\,W^{-1}}$
R_1	Stress Ratio	-
R_2	Stress Ratio	-
Re	Reynolds Number	-
r_i	Tank Inner Radius	m
r_o	Layer Outer Radius	m
r_{tank}	Tank Outer Radius	m

Symbol	Definition	Unit
S	Wing Planform Area	m^2
S_{aft}	Aft Body Planform Area	m^2
S_{cab}	Cabin Floor Area	m^2
S_{ref}	Reference Wing Surface Area	m^2
S_{wet}	Wetted Surface Area	m^2
S_w	Outer Wing Reference Area	m^2
SM	Static Margin	-
s_{FL}	Landing Field Length	m
T	Thrust	N
T_{amb}	Ambient Temperature	K
T_{ins}	Insulation Temperature	K
T_{H_2}	Hydrogen Temperature	K
T_{surf}	Tank Surface Temperature	K
TOP	Take-Off Parameter	$N\,m^{-2}$
TSFC	Thrust Specific Fuel Consumption	$g\,kN^{-1}\,s^{-1}$
t	Layer Thickness	m
t_{in}	Insulation Thickness	m
t_r	Outer Wing Root Airfoil Thickness	m
t_s	Structural Shell Thickness	m
t/c	Thickness to Chord Ratio	-
$(t/c)_{wing}$	Outer Wing Thickness to Chord Ratio	-
V	Flight Velocity	$m\,s^{-1}$
V_A	Approach Velocity	$m\,s^{-1}$
V_{alt}	Alternate Velocity	$m\,s^{-1}$
V_S	Stall Velocity	$m\,s^{-1}$
V_{tank}	Tank Volume	m^3
W	Weight	N
W_{aft}	Aft Body Weight	kg
W_{cb}	Front Centerbody Weight	kg
W_w	Outer Wing Weight	N
W_{ZF}	Zero Fuel Weight	N
W/S	Wing Loading	$N\,m^{-2}$
$(W/S)_{ref}$	Reference Wing Loading	$N\,m^{-2}$
w_d	Rear Door Margin	m
x_{cg}	Center of Gravity X Coordinate	m
x_{np}	Neutral Point X Coordinate	m
$\bar{y}_i$	Wing Element MAC Y Coordinate	m
$\bar{y}_{r,i}$	Wing Element Root Chord Y Coordinate	m

Greek Symbols

Symbol	Definition	Unit
α_a	Air Diffusivity	$m^2\,s^{-1}$
β	Volumetric Thermal Expansion Coefficient	K^{-1}
ΔH_e	Hydrogen Heat of Evaporation	$J\,kg^{-1}$
ΔT	Temperature Difference	K
η_{grav}	Gravimetric Efficiency	-
θ	Twist Angle	deg
κ_A	Korn Factor	-

Symbol	Definition	Unit
Λ_{cab}	Cabin Leading Edge Sweep	deg
$\Lambda_{c/2}$	Half Chord Sweep	deg
Λ_{w}	Outer Wing Leading Edge Sweep	deg
λ_{aft}	Aft Body Taper Ratio	-
λ_{i}	Wing Element Taper Ratio	-
λ_{w}	Outer Wing Taper Ratio	-
ν_{a}	Air Kinematic Viscosity	$m^2 s^{-1}$
Π	Fuel Fraction	-
Π_{cruise}	Cruise Fuel Fraction	-
Π_{loiter}	Loiter Fuel Fraction	-
σ	Tank Design Stress	Pa
σ_{a,R_2}	Operating Design Stress	Pa
$\sigma_{a,-1}$	Reverse Loading Stress	Pa
σ_{b}	Operating Ultimate Stress	Pa
ϕ_{f}	Side Tank Fuel Volume Ratio	-

1
Introduction

1.1. Motivation

The aviation industry is an essential industry in the modern world, by providing the fastest means of transportation and connecting the world. Since the industrial revolution in the 18th century, CO_2 levels in the atmosphere have risen dramatically due to anthropogenic emissions [1]. This has resulted in an increase in global temperature [2]. Currently aviation is responsible for a significant amount of global carbon emissions with a share of 2.5 % of total global carbon emissions in 2019. Including non-CO_2 effects aviation is estimated to be responsible for 3.5 % of global radiative forcing. Of the total CO_2 emissions from the aviation industry, more than half of those emissions were caused by long range flights (> 4000 km) in 2020. This is while long range flights only accounted for roughly 6 % of the total number of flights in that year [3]. This indicates reducing emissions of long range flights is crucial. Although efficiency improvements of aircraft have resulted in a decrease in energy intensity and thus CO_2 intensity, demand increases outweigh this. The result is an overall increase in CO_2 emissions from aviation. To add to this, it is expected other industries will decarbonise faster than aviation, which will lead to the share of global emissions of the aviation industry to rise further in the future [4]. Current efficiency improvements and fleet renewal will not be sufficient to reduce carbon emissions in the industry. In a forecast for the year 2050, it is clear more radical technology improvements are necessary, as well as usage of sustainable aviation fuels and infrastructure improvements as shown in Figure 1.1 [5].

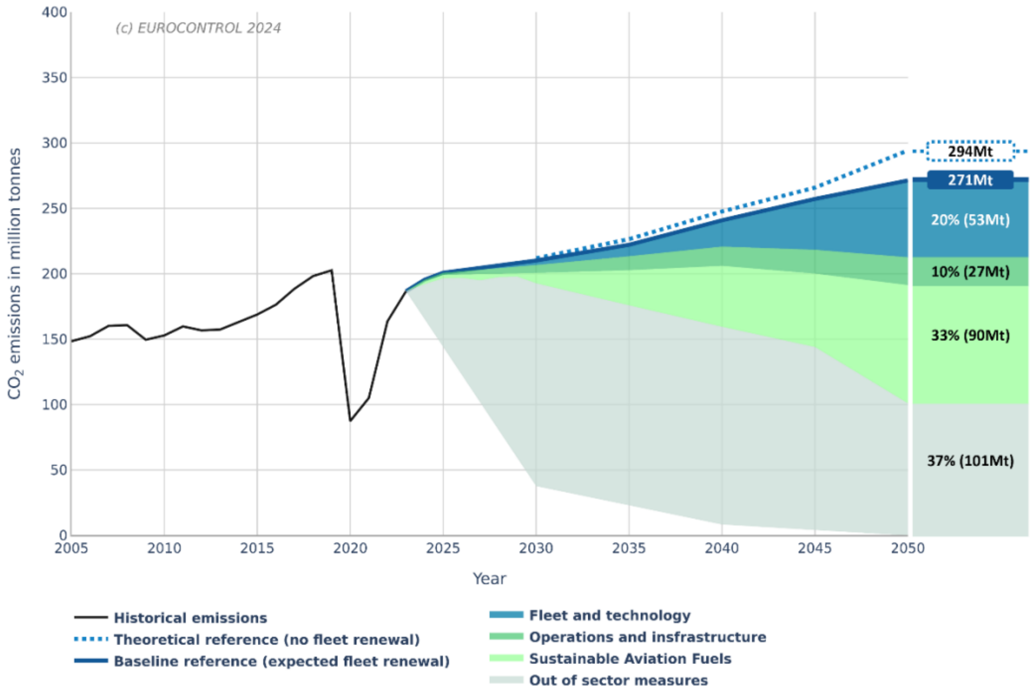

Figure 1.1: Estimated aviation CO_2 emissions between 2005 and 2050 [5]

A promising new fuel for aircraft is hydrogen, as combustion of the fuel does not result in CO_2 emissions, producing only water vapour [6]. However, the fuel comes with a number of challenges. While the specific energy of liquid hydrogen is about 3 times as high as Jet-A1 fuel, the energy density is 4 times lower [7]. This means that although 3 times less fuel mass is required, the required storage volume is 4 times as high for liquid hydrogen aircraft. Besides this challenge, other challenges are present in handling and storing the cryogenic hydrogen, producing the hydrogen fuel economically and sustainably and designing hydrogen propulsion systems. A aircraft configuration that is promising for the use of hydrogen as a fuel is the Blended Wing Body (BWB) concept. The blending region (where the thick centerbody transitions to the slender outer wing) of this configuration presents a large volume that is impractical for the storage of passengers or cargo, however it can be used for storing hydrogen fuel [8]. Inherently, the BWB concept presents a better surface area to volume relation due to its shape, providing more internal volume to store fuel in compared to tube and wing (TAW) aircraft.

Previous studies have investigated the general feasibility of the BWB concept [9–15], while more recent studies have investigated hydrogen powered BWB aircraft [16–23]. The BWB concept is expected to be a feasible configuration for the usage of liquid hydrogen fuels, presenting similar energy penalties when switching to hydrogen as TAW aircraft. This means that the efficiency improvements of kerosene BWB aircraft compared to TAW aircraft [10] are also expected for hydrogen variants [18].

The studies on hydrogen BWB aircraft that were published recently have not focused on the effects of different hydrogen tank layouts in the aircraft in detail. The resulting aircraft internal layout, gravimetric efficiency of the tanks and their effects on the total aircraft level performance have not been studied in detail.

1.2. Research Scope, Objective and Questions

This work, which is performed at the Royal Netherlands Aerospace Center (NLR), investigates the relation between the internal layout of long range, liquid hydrogen combustion powered BWB aircraft and their overall aircraft level performance by designing several aircraft variants at a conceptual level using a parametric aircraft design and analysis model. The research includes the creation of this parametric design and analysis model and the analysis of different variants to evaluate their performance, according to the following set performance metrics: maximum L/D, operational empty mass (OEM), mission fuel mass and static margin. The following main research question has been formulated:

What effect do the LH2 fuel tank shape and positioning, cabin layout and corresponding outer shape of an H2 turbofan powered BWB concept have on its aircraft level performance?

To help answer the main research question the following subquestions have been formulated:

1. What is an achievable parameterisation of the internal layout (cabin shape, fuel tank geometry and placement) of the concept to adequately assess its effect on the aircraft level performance?
2. What BWB concept variant(s) provide(s) the best performance according to set performance metrics?
3. What are the effects of top level requirement choices within the mid to long range class (payload, design range) on the feasibility and performance of the concept(s)?
4. What is the sensitivity of the aircraft level performance to the design parameters and disciplines?

First a review of relevant literature is presented in chapter 2, after which the methodology used to answer the research questions is explained in chapter 3. Verification and validation of the methods will be performed in chapter 4. The results will be presented in chapter 5 and the conclusions and recommendations of this work will be discussed in chapter 6.

2
Literature Review

In this chapter existing literature on BWBs and LH_2 propulsion will be reviewed. First, in section 2.1 the BWB concept in general will be treated, after which literature on LH_2 usage in aircraft will be reviewed in section 2.2. Next, previous work on BWBs with LH_2 combustion will be explained in section 2.3 and finally conceptual BWB modelling aspects will be reviewed in section 2.4.

2.1. BWB Concept

2.1.1. Flying Wings

Before the BWB concept was created, flying wings had already extensively been researched and even developed. The first flying wings were already being developed in the early 20th century, mainly in Europe. The most groundbreaking work was done by the Horten brothers, who developed many flying wing aircraft. One of their designs is the Horten 229, one of the first jet powered flying wing aircraft [24] (shown in Figure 2.1). The Horten 229 was never taken into service, only performing prototype test flights in 1945.

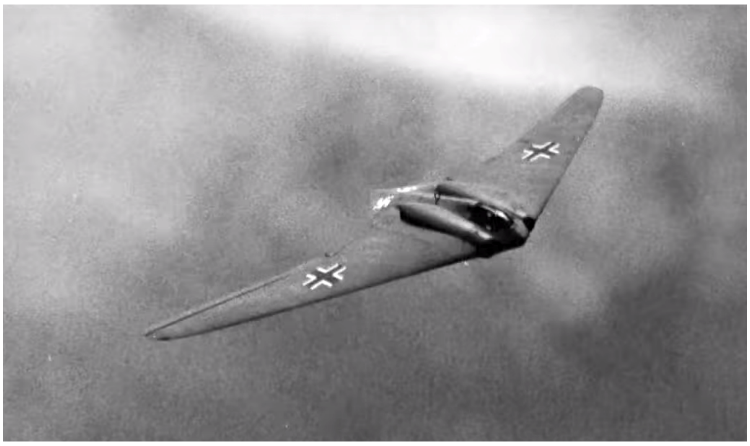

Figure 2.1: The Horten 229 in flight [25]

In the United States, the Northrop Corporation was founded in the 1920s. This corporation developed flying wing aircraft throughout the 20th century. This work resulted in the development of the XB-35, an experimental propeller driven flying wing, shown in Figure 2.2. THe prototype had its first flight in 1946 [26]. The XB-35 was modified by replacing the propeller engines with jet engines, which resulted in the YB-49, shown in Figure 2.3. The YB-49 prototype flew first in 1947 and generally showed good performance, however stability issues and crashes caused the project to be discontinued [27].

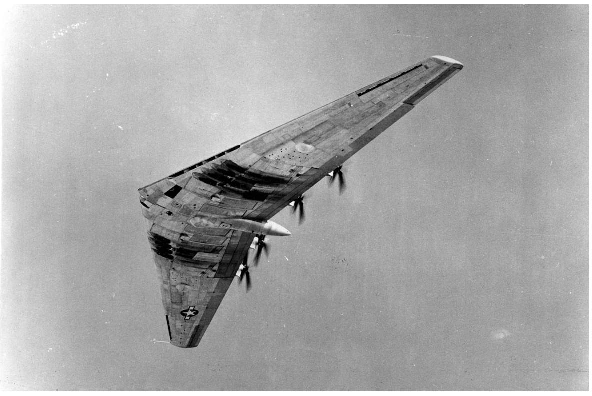

Figure 2.2: The Northrop XB-35 flying wing [26]

Figure 2.3: The Northrop jet powered YB-49 flying wing [27]

Some time later, Northrop developed the B-2 flying wing, a heavy bomber. Having its first flight in 1989, the B-2 turned out to be a success and was put into service in 1993. The B-2 Spirit is shown in Figure 2.4

Figure 2.4: The Northrop B-2 Spirit heavy bomber [28]

2.1.2. Boeing Baseline BWB-450

Following the success of the B-2 flying wing, interest in flying wing concepts was reignited. This resulted in a small study performed at McDonnell Douglas, funded by NASA. The goal was developing and comparing new subsonic transport technologies for a design mission of 800 passengers and a 13 000 km range. At first there were issues with circular fuselage pressure vessels, directing the design back to a conventional TAW configuration. Removal of the circular pressure vessel constraint and further development resulted in the first and second generation BWB transports [10]. The second generation 800 passenger concept is shown in Figure 2.5. It has a double deck passenger cabin layout to fit the large number of passengers. The feasibility and performance of this concept was evaluated using several analyses. The aerodynamical features of the concept were evaluated using a CFD analysis, after which a scaled wind tunnel test was performed to validate the accuracy of the CFD results for a BWB concept. A critical attention point was the stability and control of the concept. It was decided that stability augmentation was a requirement for this concept. A flight demonstrator with an augmentation system was tested and showed excellent handling qualities. In terms of performance the concept achieved a higher L/D than conventional aircraft at that time (23 vs 19). These improvements are the result of a decrease in wetted area to reference area ratio of the BWB aircraft of 33 % compared to a TAW aircraft [10].

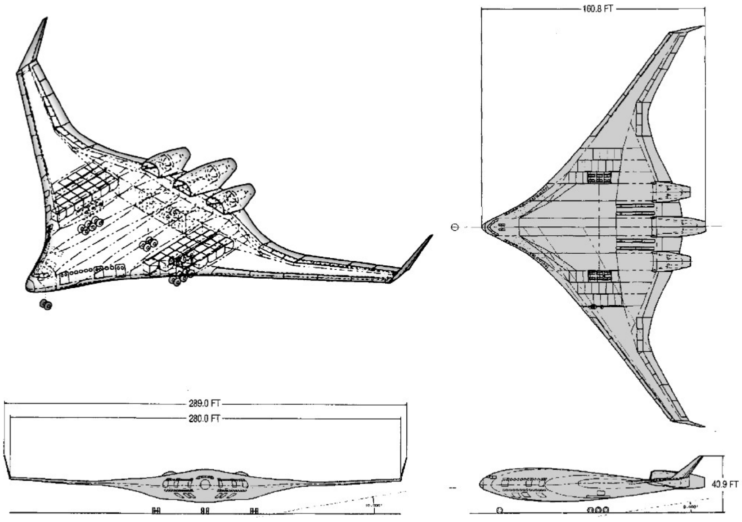

Figure 2.5: Second generation 800 passenger BWB concept [10]

After demonstrating the feasibility of the 800 passenger BWB concept, a preliminary design of a BWB transport was made at Boeing. For this study it was decided that the original top level requirement point of 800 passengers and 13 000 km is not realistic for the market at the time. Instead, a 468 passenger and 14 000 km range concept was developed, which will hereafter be referred to as the BWB-450. This concept has a single three-class passenger deck with the cargo placed under the passenger deck. In Figure 2.6 the concept is shown.

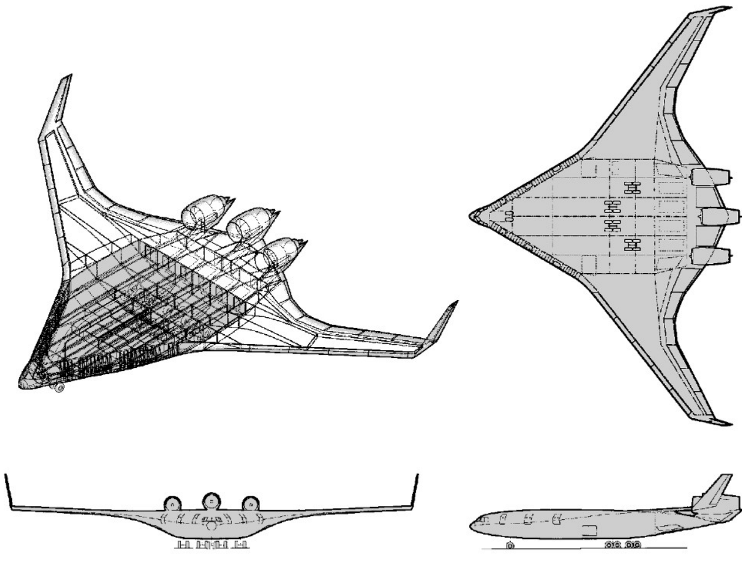

Figure 2.6: Boeing baseline BWB-450 concept [10]

Besides aiming for a more realistic payload-range combination, this concept was also designed with airport wing span requirements in mind. An optimisation procedure was performed to obtain the baseline concept. Due to the combination of the payload carrying capacity and lifting capacity in the blended region of the concept, a BWB aircraft has strong interactions of the different aircraft disciplines. The strong interactions and unconventional nature of the concept mean conventional empirical design methods are not suitable for the design of a BWB aircraft. An optimisation framework integrating all the different disciplines into one design method is therefore necessary [10, 29]. An optimisation was performed with the goal to minimise the take-off mass while satisfying all constraints. This resulted in the baseline BWB-450 concept. Instead of preserving a near-elliptic spanwise load distribution, this concept was trimmed using a different spanwise load distribution and wing washout. This resulted in a statically stable flying wing, as opposed to earlier concepts [10].

A performance comparison of the baseline BWB-450 was also made, which showed significant improvements with respect to a conventional configuration at the time. The concept was compared to the A380, expecting a reduction in fuel burn per seat of 32 % and a reduction in MTOM of 18 % compared to an A380. The improvements are due to improved aerodynamic efficiency of the concept (lower wetted area), inherently different load cases in the structure and the use of composites in the centerbody. Other interesting advantages of the concept were identified to be noise reductions due to the shielding of the engines by the centerbody and easy adaptation to more or less payload by changing the number of spanwise bays in the cabin configuration [10].

2.1.3. Other Concepts

The improved aerodynamic efficiency of the BWB-450 can be explained by both the centerbody carrying the payload and the outer wings generating lift [15]. Due to the demonstrated advantages and feasibility of the BWB-450 concept, other researches into BWB aircraft were set up. A program jointly funded by the EU and the USA was set up, including several projects on BWB concepts (Okonkwo and Smith [29] based on Kozek and Schirrer [15]). Several BWB concepts followed from this program, which are the VELA, NACRE, SAX-40 and the ACFA 2020. The VELA project resulted in a very large capacity BWB concept, designed for 750 passengers and long range. From this, the NACRE concept followed. This project focused on integration of the engines aft of the center of gravity, the laminar wing and passenger evacuation [15]. The VELA and NACRE designs both have the engines under the wing, as shown in Figure 2.7. The VELA concept was estimated to have a saving potential of about 10 % in mass and 4–8 % in aerodynamic efficiency during cruise compared to a TAW configuration [15].

Another project in this program was the Silent Aircraft Initiative, which aimed to drastically reduce aircraft noise using buried top mounted engines. The concept was designed as a long range aircraft for 215 passengers. The final configuration was obtained through an aerodynamic optimisation, which achieved an elliptical span distribution on cruise which yields a large aerodynamic efficiency improvement with respect to BWB designs at the time (2010). It achieved this while having a comfortable static margin of 5–10 % and improved stall speed [12]. The SAX-40 concept is shown in Figure 2.8. The final project in the program is the ACFA 2020 project which resulted in a long range, 450 passenger BWB design. The focus of this project was designing an ultra-efficient mid-size BWB, as well as designing a flight control system. The project resulted in a BWB design with improved aerodynamic efficiency [30]. The design is shown in Figure 2.9. Specifications of the BWB concepts discussed are given in Table 2.1, note that the discussed concepts are all powered by conventional kerosene turbofan engines.

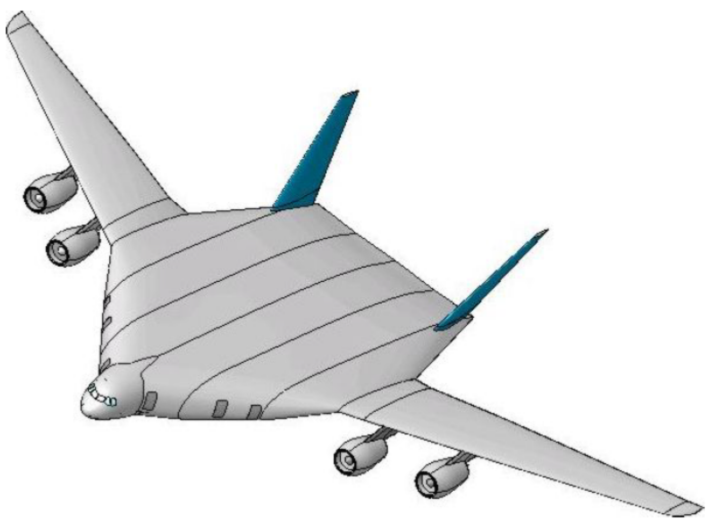

Figure 2.7: The VELA BWB design [13]

Figure 2.8: The SAX-40 BWB design [31]

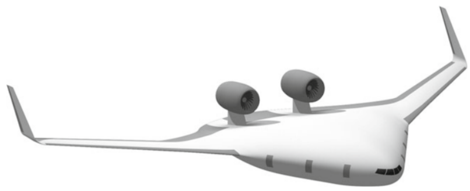

Figure 2.9: The ACFA 2020 BWB design [15]

Table 2.1: Specifications of different BWB concepts

	BWB-800 [10]	BWB-450 [9]	SAX-40 [12]	ACFA 2020 [14]
Passengers [-]	800	468	215	450
MTOM [kg]	-	373 000	151 000	402 000
OEM [kg]	-	187 000	94 000	255 000
Range [km]	13 000	14 000	9300	13 000
Cruise Mach Nr [-]	0.85	0.85	0.8	0.85
L/D [-]	23	22	25.1	24.2

A number of advantages and disadvantages of the BWB concept have been identified in studies on the concept. The advantages and disadvantages are listed below:

Advantages

- Significant improvements in aerodynamic efficiency with respect to conventional TAW aircraft. Considering the L/D values given in Table 2.1 and conventional aircraft having an L/D in the range of 15–20 (Salazar et al. [32], based on Torenbeek [33]), it is clear the BWB concept is expected to yield significant improvements.
- Decreased structural mass [10]. Although a disadvantage of the BWB concept is the non-circular cabin shape resulting in higher cabin mass, the overall aircraft mass is lower compared to conventional aircraft.
- Noise reductions [10, 12]. Liebeck [10] states that shielding of the engines due to the centerbody and avoidance of noise reflecting on the lower wing surface result in reduced noise.
- Improved boarding time, Sgueglia [34] performed boarding simulations on a BWB in the same size class as an A320. The study found improved boarding times for the BWB concept.

Disadvantages

- Non-circular cabin shape which is not optimal for pressure loads. This results in increased fuselage mass, however as explained earlier the overall aircraft mass is expected to be lower [10].
- A smaller number of windows due to the cabin shape, which affects the passenger experience [35].
- Challenges with respect to control and stability. Due to the tailless nature of BWBs, achieving a positive static margin requires careful design [10]. Ehlers et al. [36] found major deficiencies in the dynamic stability of the NACRE BWB concept, requiring the implementation of active control to achieve sufficient handling qualities.
- Emergency evacuation of passengers is a challenge for the BWB concept, especially for larger capacity designs [10]. Sgueglia [34] argues that as boarding times are sufficient evacuation times should also be sufficient. This is yet to be confirmed however.
- Cruise cabin deck angle requirements pose a challenge for designing BWB concepts, as the fuselage is also a lifting surface [10].

2.2. LH2 In Aircraft

The need for emission reductions in aviation has resulted in the search for alternative fuels. A promising fuel is hydrogen, which does not emit any CO_2 when combusted [6]. The usage of hydrogen to power aircraft is a topic that has been researched for almost a century, resulting in a large amount of literature [37]. For this study not all aspects of hydrogen aircraft will be taken into account and only relevant aspects for this research will be considered. The relevant topics that will be treated are LH_2 storage and LH_2 combustion.

2.2.1. LH2 Storage

Hydrogen has a specific energy of 2.8 times that of kerosene. On the other hand, hydrogen has an energy density that is 4 times lower than kerosene, when cryogenically stored [38]. This means the total mass of fuel required will be lower, but the storage volume is increased considerably. The large storage volume is the dominant driver for hydrogen aircraft configurations [37].

The entire fuel system will include hydrogen storage, control and distribution systems. As the control and distribution systems fall out of the scope of this research, only literature on the fuel storage will be considered. The other parts of the fuel system will be modelled as black boxes with a certain mass, based on empirical relations given in literature (like Brewer [7]). An important figure of merit for fuel storage is the gravimetric efficiency, which is defined by Equation 2.1 [8]. W_{H_2} is the weight of hydrogen in the tank, W_{tank} is the tank weight and η_{grav} is the gravimetric efficiency.

$$\eta_{grav} = \frac{W_{H_2}}{W_{H_2} + W_{tank}} \tag{2.1}$$

Adler and Martins [8] states that the tank gravimetric efficiency has a large effect on the overall design and performance of hydrogen aircraft. The energy usage relative to kerosene aircraft for different ranges and gravimetric efficiencies is given in Figure 2.10. The data is based on the Breguet range equation for constant cruise conditions and L/D [8]. It can be seen that the gravimetric efficiency has a dramatic impact on the energy usage, with the biggest effect on long range aircraft.

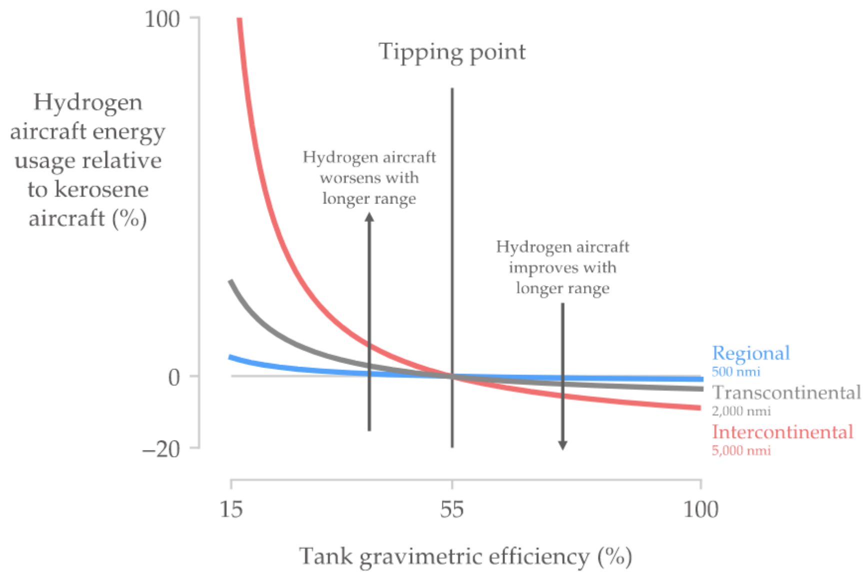

Figure 2.10: Energy usage of a conventional aircraft powered by hydrogen, relative to kerosene for different ranges and gravimetric efficiencies [8]

Besides being stored cryogenically, hydrogen can also be stored in gaseous form under high pressure. Adler and Martins [8] compiled data on several existing or designed hydrogen tanks. A plot with the collected data is given in Figure 2.11. As can be seen in the plot, liquid hydrogen tanks perform best in terms of gravimetric efficiency and volumetric energy density. The duration the hydrogen needs to stay in the tank has a large effect on gravimetric efficiency, as more insulation is required for long storage durations due to boil-off of the hydrogen. Tanks for space vehicles consume the hydrogen quickly, meaning the accepted boil-off rate is much higher than for aircraft. This allows the tanks to have little insulation, increasing the gravimetric efficiency [8]. Combining the data in Figure 2.10 and Figure 2.11 it can be seen for long range aircraft liquid hydrogen is the only viable option due to the higher attainable gravimetric efficiencies and the superior volumetric energy density. The focus will therefore be on liquid hydrogen storage options.

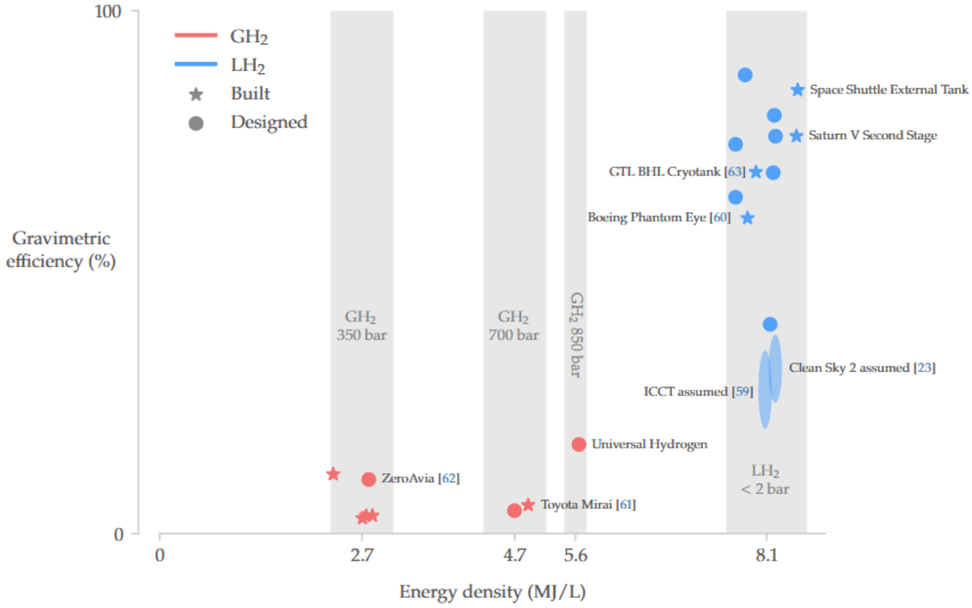

Figure 2.11: Gravimetric efficiency and energy density of various hydrogen tanks [8]

Analysing storage options in aircraft is not straightforward, as the aircraft configuration imposes physical limits on the size and shape of the tank. The fuel flow required by the engine has a large effect on the tank design as well. The size, shape and fuel extraction all have an effect on the boil-off rate of the tank and thus the required insulation. In trade-off studies it is therefore necessary to have a detailed tank model [38]. Heat flow into the tank is proportional to the surface area of the tank. To minimise boil-off, it is therefore important to minimise the surface area to volume ratio of the tank. This means a spherical tank with maximum diameter is best for low boil-off [8]. Several studies have looked at different tank shapes and architecture and their effect on gravimetric efficiency. Huete and Pilidis [39] found that the insulation technology used and maximum pressure of the tank have a considerable effect on tank gravimetric efficiency. The study also found that for large tanks the radius has the largest effect on gravimetric efficiency, while the length and volume of the tank have a smaller effect. For maximum gravimetric efficiency the radius should be as large as possible. The study also suggests the optimum tank configuration can only be determined using a system level analysis, as there is a trade-off between aerodynamic efficiency and tank gravimetric efficiency. This is reflected by gravimetric efficiencies showing smaller variations for different tank volumes (and thus lengths) while keeping the tank radius constant. Dannet [40] found that small cryogenic tanks placed in the wing are not feasible due to either very thick and heavy insulation or a large, unsafe boil-off rate. Rompokos et al. [41] states that large cylindrical tanks need to be subdivided to avoid stability issues due to the hydrogen moving in the tank. Huete and Pilidis [39] found that for vacuum insulated tanks, splitting of the tanks does not have a negative effect on gravimetric efficiency. However the study also found that generally foam insulated tanks are superior to vacuum insulated tanks. Foam insulated tanks have a mass penalty when split. This means splitting of tanks is an important consideration as well. Another advantage of split tanks is having redundancy when a tank fails, ensuring fuel flow to the engines [41].

Besides the tank properties there are other factors that influence the hydrogen storage system, such as structural loads, stratification, mixing of the hydrogen and venting. Venting is necessary when the pressure in the tank reaches the pressure limit. Hydrogen is vented overboard to avoid any further pressure buildups [41]. Stratification increases pressure buildup in the tank, however mixing results in a pressure drop [42]. Mixing of the tanks and venting of hydrogen throughout a flight has an effect on the total pressure buildup in the tank [41]. Onorato et al. [43] concluded that an efficient venting strategy has a small positive effect on the aircraft mass, however a negative effect on energy consumption. Besides accounting for pressure buildup, the tank also needs to be at a pressure higher than the ambient pressure to avoid outside air from leaking into the tank [8]. Tanks can be integral or non-integral, which has an effect on the tank properties. Integral tanks need to carry structural loads as well, however they can take up more space in the fuselage and can be closer to a spherical shape. On the other hand, non-integral tanks can be placed anywhere in the aircraft and are not bound to the outer shape of the aircraft [8].

Other challenges to consider in the design of a storage system are hydrogen permeation and embrittlement. Hydrogen is a small molecule, meaning it permeates through materials easily. Hydrogen embrittlement affects many materials, making the material more brittle when exposed to hydrogen molecules. Materials are more prone to cracking under stresses below their yield strength, which poses a safety issue. To account for these effects careful material selection is necessary [38]. The permeation of hydrogen and its wide range of flammability pose crucial safety considerations [41].

2.2.2. LH2 Combustion

Stored hydrogen obviously needs to be used to propel the aircraft. For hydrogen aircraft there are two main propulsion methods, namely hydrogen combustion in gas turbine engines and hydrogen fuel cells in combination with electric propulsors [8]. As this research will focus on hydrogen combustion in turbofan engines, only literature on this topic will be considered.

The feasibility of hydrogen combustion in turbojet engines was first demonstrated by Pratt & Whitney in 1956, when a modified jet engine was successfully run on LH_2, showing good combustion characteristics (Pratt et al. [44], based on Mulready [45]). After this an LH_2 fuel system was installed on a B-57 jet and one of its turbojet engines was powered by hydrogen. For those tests a ram air heat exchanger was used to gasify the LH_2 before combustion. Ground tests demonstrated the ratio between TSFC between the two fuels is roughly the same as the ratio in heat of combustion, which indicates there is no efficiency loss when using hydrogen (Pratt et al. [44], based on Witcofski [46]). Currently GE Aerospace, Rolls-Royce, Pratt & Whitney and Safran are all working on hydrogen turbofan engines and have plans to build and test hydrogen engines. In one of those projects CFM is working on modifying a GE Passport engine (used on Bombardier Global business jets) to run on hydrogen. This engine is planned to be tested on an A380 demonstrator, including liquid hydrogen tanks by 2025 (Adler and Martins [8], based on Airbus [47]).

The design of gas turbine engines running on hydrogen will require some changes with respect to conventional kerosene gas turbine engines. Several studies investigated the characteristics of conventional gas turbine engines being run on hydrogen. Boggia and Jackson [6] found that the fuel system and combustion chamber require redesigns. Another change should be made to the turbine and nozzle areas. This study simulated a conventional engine running on hydrogen. Other studies agree, as Corchero and Montañés [48] states that adapting a conventional engine to hydrogen does not require large-scale hardware changes, however changes to section areas have to be made to allow for effective engine matching. Here GasTurb was used to simulate a conventional baseline engine on hydrogen. Another study suggested that changes need to be made to the fuel supply system, combustion system and the addition of a hydrogen heat exchanger [49].

Several studies found the need for changes to the combustion chamber [6, 49]. When compared to kerosene hydrogen burns at higher temperatures at a certain equivalence ratio, burning about 100K hotter than kerosene. However, hydrogen is able to be combusted much leaner than kerosene [49]. This is illustrated in Figure 2.12. As can be seen in the figure, the operating range of hydrogen extends into much lower equivalence ratios than the range for kerosene. Although overall temperatures might be higher for hydrogen, the ability to operate in leaner conditions allows hydrogen to have lower flame temperatures than kerosene. In theory this reduces NO_x emissions of the combustor. There are some important considerations, however. Imperfections in mixing of fuel and air can create local high temperature flame pockets. Due to the high stoichiometric flame temperature of hydrogen it is important to avoid these local pockets, through good design of the fuel injection scheme. This should ensure good mixing [49].

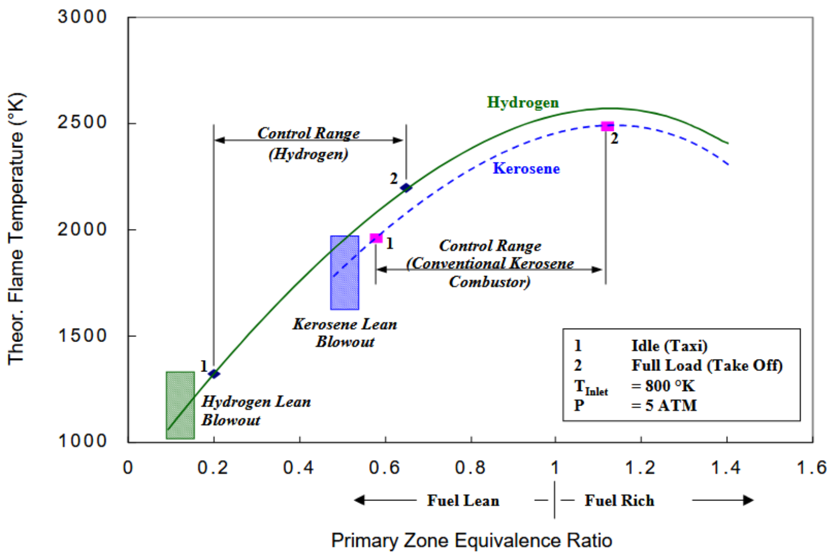

Figure 2.12: Flame temperature of kerosene and hydrogen combustion at different equivalence ratios [49]

One study researched how to run gas turbine engines on hydrogen with minimum NO_x emissions. To do this, the APU of an A320 was run on hydrogen. The APU was run with the original combustor and with an improved combustor for better mixing. The NO_x emissions were then compared to the kerosene baseline [50]. The results are shown in Figure 2.13. Note that the equivalence ratio of the hydrogen combustion is lower than kerosene, to achieve equal heat release. As can be seen in the figure, hydrogen combustion in the regular combustor leads to comparable NO_x emissions as for kerosene. The modified combustor for improved mixing leads to considerable decreases in NO_x emissions, however.

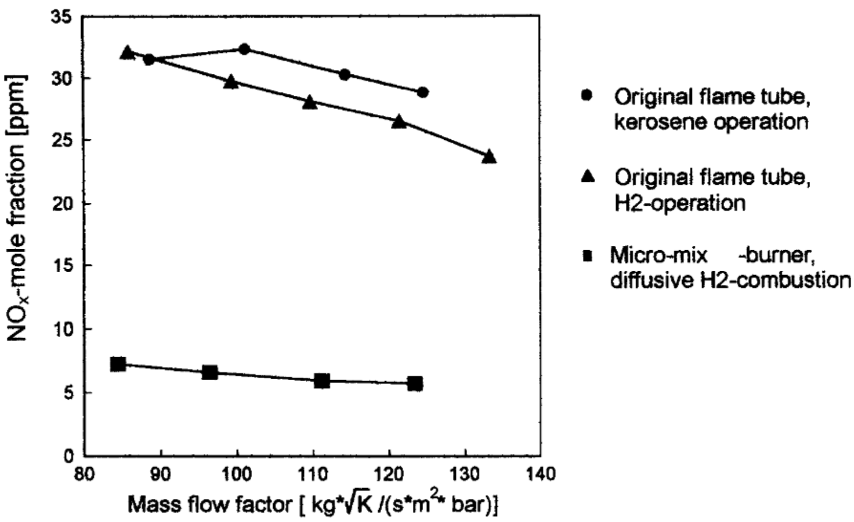

Figure 2.13: NO_x emissions for kerosene and hydrogen combustion, with and without mixing [50]

Besides evaluating NOx emissions in hydrogen gas turbine engines, several studies have researched the overall performance of hydrogen engines. As mentioned earlier, Corchero and Montañés [48] analysed the performance of a gas turbine engine running on hydrogen using the GasTurb simulation software. In this study a baseline engine was taken and its performance on hydrogen and kerosene was compared. Several modifications were then made to the engine cycle to quantify the effects on overall engine performance. When running the baseline engine at equal thrust for hydrogen and kerosene, improvements are observed in the hydrogen variant. The turbine inlet temperature (TIT) of the hydrogen engine is about 37 K lower for equal thrust, which suggests an increase in engine life can be achieved, as the turbine will experience lower temperatures. Another interesting improvement is observed in the specific energy consumption (SEC). An improvement of around 1 % can be observed, which can be explained by the change in fuel properties when burning hydrogen. Note that the hydrogen engine has an external heat exchanger to heat the hydrogen to 250K before injection into the combustion chamber. The study also evaluated the effect of fuel temperature before injection on overall performance of the engine. Figure 2.14 shows this effect for the engine with an external heat exchanger. The TSFC improves with increasing fuel temperature (1–3 %), however this also results in a slight increase in TIT (about 1–2 K) [48].

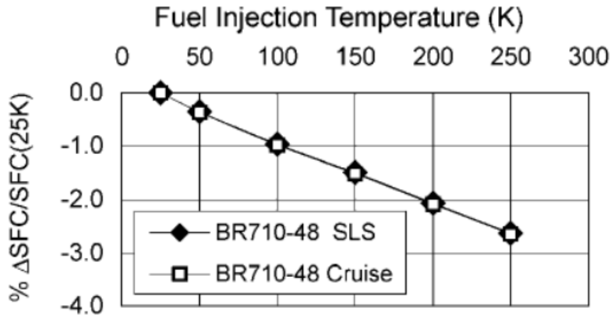

Figure 2.14: Change in TSFC of hydrogen temperature, compared to a temperature of 25K [48]

Another study performed simulations of different engine configurations running on both kerosene and hydrogen. To identify the fundamental effects of hydrogen combustion a simple turbojet engine was simulated, running on kerosene and hydrogen [6]. This study found a similar improvement in SEC for the hydrogen engine as found in Corchero and Montañés [48]. For equal TIT an improvement of about 1.5 % in SEC was observed, as well as an increase in net thrust. Corchero and Montañés [48] mentioned this improvement can be explained by different fuel properties, however Boggia and Jackson [6] dives deeper into the exact reason behind this improvement. In the simulations two changes are observed, namely the mass flow after the combustion chamber being lower for the hydrogen variant (due to the lower TSFC of hydrogen) and a different gas composition. The decreased mass flow results in larger temperature and pressure drops in the turbine, which results in decreased thrust. On the other hand, the gas composition of a hydrogen engine is different. No CO_2 is present and instead much more water is present. This causes the specific heat of the gas mixture to be higher than when burning kerosene. Overall, the increased specific heat outweighs the reduced mass flow in the turbine and exhaust, with improved performance as a result. The change in massflow is also what causes the need for different turbine/nozzle areas for engine matching [6].

Boggia and Jackson [6] next focuses on different turbofan configurations, running on hydrogen. Results are compared to a kerosene reference. For the conventional configuration, again improvements with respect to the kerosene baseline can be observed. For equal TIT, the SEC increases with 1.7 % and 2.8 % at take-off and cruise thrust, respectively. An increase in thrust was also observed, which means that for equal thrust the TIT would be lower. As mentioned earlier, this would have a positive effect on turbine life. Different configurations were also simulated. As the LH_2 is stored cryogenically, it offers a large heat sink that can be utilised. The following configurations are found to be promising: Precooling of inlet air with the LH_2 heat sink and preheated fuel using the hot exhaust air. The first configuration causes the compression work to decrease, as the compressor temperature is lower. This results in improved performance and additionally the lower temperature improves engine life. An improvement in TSFC of 5.7 % with respect to the hydrogen baseline engine was observed, however a mass increase is also expected due to the configuration change. The second configuration also results in an improvement in TSFC of 3.9 %, but no mass increase is expected. The study found both configurations to be interesting and technically feasible, without additional turbomachinery. Safety wise the engines should also be acceptable [6].

Maniaci [51] compiled the results of several full engine cycle analyses and computed the average performance changes of the hydrogen engines compared to the kerosene baseline. It found an average improvement of approximately 3 % in SEC during take-off and an average improvement of approximately 1 % during cruise.

Improvements in engine performance are clearly expected when switching to hydrogen. The LH_2 can be used as a heat sink for further improvements in performance. However, Abedi et al. [52] is less optimistic about improvements using the heat sink. As the fuel heat management system has a considerable effect on overall engine performance, this study created a detailed fuel architecture and heat management system to evaluate the effect of different architectures on engine performance. The performance is compared to a baseline LH2 engine without a dedicated fuel heat-management system. The study considered precoolers and intercoolers in the compression system, evaluating different design points of the heat exchangers. The LH_2 is heated by the air in the compressors, similarly to the precooler in Boggia and Jackson [6]. For the precooler the study found a positive, but very limited impact on engine impact. For the intercooler it found an improvement of 0.3 % in terms of TSFC. The study does however foresee more significant improvements in TSFC with an optimised engine cycle and intercooler. The engine analysed here has a conventional engine cycle.

2.3. Previous Work on LH2 BWBs

2.3.1. Top Level Requirements of Considered Studies

So far the BWB concept and general findings on LH_2 in aircraft have been discussed. BWB aircraft powered by hydrogen turbofans with LH_2 storage have been a new area of research in the recent years. There have been conceptual studies which will be discussed in this section.

As explained earlier, although LH_2 has a higher gravimetric energy density, a challenge is its much lower volumetric energy density. To account for the high required storage volume conventional aircraft might not be the best choice [8] and require significant changes to the fuselage or a reduction in passenger capacity [16]. BWB aircraft show more potential when combined with hydrogen as a fuel, due to the inherently large internal volume and high aerodynamic efficiency. Adler and Martins [8] states that the blending region between the cabin and outer wings offers a large volume that is unusable for cargo storage, however it can be used to store the hydrogen fuel with a low drag penalty. This promising combination of technologies resulted in several studies researching the potential of LH_2 BWB aircraft powered by turbofans. In Table 2.2 the top level requirements of the concepts evaluated in the considered studies are listed, as an overview. The findings of each study will be discussed after. As shown in the table most studies considered long range aircraft, while Chan et al. [19] performed a comparative study and ONERA considered a short-medium range aircraft. It is apparent the concept in Karpuk et al. [17] has a significantly lower cruise altitude than the other concepts. This is because this study assumed reduced turnaround times and based the mission conditions on reaching the same aircraft availability as existing aircraft. The reduced turnaround time therefore allowed this concept to fly lower and slower.

Table 2.2: TLRs of considered LH_2 BWB studies

BWB Concept	**Passengers [-]**	**Range** [km]	**Cruise Mach Nr [-]**	**Cruise Altitude** [ft]
Smith [16]	550	13 900	0.85	35 000
Karpuk et al. [17]	378	10 600	0.79	25 000
Adler and Martins [18]	420	10 200	0.8	35 000
Chan et al. [19]	200-800	3700–15 700	0.8	39 000
ONERA [21]	150	5100	0.78	40 000

2.3.2. Findings of LH2 BWB Studies

Smith [16] is one of the earliest publicly available studies that considered a liquid hydrogen powered BWB aircraft. The goal of this work was to design a long range LH_2 BWB in the same capacity category as the Boeing 747. A conceptual design was created using a combination of analysis methods for conventional aircraft and previously applied methods for BWBs. The study mainly focused on checking the feasibility of the design and considered many aspects of the aircraft, without diving deeper into any of the specific aircraft disciplines. The baseline BWB-450 was used as a reference for the layout of the aircraft. For the hydrogen tanks only the internal volume was checked to see if the fuel could fit. It did not give any indication on the performance (with respect to energy consumption, emissions) of the aircraft with respect to TAW aircraft or kerosene BWB baselines. It did however conclude that the aircraft meets all the performance and operational requirements that were considered. Challenges were identified with respect to the static margin, which was found to be small. The study recommended class 3 analyses to evaluate the static margin. Other issues include passenger comfort due to the absence of windows and evacuation. Recommendations were also made with respect to more detailed aerodynamic analyses to have a better understanding of the centerbody aerodynamics. A maximum L/D of around 23 is estimated. Finally, the combination of the BWB concept with LH_2 was found to mitigate each other's disadvantages, due to the low maximum lift coefficient of BWB aircraft and the large required volume for LH_2 storage.

A large limitation of this work is the lack of a more critical analysis of the fuel tank placement and mass. The study considered a large number of fuel tanks distributed over the centerbody and outer wings. The fuel tank mass was calculated using a conventional mass estimation method with a mass penalty of 50 % to account for heavier tanks [16]. Considering earlier discussed findings on LH_2 fuel tanks in aircraft the feasibility of the tank layout and accuracy of the tank mass are questionable.

A more recent study was performed by Karpuk et al. [17]. In this study a long range LH_2 BWB conceptual design is created and assessed. Several novel technologies are also implemented into the design and a comparative assessment is made between the hydrogen BWB and a kerosene one. The technologies that were implemented are load alleviation, advanced structures, boundary layer ingestion and ultra-high bypass ratio engines. The load alleviation is implemented through a maximum load factor reduction, while the advanced structures translates to a reduction in airframe mass. The BLI and UHBPR engines are implemented through TSFC improvements. The aerodynamic shape of the aircraft was optimised in the study to minimise drag, subject to internal volume constraints. Comparisons of the planforms of the kerosene BWB and hydrogen BWB are given in Figure 2.15 and Figure 2.16. The extending and narrowing of the cabin for the hydrogen BWB can clearly be observed, as well as the significant size increase of the hydrogen BWB to provide the internal volume required for the hydrogen fuel.

The study found that there is a large dependence of the planform on the size of the fuel tanks. The size of the tanks had a large effect on cabin sizing, planform dimensions and aerodynamic characteristics of the aircraft. Narrowing and extending the cabin was found to avoid range limitations of the aircraft. However, it was mentioned a longer and narrower cabin creates concerns with respect to crash safety. The performance of the aircraft was evaluated through an emission analysis, which included production emissions of the hydrogen. Flight energy consumption was estimated, as well as the effect of the novel technologies. It was found that the individual novel technologies have a significant effect on the optimised aircraft planform, with conflicting effects. Significant improvements in energy consumption are expected, as well as emission reductions. The emissions are estimated using a detailed model that takes the flight altitude into account. When blue hydrogen (produced through natural gas reforming with carbon capture) is used a CO_2 equivalent emission reduction of 18 % with respect to the kerosene BWB is estimated. A reduction of 44 % compared to a Boeing 777 was estimated, while for green hydrogen (electrolysis with renewable electricity) a reduction of 88 % was estimated. The comparison is made based on a reference mission. A significant increase in energy consumption of around 27 % is estimated compared to the kerosene BWB. This is due to the larger planform which is necessary to allow for sufficient internal volume for the hydrogen fuel, which outweighs the decreased mass due to the lower fuel mass. An energy consumption decrease of 35 % is estimated compared to the reference Boeing 777. This decrease is due to the improvements of the BWB concept itself and the use of novel technologies [17].

Karpuk et al. [17] implemented a more realistic placement of the tanks, placing cylindrical tanks in the centerbody of the aircraft. A structural analysis and thermodynamic analysis was applied for estimating the tank mass and sizing the tanks. Where possible, the analysis tools are validated and show conservative results. A more detailed discussion of the analysis tools is provided later in this chapter. The implementation of a detailed tank model gives more confidence in the results, however the study included novel technologies, which provide an optimistic estimation of the aircraft performance. The aircraft is compared to a currently flying aircraft, which does not include the novel technologies. A significant portion of the emission improvements is therefore due to those technologies. As explained earlier, for the design cruise conditions the study looked at the flight availability of the aircraft. It made an optimistic assumption by reducing the turnaround time, making flying lower and slower a viable design condition. The reference conventional aircraft does not fly at a lower altitude, which means part of the emission improvements are due to flying lower and slower.

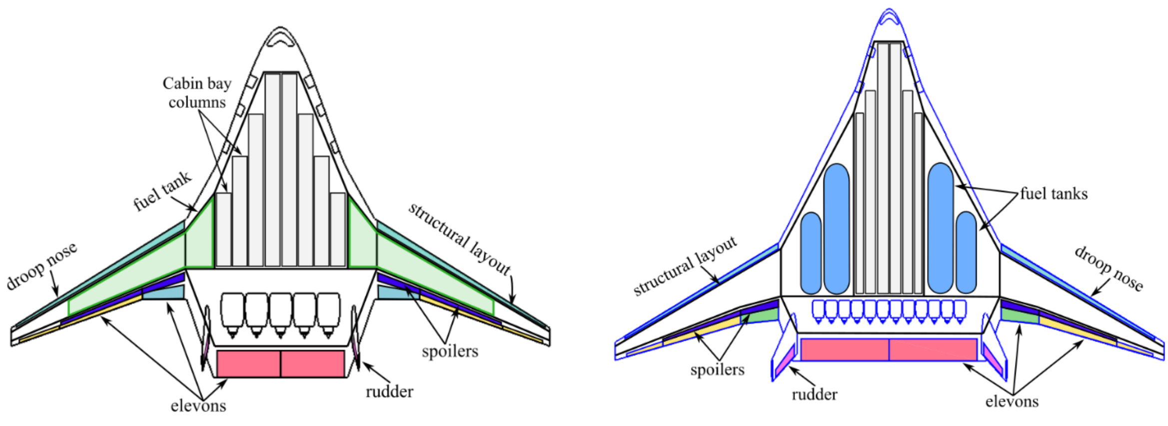

(a) Kerosene BWB (b) LH_2 BWB

Figure 2.15: Scaled planform comparison of kerosene and LH_2 BWBs Karpuk et al. [17]

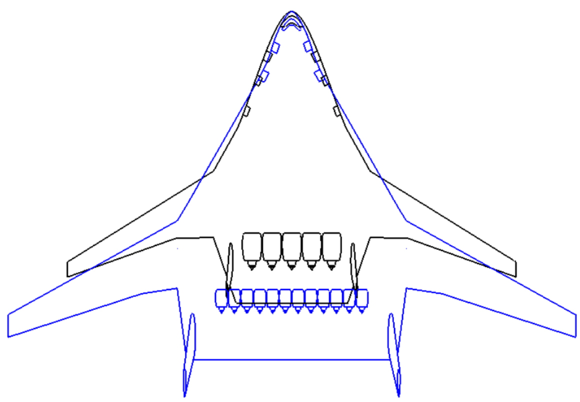

Figure 2.16: Absolute planform comparison of kerosene (black) and LH_2 (blue) BWBs [17]

Adler and Martins [18] performed a comparative study between kerosene and LH_2 aircraft. Comparisons between a kerosene and hydrogen version of both a TAW and BWB aircraft were made. Conceptual designs of each aircraft were made, after which the energy consumption of each version is estimated. The study focuses on evaluating which aircraft configuration is better suited to switching to hydrogen fuel. The BWB concept is designed to provide similar cabin area to a Boeing 787-9, while the planform is taken from reference BWBs (such as the BWB design from Liebeck [10]). No novel technologies were implemented in any of the aircraft designs. The study performed an optimisation of the aerodynamic shape with internal volume constraints. The tanks were placed in the centerbody next to the cabin and were assumed to be conformal with the aircraft shape, meaning the hydrogen fuel is assumed to take up the full volume of this aircraft region. A gravimetric efficiency was assumed for the conformal tanks. The cabin was not modified compared to the kerosene BWB. The kerosene BWB and LH_2 BWB planforms are shown in Figure 2.17. The conformal hydrogen tanks are indicated in red in the figure. The biggest difference between the planforms that can be observed is the centerbody of the BWBs. The centerbody of the hydrogen BWB is significantly widened to provide sufficient internal volume for the hydrogen fuel.

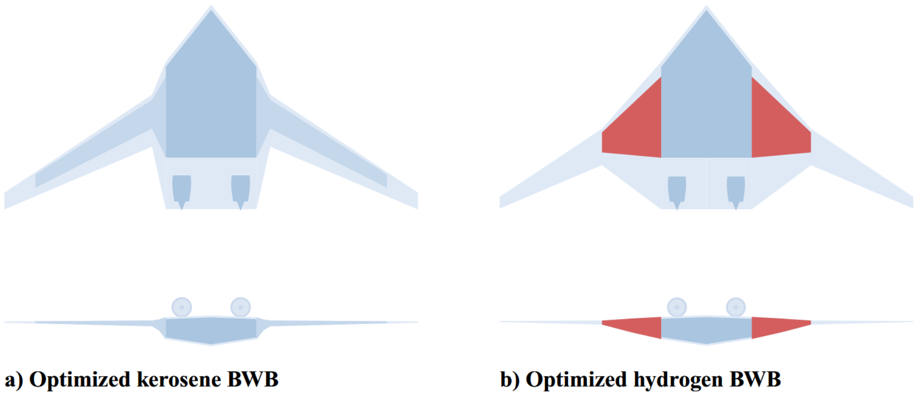

Figure 2.17: Planforms of kerosene and LH_2 BWBs [18]

The study found the hydrogen BWB to have an increase in energy consumption of 3.8 %, compared to the kerosene BWB. The hydrogen TAW aircraft was found to have an increase of 5.1 %, compared to the kerosene TAW aircraft. This indicates the BWB configuration performs slightly better when modified to be powered by hydrogen. It must be noted that the assumed gravimetric efficiency is an optimistic one, resulting in the conclusion that BWB configurations might not be the silver bullet for LH_2 storage. The energy penalties for switching to hydrogen are similar for both aircraft configurations. The study recommends more work to be done on different LH_2 packaging options in combination with an aerodynamic shape optimisation. The assumption of conformal tanks with a gravimetric efficiency is a limitation to the study, as the conclusions drawn on energy consumption depend highly on the assumed gravimetric efficiency. A plot indicating this dependency is given in Figure 2.18, showing this for both the BWB and kerosene aircraft. This results in a more interesting conclusion of this study, which is that the energy consumption of a BWB aircraft is less sensitive to the tank gravimetric efficiency than TAW aircraft [18]. Another limitation is the analysis of only one cabin layout, as modifications to the cabin shape were shown to have an effect on the aircraft performance in Karpuk et al. [17].

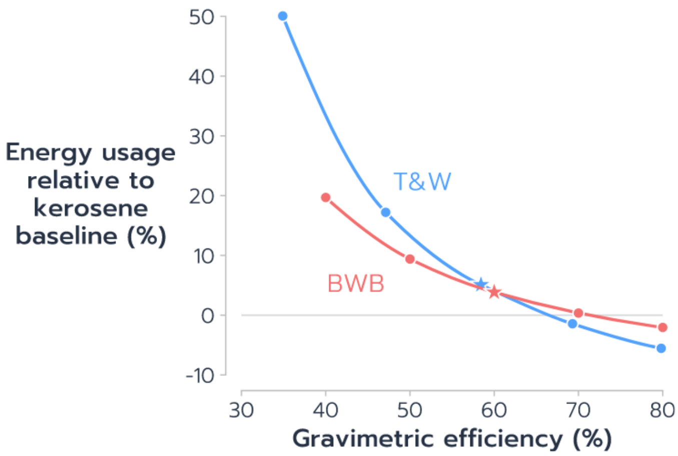

Figure 2.18: Aircraft energy consumption vs LH_2 tank gravimetric efficiency [18]

Chan et al. [19] investigated the effect of different alternative fuels on the design and performance of BWB aircraft. The study considered several capacity designs, as well as a span of mission ranges. The emissions and energy consumption of the different aircraft designs are compared to each other and to a TAW aircraft. For designs with cryogenic tanks several cylindrical tanks are placed in the centerbody next to the cabin, as well as several tanks in the area behind the cabin. The diameter of the tanks is limited by the airfoil shape. It is not clear whether a detailed tank analysis is applied to estimate the tank size and mass. A detailed mission analysis is applied to estimate the energy consumption of each design, while the emission analysis is based on emission factors, yielding CO_2 equivalent emissions. The LH_2 designs for different capacities are shown in Figure 2.19. Note that the planform does not change, however the internal layout does.

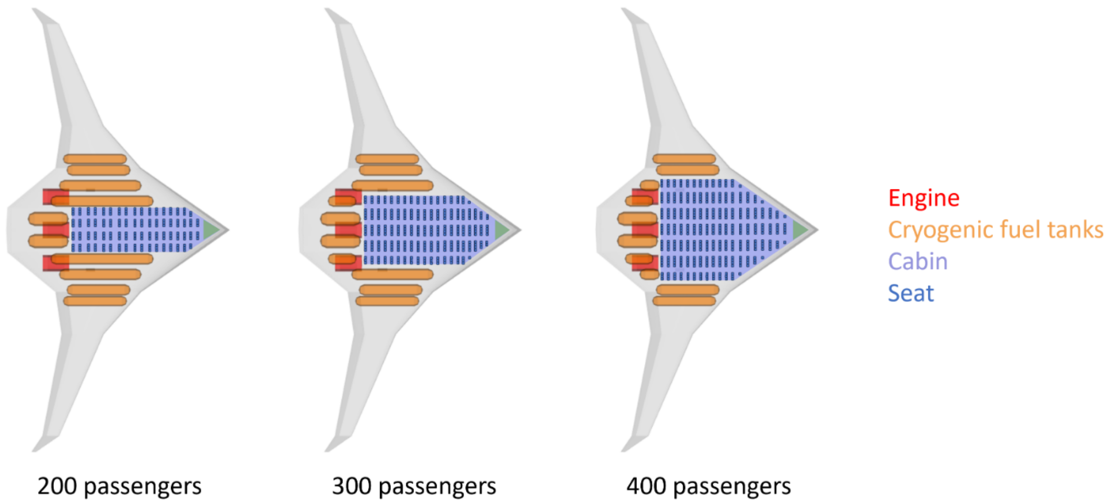

Figure 2.19: LH_2 designs for different passenger capacities [19]

An advantage of the LH_2 BWB concept was found to be the flexibility in internal layout. The cabin, fuel tank and cargo layout can be changed without any changes to the exterior of the aircraft [19]. Liebeck [10] also mentions this advantage for kerosene BWB aircraft. Chan et al. [19] did however find issues with small capacity BWB aircraft. Because the centerbody is an airfoil shape, meeting cabin height requirements is an issue. For the same reason the diameter of the cylindrical cryogenic tanks is limited, making it hard to fly long range missions with a small BWB. A proposed solution is using a larger BWB where volume normally reserved for the cabin is used for fuel storage. The study also found that the hydrogen BWB needs to operate away from the optimum L/D lift coefficient, due to the increased mass from the cryogenic tanks. Similarly to Karpuk et al. [17], it was also concluded that hydrogen BWB need to be bigger than kerosene counterparts to provide storage volume. The result is increased energy consumption compared to kerosene BWB aircraft. The energy consumption of different capacity designs powered by hydrogen and kerosene was compared as a function of mission range. In Figure 2.20 the specific energy consumptions of different aircraft designs is given.

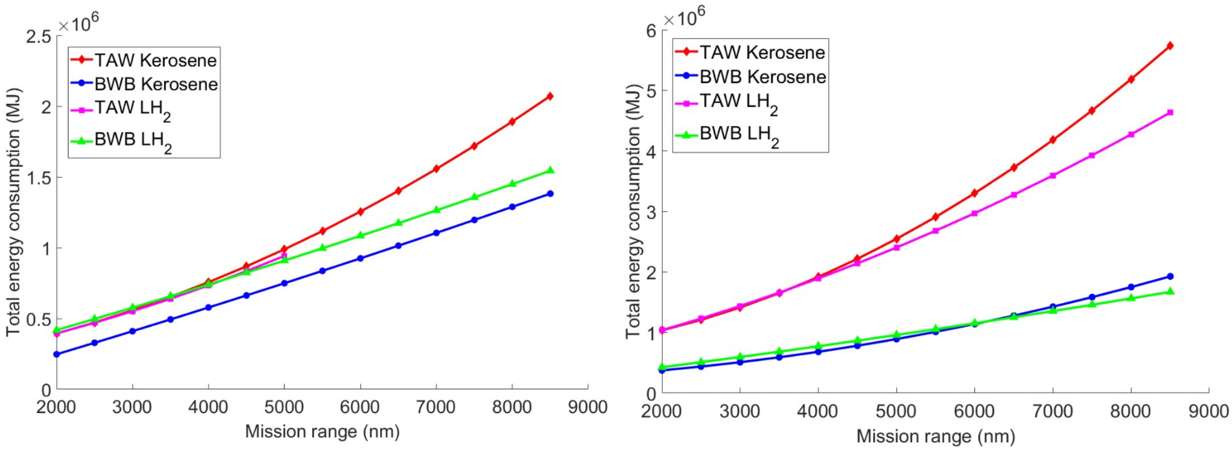

(a) 200 passengers

(b) 400 passengers

Figure 2.20: Energy consumption of different BWB aircraft designs for a span of ranges [19]

In the plots it can be observed that for 200 passengers the hydrogen BWB has a significantly higher energy consumption than the kerosene BWB for all ranges. Until a mission range of around 7000 km the energy consumption is higher than the TAW aircraft, however after this the energy consumption of the LH_2 BWB is lower. For low capacity aircraft hydrogen BWB have a higher energy consumption for every mission range. This trend changes as the capacity is increased. For the 400 passenger aircraft the energy consumption of the hydrogen BWB is higher for short to medium range missions and is roughly equal for long range missions, eventually dropping below the kerosene BWB's energy consumption for very long range missions. The tipping point is found at a mission range of roughly 11 000 km. In terms of energy consumption the BWB aircraft are superior to the TAW aircraft for every range, according to this study. The reason for the hydrogen BWB improving for longer ranges is the decreased fuel mass (and thus decreased MTOM) outweighing the increased internal volume at long ranges [19].

The fidelity of the models used in Chan et al. [19] is comparable to Karpuk et al. [17] and Adler and Martins [18]. The tank placement and volume is determined accurately, however the paper does not mention any thermodynamic or structural analyses to determined the tank mass and usable volume. Similarly for earlier discussed studies only one cabin and tank layout was considered, without any comparison between different layouts.

Nguyen Van et al. [21] (ONERA) analysed the conceptual design of a short-medium range low capacity LH_2 BWB. In earlier work the conceptual design of a kerosene BWB was created, which was used as a baseline for the hydrogen variant. Gauvrit-Ledogar et al. [53] describes this baseline BWB aircraft. A multidisciplinary design and optimisation framework was used to create the conceptual BWB, as well as an LH_2 TAW aircraft for reference. In the design, no novel technologies (such as BLI, load alleviation etc) were implemented. During the design phase the study found issues related to the balance and stability of the aicraft. The kerosene baseline has engines on top of the aft fuselage, however for the hydrogen BWB the engines were moved under the outer wing to fix the balance issues. The optimisation of the design and replacement of the engines resulted in a feasible conceptual design. The concept is shown in Figure 2.21.

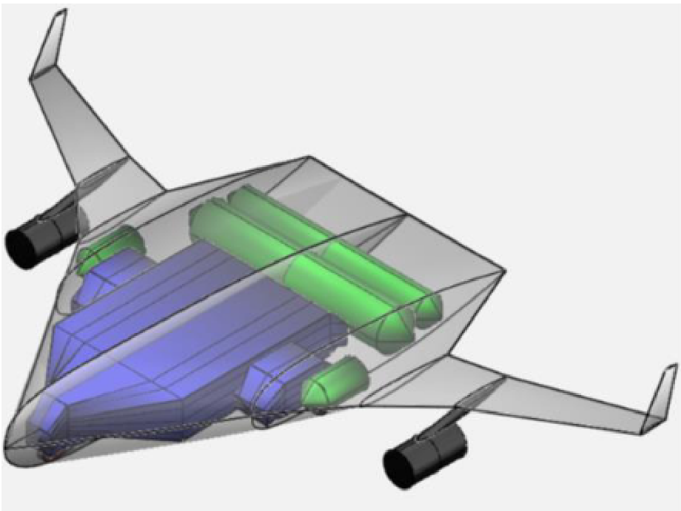

Figure 2.21: ONERA hydrogen BWB concept [21]

Compared to the kerosene BWB the hydrogen BWB did not show any improvements in terms of mass and energy consumption. The MTOM increased by about 7 %, while the energy consumption for the design mission increased by 10 %. Although the energy efficiency decreased, the hydrogen BWB is feasible without affecting mission requirements. A sensitivity study with respect to the gravimetric efficiency was performed to compare the hydrogen aircraft to each other and their kerosene reference aircraft. In Figure 2.22 the energy efficiency of the hydrogen TAW and BWB aircraft is shown for different gravimetric efficiencies. In Figure 2.23 the relative energy efficiency of the hydrogen aircraft compared to their kerosene reference aircraft is shown. From these results the study concluded that the energy consumption is highly dependent on the tank gravimetric efficiency. It also concluded that BWB aircraft are better suited for LH_2 integration, as the relative energy efficiency increased less than for the TAW aircraft. The overall energy consumption is also lower for the BWB aircraft [21]. However, even for optimistic gravimetric efficiencies the hydrogen aircraft do not show improvements in energy consumption with respect to the kerosene reference aircraft.

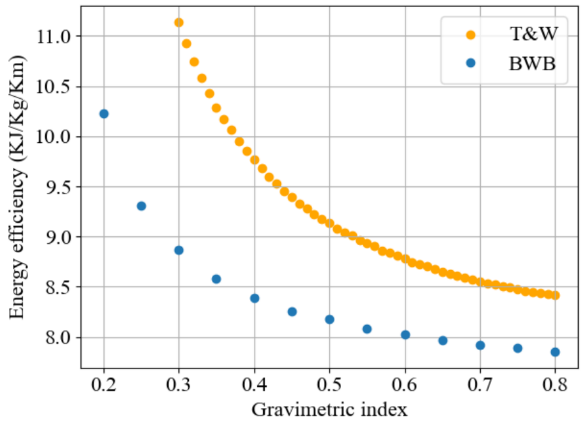

Figure 2.22: Energy efficiency vs gravimetric index for ONERA hydrogen aircraft [21]

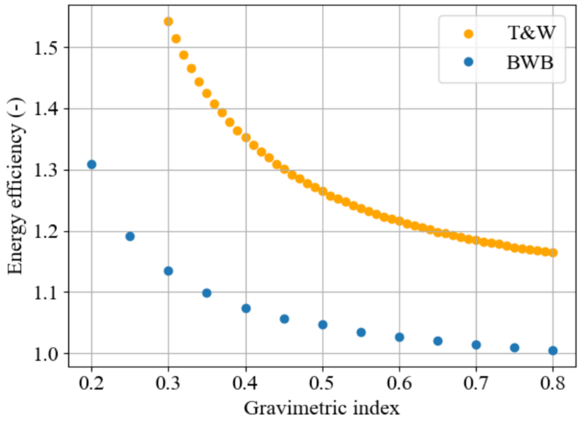

Figure 2.23: Relative energy efficiency vs gravimetric index for ONERA hydrogen aircraft, compared to kerosene reference aircraft [21]

For the internal layout the study considered a detailed model and identified several critical areas that should stay clear of fuel tanks. This resulted in most tanks being placed behind the cabin. For determination of the usable internal volume of the tanks a thermodynamic analysis was applied, however for the mass a gravimetric efficiency was assumed. As the energy consumption is highly dependent on the gravimetric efficiency and a gravimetric efficiency was assumed, it is questionable how accurate the absolute performance results of the hydrogen BWB are. The sensitivity study does provide interesting conclusions.

2.3.3. Comparison of Different Studies

The different hydrogen BWB studies can be compared to each other to give an overview of the overall findings so far. In Table 2.3 this comparison is given in a structured way.

Table 2.3: Comparison of findings of LH_2 studies

Study	Performance Metric	Reference A/C	Internal Layout and Detail of Tanks	Conclusions
Smith [16]	L/D	No reference	Baseline BWB-450 cabin with several tanks in centerbody and outer wing. Only tank volume considered.	Aircraft meets performance goals, high L/D, issues with evacuation, passenger comfort and small static margin.
Karpuk et al. [17]	Emissions, energy consumption and DOC	Kerosene BWB and Boeing 777	Extended and narrowed cabin, tanks next to cabin in centerbody. Detailed structural and thermodynamic analysis of tanks.	Emission reductions, high energy demands and large dependence of planform on tank size. Issues with evacuation, crash safety and stability
Adler and Martins [18]	Energy consumption	Kerosene variant of same configuration	Cabin based on B787-9 floor area. Conformal tanks placed in centerbody next to cabin, with assumed gravimetric efficiency.	BWB better suited to LH_2 integration than TAW. Higher energy consumption than kerosene BWB, even for optimistic gravimetric efficiency.
Chan et al. [19]	Emissions and energy consumption	A321, Boeing 777, A380 and kerosene BWB	Multiple tanks next to and behind cabin, cabin is narrowed or widened for different capacities.	For low capacity and low range BWB have increased energy consumption. Better suited for large capacity and long range missions.
ONERA [21]	Mass and energy consumption	Kerosene TAW and BWB aircraft	Same cabin as kerosene BWB, tanks placed mostly behind cabin, some tanks next to it. Thermodynamic analysis for tank volume, gravimetric efficiency for mass	All hydrogen aircraft have increased energy consumption compared to kerosene. Hydrogen BWB has higher mass than kerosene BWB. BWB is better suited to LH_2 integration than TAW.

2.4. BWB Modelling Aspects

To analyse BWB conceptual designs, analysis models are required. The different disciplines of the BWB aircraft have to be modelled with acceptable fidelity to allow for aircraft level performance analyses. The modelling approaches of several BWB studies (Both kerosene and LH_2) are discussed in this section.

2.4.1. Aerodynamic Models

For determining the aerodynamic characteristics of BWB concepts several models can be used, ranging from low to high fidelity. The main aerodynamic characteristics that were modelled by most studies were the pressure forces, drag components and the maximum lift coefficient. Some studies used high fidelity aerodynamic models that captured most of the characteristics in one analysis. Patel et al. [22] created a surrogate model using results from viscous and non-viscous CFD analyses. This surrogate model was then used in a design optimisation. Nieuwenhuizen [54] used a drag polar constructed using an aerodynamic model from earlier work [55]. Based on design changes this drag polar is modified. Faggiano [55] runs an Euler CFD analysis, after which viscous effects are computed with other methods. Versprille [56] also uses an Euler CFD method with separate methods for the viscous effects. Other studies used lower fidelity models for the inviscid aerodynamics, that required separate analyses for the different drag components.

Pressure Forces

For the studies that did not use higher fidelity methods such as CFD it was found vortex lattice methods were used. Athena Vortex Lattice (AVL) [57] is the most widely used vortex lattice method, being used by several studies [17–19, 58]. Liebeck [10] and Smith [16] also use vortex lattice methods, but not AVL. The vortex lattice method is a numerical analysis method that computes non-viscous aerodynamic forces, such as lift, induced drag and aerodynamic moments. The AVL software allows the definition and analysis of full aircraft, including nacelles and fuselages. As vortex lattice methods only compute non-viscous forces, separate methods for determining the different drag components are necessary. The drag breakdown given in Equation 2.2 is used in most studies, where C_{D_i} is the induced drag, C_{D_p} is the profile drag, C_{D_w} is the wave drag and $C_{D_{add}}$ is additional drag such as parasitic drag from probes or antennas. Note that the induced drag is taken from AVL in most studies and separate methods are used for the other drag components.

$$C_D = C_{D_i} + C_{D_p} + C_{D_w} + C_{D_{add}} \tag{2.2}$$

Additional Drag

The additional drag components were not considered by every study. In the ONERA study a constant drag coefficient was added to the total drag coefficient to account for parasitic drag [59]. Brown [58] used a method from Roskam [60] to account for additional drag.

Profile Drag

Profile drag is the combination of skin friction drag and form drag. Most studies computed the flat plate friction coefficient and applied corrections to this coefficient using form factors [17, 18, 21, 55, 56]. This is done for airfoil sections at different stations along the span, after which the individual contributions are summed. Chan et al. [19] used empirical relations from Howe and Rorie [61], which computes all drag components except lift induced drag with one empirical relation. Liebeck [10] also evaluates multiple airfoil sections at different spanwise stations and uses the airfoil section properties and vortex lattice solution to compute the profile drag. It is not specified how this is exactly computed.

Wave Drag

The computation of the wave drag is a crucial part of the aerodynamic analysis for BWB aircraft. The reasons for this will be explained later, when the validation of used aerodynamic models will be discussed. It is found that most studies use semi-empirical relations. Adler and Martins [18] uses a method described in Kays [62]. The BWB aircraft is divided into 2D airfoil sections at different spanwise stations. The drag divergence Mach number is then calculated for each section, after which a drag rise is calculated using an empirical relation. The total wave drag is then obtained by summing all the section contributions. The same method is used in the aerodynamic model from ONERA [59]. Karpuk et al. [17] uses a similar method, where first the critical Mach number for 2D sections is computed. After this the drag rise can be obtained using the ratio between the freestream Mach number and the critical Mach number and empirical data. The method is explained in detail in Shevell and Bayan [63]. Brown [58] uses a different method. Here a conventional emprical drag prediction method is used, which is explained in Feagin and Morrison [64]. This method relates the overall geometry of wings and fuselages to the wave drag. The wave drag method for wings is used for the outer wings of the BWB. A conventional fuselage method is used for the centerbody, based on the centerbody area distribution. The drag polar used in Nieuwenhuizen [54] includes wave drag, however in this work the design is changed after which corrections are applied to the drag polar. As this does not include any corrections on wave drag, the drag divergence Mach number is computed. If this is higher than the cruise Mach number the design changes are accepted, as no uncaptured drag rise is expected.

Maximum Lift Coefficient

Estimating the maximum lift coefficient of a BWB aircraft is not straightforward as using trailing edge flaps is challenging. Roman et al. [9] mentions no flaps can be used, since there is no tail to balance the aerodynamic moment created by the flaps. Hefazi et al. [65] investigated the use of a trailing edge flap system in combination with a belly flap. The study found that the take-off field length was improved, however the maximum lift coefficient decreased compared to a baseline without the high lift system. Only a few studies considered the maximum lift coefficient of the conceptual design. One of the methods used to estimate the maximum lift coefficient is the critical section method, which was used by Liebeck [10] and Adler and Martins [18]. This method considers the lift coefficient of the individual 2D airfoil sections. When the first 2D section reaches its maximum section lift coefficient the total aircraft lift coefficient at this angle of attack is taken as the maximum total lift coefficient. Karpuk et al. [17] applied leading edge slats to the outer wings to increase the critical angle of attack of those sections. The effect of slats on the sectional maximum lift coefficient was taken from Torenbeek [66]. For preliminary sizing a reference value for the maximum lift coefficient will be used, as the aircraft geometry has not been defined yet. Brown [58] and Smith [16] mention the use of reference values for preliminary sizing.

Validation of Aerodynamic Models

Determining the aerodynamic characteristics is a crucial part of the conceptual design of a BWB aircraft, due to the unconventional nature of the configuration. Special attention will therefore be given to the validation of some of the discussed aerodynamic models. Roman et al. [9] compared the results from wind tunnel tests with results from CFD. It was found that CFD can accurately predict the aerodynamic characteristics of BWB aircraft. In Figure 2.24 the drag polars of the first generation BWB presented in Liebeck [10] is given, constructed from both wind tunnel tests and CFD analyses.

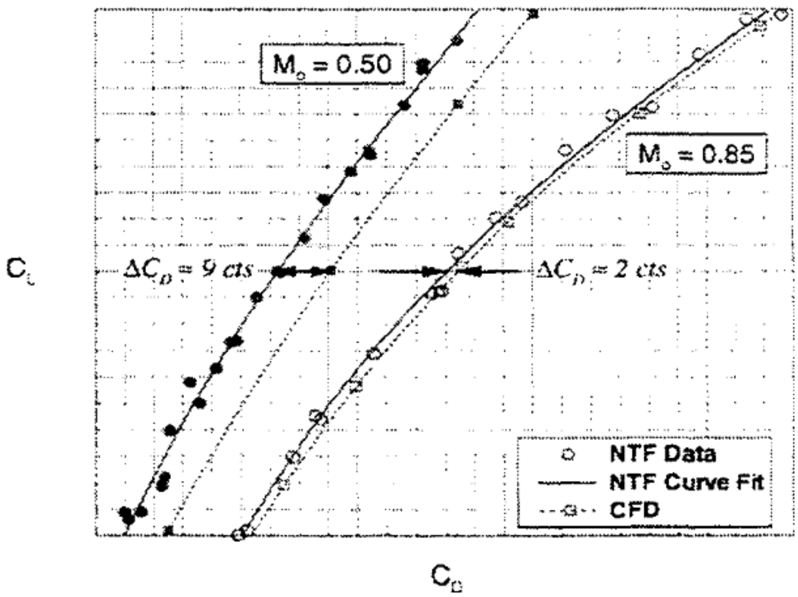

Figure 2.24: BWB concept drag polars, from wind tunnel tests and CFD [9]

Hileman et al. [12] validated the use of a vortex lattice method to compute pressure forces. The aerodynamic characteristics of the SAX-29 concept (one of the earlier concepts in the Silent Aircraft Initiative) were determined using a full viscous CFD analysis and a 2D vortex lattice method. The computed pressure distributions are given in Figure 2.25. Qualitatively the pressure distributions are similar for the CFD and vortex lattice methods. Differences in the pressure distributions are observed in the formation of shockwaves on the outer wings, as the vortex lattice method is unable to capture shockwaves and only applies a compressibility correction. The vortex lattice method does capture the centerbody and junction region between the outer wing and centerbody well, compared to the CFD results.

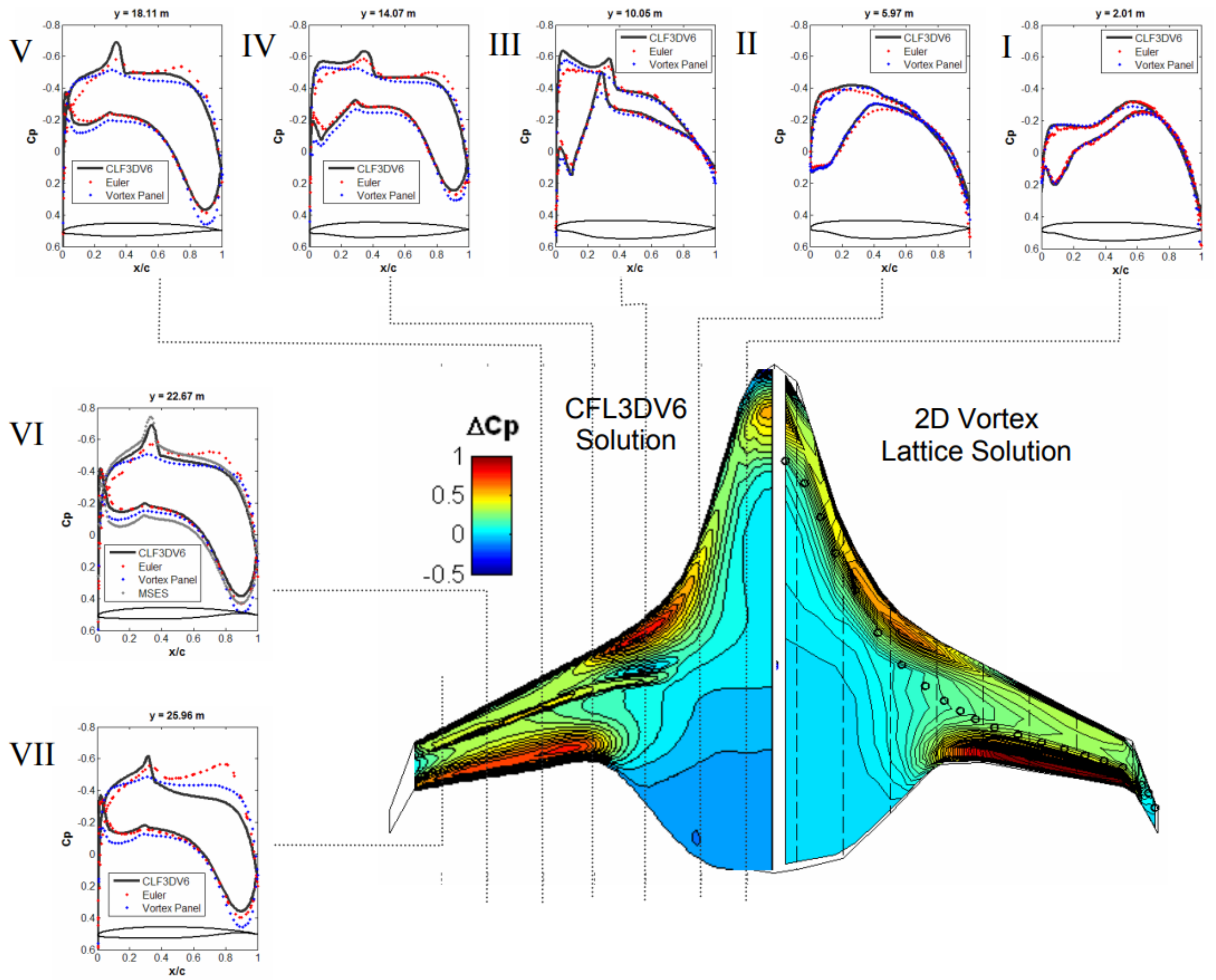

Figure 2.25: Computed pressure distributions of SAX-29 concept at a Mach number of 0.8 [12]

Karpuk et al. [17] validated its aerodynamic model by comparing it to a high fidelity CFD analysis. The computed lift curves, drag polars and moment curves are compared. The resulting curves are given in Figure 2.26. For the lift it can be seen the high fidelity analysis has a slightly higher lift slope at the cruise Mach number due to better prediction of compressibility effects. Onset of flow separation can also be seen, which is not predicted by the low fidelity analysis. For lower Mach numbers there are no significant differences between the two methods. For the drag polar large differences can be observed at the cruise Mach number. The CFD analysis predicts a significantly higher drag coefficient at high lift coefficients and seems to diverge from the low fidelity results. This is due to better capturing of shockwaves in the high fidelity analysis. Overall, at higher angles of attack and cruise Mach numbers the low fidelity method does not accurately predict the aerodynamic characteristics of the BWB concept. If high cruise lift coefficients are avoided by proper design of the BWB the low fidelity aerodynamic model is deemed accurate enough. When comparing the moment curves, it can be seen the high fidelity predicts lower moment coefficients (more negative). This results in a static margin shift. However, this shift is a conservative one, meaning the low fidelity method predicts a more conservative static margin

[17].

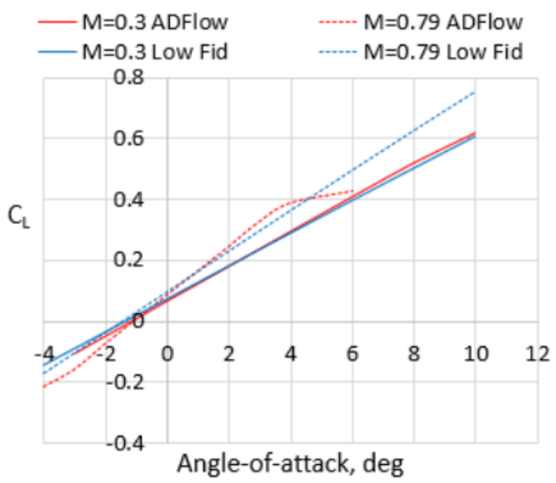

(a) Lift curve

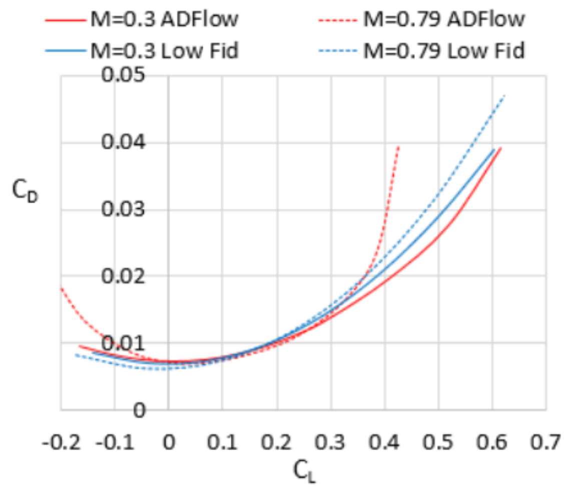

(b) Drag polar

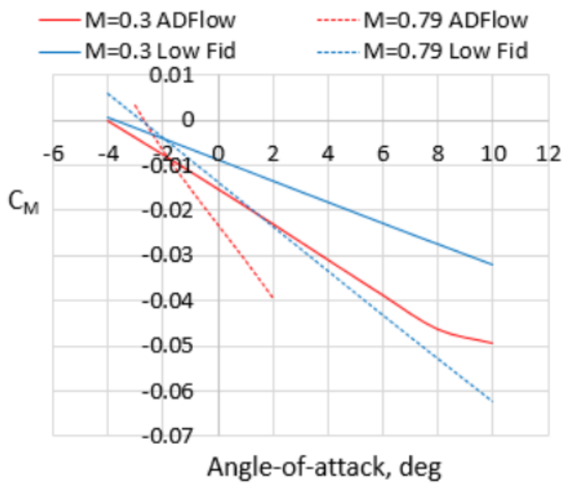

(c) Moment curve

Figure 2.26: Aerodynamic characteristics of BWB computed by a high fidelity CFD (ADFlow) analysis and low fidelity aerodynamic model [17]

Moens [59] found similar results for the drag polar, when comparing the aerodynamic model for the ONERA hydrogen BWB with results from CFD. The drag polar is given in Figure 2.27.

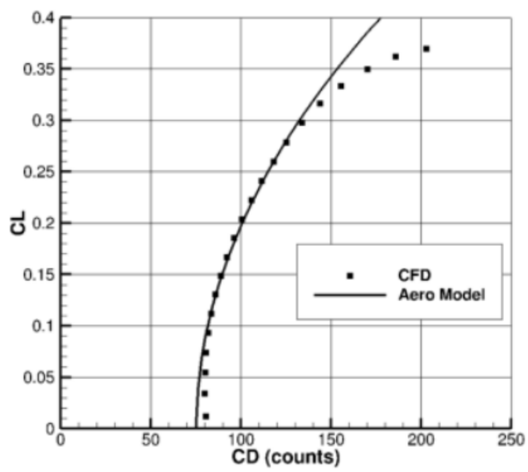

Figure 2.27: Drag polar of the SMILE BWB concept computed by a low fidelity aerodynamic model and a high fidelity CFD analysis ($M = 0.78$) [59]

Similarly to Karpuk et al. [17], the CFD analysis predicts a higher drag coefficient at higher lift coefficients than the low fidelity analysis, at cruise conditions. This is due to better capturing of wave and viscous drag [59]. The same argument can be made that the low fidelity model is accurate enough if high cruise lift coefficients are avoided.

2.4.2. Structural Mass Models

For the conceptual design of a BWB it is important to have a structural mass model that allows fast and reliable estimations of the aircraft structural mass. Since the primary structure of a BWB aircraft is different from a conventional aircraft, conventional methods such as Roskam [67] cannot be used. Bradley [68] created a semi-empirical method to rapidly estimate the structural mass of BWB concepts. The method also provides a sizing method for the passenger cabin. This method was widely used by previous studies to estimate the primary structure mass [16–18, 20, 22]. FEM analyses were performed on a BWB design, followed by a regression analysis using the FEM results. The result is regression equations to calculate the centerbody mass, as a function of the MTOM, cabin area, number of engines on the aft body and centerbody shape. The results of the regression equations were validated using predictions by Boeing, showing good agreement [68].

The other mass groups are conventional, meaning conventional methods can be used. Adler and Martins [18] computed the outer wing mass using a conventional method, however the method used for the mass of subsystems is not explained. Karpuk et al. [17] also does not mention what method is used for the mass of conventional mass groups. Smith [16] uses regression estimations from Raymer [69] and Roskam [67]. Patel et al. [22] also uses regression estimations, however from Wells et al. [70]. Chung et al. [20] uses a detailed method to calculate the mass of subsystems. Using component dimensions, material properties and structural requirements those masses are calculated.

Brown [58] uses the method from Howe [71] to calculate the primary mass of a BWB aircraft. An ideal wing mass is calculated, after which penalty factors are applied to this mass based on components placed on the wing. The method is not validated however. Brown [58] uses regression estimations for the other mass groups, using relations from Torenbeek [66].

2.4.3. Propulsion Models

For estimating the characteristics of the propulsion system different models are used. Adler and Martins [18] uses a surrogate model, based on a model of the CFM56 engine from pyCycle [72]. Improvements with respect to the TSFC of the CFM56 engine were applied, to account for improvements in more modern engines. To account for hydrogen usage the SEC was assumed to be equal to the kerosene SEC of the engine. Based on SEC improvements found in earlier discussed literature in subsection 2.2.2 this is a reasonable, conservative assumption. The fuel flow and thrust of the engine are linearly scaled, maintaining the same TSFC.

Karpuk et al. [17] uses the method described by Cantwell [73]. The method calculates the engine cycle using isentropic relations, with polytropic efficiencies to account for losses. TSFC changes based on the fuel properties are applied to the calculations to account for the use of hydrogen in the engine.

Other studies used models that are not transparent. Nguyen Van et al. [21] used an in-house code, without giving any details on the method used in this code. Chan et al. [19] integrated the NASA EngineSim software into its design tool, however the exact integration method was not explained. Documentation on the exact calculation method used by the tool was not found.

Nieuwenhuizen [54] did not apply a detailed propulsion analysis. Instead a fuel fraction method was used to estimate the fuel burn. Performance constraints were used to size the propulsion system. Brown [58] also only sized the propulsion system based on performance constraints and did not apply a detailed propulsion model.

2.4.4. Tank Sizing and Internal Layout Models

Another crucial part of modelling an LH_2 BWB concept is the internal layout and the hydrogen tank sizing. Different methods were used to model the internal layout. For sizing the passenger cabin the method explained in Bradley [68] is used by most studies [17, 19, 20]. Based on the required seating area a total bay length will be computed. The total length will then be divided over several side-by-side bays, giving a cabin shape.

Adler and Martins [18] and Nieuwenhuizen [54] sized the passenger cabin based on the total required cabin area as well, however applied their own method to define the cabin shape. Both studies based the cabin shape on earlier concepts, such as the one given in Liebeck [10]. Smith [16] copied the cabin layout of the Baseline BWB-450 and removed a bay to allow the placement of hydrogen tanks.

For sizing the tanks models with various fidelities were used. As explained earlier, Smith [16] only computed the available internal volume for the hydrogen fuel. Similarly, Adler and Martins [18] computed the available internal volume, however a tank gravimetric efficiency was assumed to calculate the tank mass. In the ONERA project a similar approach was taken, assuming a gravimetric efficiency for the tanks. However, for determining the usable volume of the tanks a thermal analysis was applied. Based on the required dormancy time, maximum allowable pressure, ambient temperature and the insulation material properties the internal and external volume of the tank was determined. Only the heat flux from convection was considered, using methods from Verstraete [38] to compute the heat flux.

For BWB aircraft only Karpuk et al. [17] applied a more detailed tank sizing method. The component mass breakdown method from Brewer [7] was used to estimate the mass of fuel system components other than the tank. The mass of the hydrogen fuel tanks was estimated using structural and thermodynamic analyses. Using limit load factors the tank is sized to withstand hoop stress. This is based on the limit load factors given by Brewer [7]. The insulation thickness and mass are calculated based on analyses given by Verstraete [38]. In this study only the heat flux through the insulation layers and the tank walls was considered. Each layer has its own resistivity, resulting in a total thermal resistance for the tank. Iterations are made until the heat flux through each of the sub-layers is equal [38]. The insulation thickness was determined using this method and a maximum allowable boil-off in the tanks. It is not clear how exactly the boil-off was modelled and what the allowances were.

Studies on conventional aircraft configurations have also implemented tank sizing models that are usable for an LH_2 BWB. Rompokos et al. [41] applied a detailed thermodynamic model to evaluate the pressure evolution inside the tank during a mission. This model considered thermal conduction, convection and radiation. The thermal resistance of the aluminium wall was neglected since it is magnitudes lower than that of the insulation. The tank is also structurally sized, according to the ASME code. The tank is structurally sized for pressure differences only. To account for stratification a pressure rise factor is applied to the theoretical value obtained by assuming a homogeneous tank. During several flight phases (taxi, take-off, climb, descent and landing) mixing is assumed. During those phases the pressure is modelled to drop back to the theoretical value. In Figure 2.28 the pressure evolution during a mission is shown.

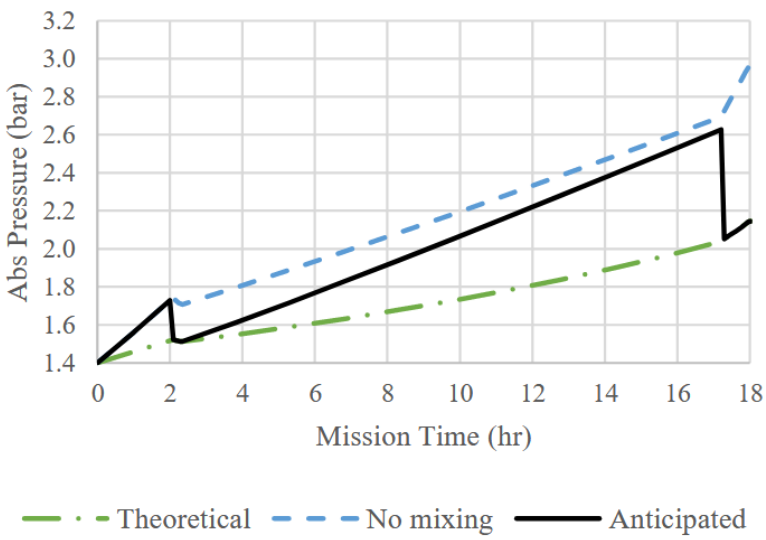

Figure 2.28: Pressure evolution inside a hydrogen fuel tank during a mission of a conventional LH_2 aircraft [41]

Tarbah [74] applied a similar method. The tank is sized for structural loads using the pressure difference and the ASME Code. The thermodynamic analysis also takes conduction, convection and radiation into account. Here only three conduction layers are modelled, which are the inner and outer wall and the insulation layer. The insulation layer thickness is computed based on the maximum allowable pressure and the boil-off rate. Stratification was ignored in this tank model.

Palaia et al. [75] uses a similar method as the earlier discussed studies for the thermodynamic and structural analysis, however starts from a certain hydrogen mass in the tanks. In this study a conventional and box wing aircraft with LH_2 tanks are analysed. The tank is optimised based on achieving maximum range. The fuel consumption and vented fuel due to boil-off is simulated throughout the entire mission duration. Once there is just enough fuel left in the tank for the descent and landing phases of the mission the simulation stops and an achieved range is computed. The insulation material, thickness and tank geometry are all variables that can be changed. In Figure 2.29 the design space for a conventional aircraft and a box wing aircraft with different tank designs is given, where $L_C/2R$ is the length to diameter ratio of the tank, t_{in} is the insulation thickness and n_p is the number of passengers. The contour lines are range values.

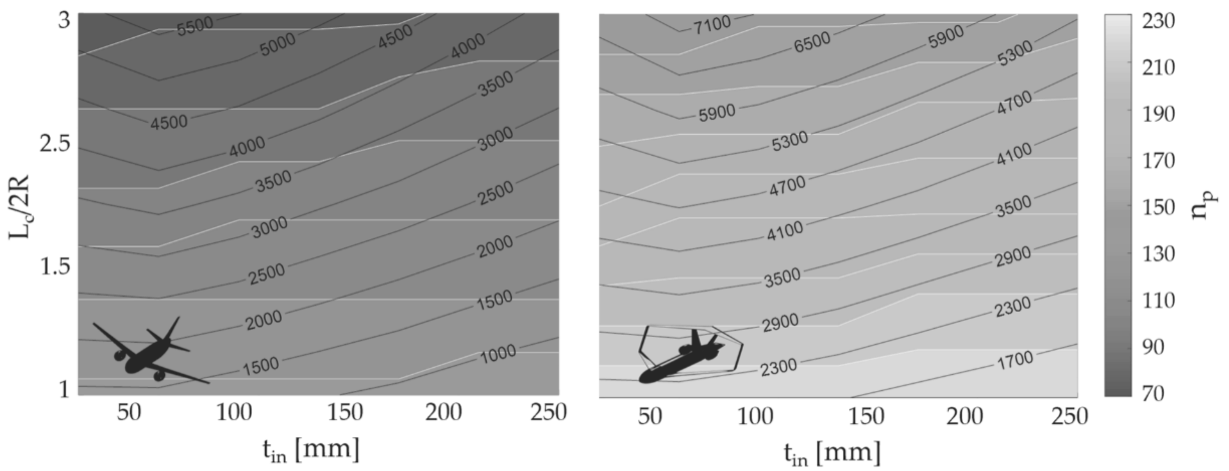

Figure 2.29: Payload and range design space for different tank designs [75]

Onorato et al. [43] included a slightly simplified tank model for a conventional aircraft configuration. The structural sizing was also done based on the pressure loads, however for the heat flux into the tank only conduction with a single insulation layer was considered. The tank is assumed to be homogeneous through mixing, while the outside tank wall temperature is assumed to be equal to the air temperature. The inner tank wall temperature is assumed to be equal to the fuel temperature. For the insulation layer properties the average temperature between the inner and outer tank walls is taken. This study did however take heat leakage through the support structure and piping into account, as well as hydrostatic pressure increase due to accelerations. For the masses of other hydrogen fuel system components an adapted Class 2 estimation equation from Torenbeek [66] was used. The pressure evolution inside the tank throughout the mission is simulated in this study, which is used in combination with an iteration loop to determine the required insulation thickness to avoid exceeding the maximum allowable pressure inside the tank. This iteration loop is included in a full conceptual design model.

2.4.5. Mission Analysis Models

For analysing a mission several methods can be used, ranging from simple to very detailed. The simplest method used is a fuel fraction method, based on typical fuel fractions for short mission phases and a cruise fuel fraction. The cruise fuel fraction can be computed using the Breguet range equation (Equation 2.3), where R is the cruise range, V is the flight velocity, g is the gravitational acceleration and Π_{cruise} is the cruise fuel fraction. The fuel fractions of other mission phases are taken from typical values found in literature, such as Roskam [76]. This method is used by several BWB studies [16, 20, 54].

$$R = \frac{V}{g \cdot \text{TSFC}} \frac{L}{D} \ln\left(\frac{1}{\Pi_{\text{cruise}}}\right) \tag{2.3}$$

More detailed models for the mission analysis are also used. Adler and Martins [18] performed a mission analysis with a time integration. At each timestep in the mission the correct lift coefficient and throttle setting is set to balance the mass and drag of the aircraft at that time. An in-house design tool is used, in which this mission analysis model is incorporated. The model is efficiently solved using a monolithic solution and analytical derivatives. Karpuk et al. [17] also performs a detailed mission analysis. This is done using the SUAVE software, which enables the analysis of the aircraft state at every timestep in a mission and computes the fuel burn for a certain mission based on this [77]. Chan et al. [19] and ONERA (Gauvrit-Ledogar et al. [53]) use a similar time integration method to determine the mission performance.

2.4.6. Weight and Balance

The balance and stability is a crucial part of designing a BWB aircraft, due to the lack of a conventional tail to balance the aircraft. In the conceptual design of a BWB it is therefore important to adequately predict the stability of the aircraft. Most of the considered studies evaluated the center of gravity and neutral point location to determine the static margin [10, 16, 17, 19, 20, 53, 58]. Gauvrit-Ledogar et al. [53] also considered dynamic longitudinal stability. It considered the trim glide, which is the ability of the aircraft to be balanced with sufficient actuator margin during approach. It also considered trim turn, which is the same condition with a steady turn rate. Another consideration was the trim take-off, which is the take-off rotation authority. The maneuver point was also determined, which is an extension of the neutral point that takes dynamic effects into account. Brown [58] considered longitudinal controllability, by sizing elevators at the aft of the centerbody. The elevator is modelled in AVL to analyse its effectiveness.

Dynamic stability was not considered much. Karpuk et al. [17] computed stability derivatives using AVL, however from validation with CFD it was found that the AVL results for dynamic stability are optimistic. Chan et al. [19] also determined stability derivatives, however it is not mentioned with what method exactly. Considerable differences in yaw and roll moment were observed between the CFD and AVL analyses. This is shown in Figure 2.30. Differences in pitching moment are also observed, which have already been explained in subsection 2.4.1.

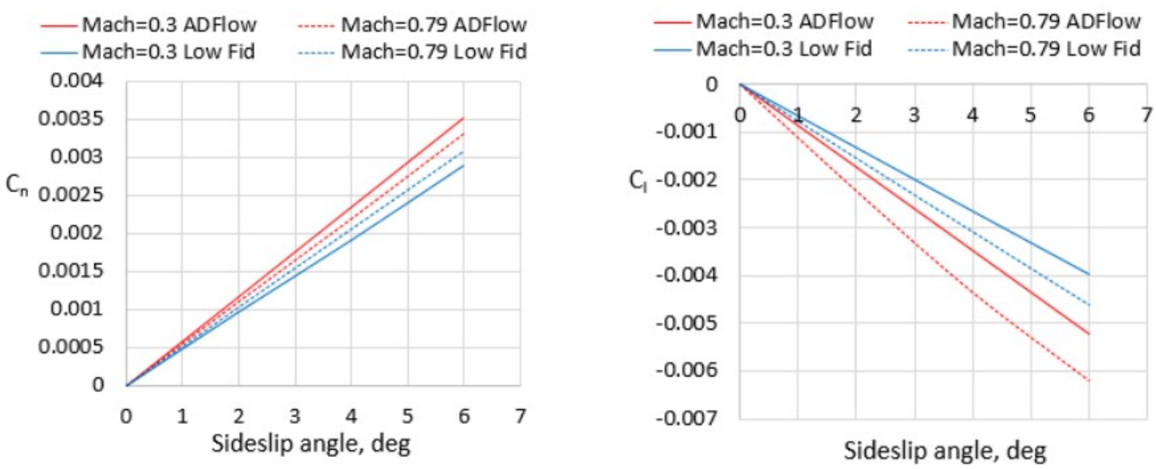

(a) Yaw moment vs sideslip angle

(b) Roll moment vs sideslip angle

Figure 2.30: Yaw and roll moment characteristics of a BWB aircraft, computed by a CFD solver and AVL [17]

3 Methodology

In this chapter the methodology used to output results and answer the main research question is described. In section 3.1 the structure of the design model is explained, in section 3.2 the preliminary sizing of BWB concepts is explained and in section 3.3 the geometry definition of BWB concepts is described. After this, the method used for the aerodynamic analysis is discussed in section 3.4, the tank sizing method is detailed in section 3.5 and the engine sizing method is explained in section 3.6. In section 3.7 the Class 2 weight estimation methods are explained and the stability analysis of the BWB concepts is described in section 3.8. Finally, in section 3.9 the concept optimisation procedure is detailed and in section 3.10 a summary of important assumptions is given.

3.1. Parametric Model Framework

To achieve the research objective of this work it is necessary to create a BWB conceptual design tool. To evaluate various different BWB variants easily, a parametric model is required that allows automatic, easy and extensive modification of TLRs and aircraft parameters. For this purpose the model is created on the ParaPy[1] platform, which is a Python library that provides multiple useful features. Among other features, the platform provides dependency tracking between variables, a geometry library and a user interface that allows easy visualisation of the created geometry and manipulation of model inputs. The library also provides built-in links between ParaPy models and analysis software, such as AVL.

The model framework that is used is similar to typical ones for conventional aircraft. First preliminary sizing (or Class 1 sizing) and a constraint analysis is performed, after wich the aircraft geometry is created and analysed. From this a component weight estimation (or Class 2 weight estimation) can be performed and iterations between Class 1 and 2 weight estimations are performed to converge the aircraft concept to a reliable weight estimate. Following this, optimisation algorithms are applied to optimise the aircraft planform for range and longitudinal static stability. This is explained in depth in section 3.9 An N2 chart of the Class 1 – Class 2 iteration framework is given in Figure 3.1.

[1] `https://parapy.nl/`

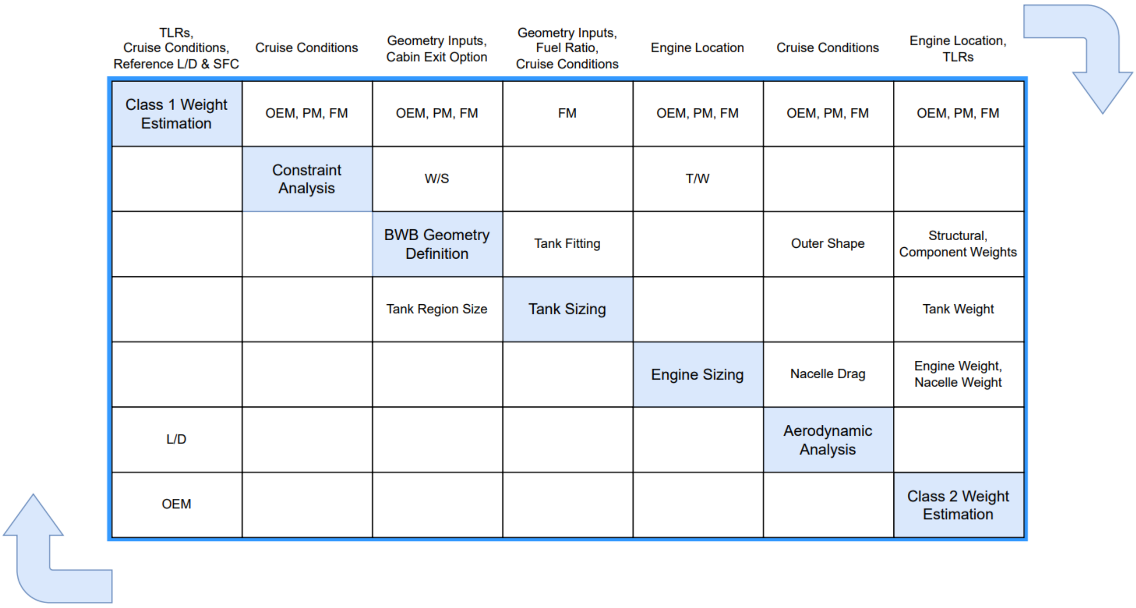

Figure 3.1: N2 chart showing Class 1 – Class 2 iteration framework

In this design loop the Class 2 OEM and L/D are fed back into the preliminary sizing module. The iterations run until the difference between the Class 1 and Class 2 OEMs is less than 0.05 %.

3.2. Preliminary Sizing

The first step in the design process of a BWB concept is the preliminary sizing of the aircraft. First Class 1 weight estimations of the concept will be performed, after which a constraint analysis is done to determine the wing and thrust loading of the aircraft.

3.2.1. Class 1 Weight Estimation

The Class 1 weight estimation method provides a first estimate of the weight of the top level weight groups of the concept. This includes the payload mass (PM), fuel mass (FM), operational empty mass (OEM) and the maximum take-off mass (MTOM), which are related according to Equation 3.1 The method used to perform the estimations is based on the method for conventional aircraft explained in Roskam [76]. First the payload mass is estimated, based on the number of passengers and required number of crew members. This means the mass of the crew members is budgeted in the payload mass, while it could also be included in the OEM. This will not affect the resulting required fuel mass and MTOM. After this the design mission fuel fraction is computed (end of mission weight to MTOM fraction). The fuel fraction definition is given in Equation 3.2, where M_1 is the total mass of the aircraft at the start of a mission phase and M_2 the total mass at the end of the phase.

$$\mathrm{MTOM} = \mathrm{OEM} + \mathrm{PM} + \mathrm{FM} \tag{3.1}$$

$$\Pi = \frac{M_2}{M_1} \tag{3.2}$$

For the short flight phases reference fuel fractions from Roskam [76] are taken, however these are for kerosene aircraft. To account for the usage of hydrogen the fuel fractions are corrected based on the lower heating values (LHV) of the fuels. This results in the following fuel fractions for the short mission phases given in Table 3.1. Note that the fuel fraction corrections do not include any aerodynamic changes of the BWB concept compared to TAW aircraft. The required hydrogen fuel mass is therefore a conservative estimate.

Table 3.1: Fuel fractions of short mission phases

Mission Phase	Fuel Fraction
Engine start, warm-up	0.9964
Taxi	0.9964
Take-off	0.9982
Climb	0.9929
Descent	0.9964
Landing, taxi, shutdown	0.9971

The fuel fractions for the longer mission phases are estimated using methods described in Roskam [76]. For the cruise mission phase the Breguet range equation is used, which is given in Equation 3.3.

$$\Pi_{\text{cruise}} = \frac{1}{e^{\frac{R \cdot g \cdot \text{TSFC}}{V \cdot (L/D)}}} \tag{3.3}$$

To determine the fuel fraction, the design mission range (R), gravitational acceleration (g), TSFC, cruise velocity (V) and L/D are required. The cruise velocity depends on the cruise altitude and Mach number entered by the user. The user also determines the design mission range, which is actually the design cruise range, as the climb and descent phases of the mission are not taken into account in the design range. The first time the Class 1 weight estimation is performed a reference value is taken for the L/D. After this the L/D is updated based on the results of the aerodynamic analysis model, which will be explained later in this thesis. The reference value is an average value obtained from several hydrogen BWB studies [17–20, 22]. For the TSFC of the concept a reference value is taken from literature representing the current state of the art high bypass ratio turbofan engines. The TSFC values of several reference engines are taken from the Janes database[2] and datasheets given in Jenkinson et al. [78]. An average value is obtained, which is corrected for the use of hydrogen. As explained earlier in subsection 2.2.2, the SEC of hydrogen engines shows small improvements compared to that of kerosene engines. To stay conservative the SEC of turbofan engines on both fuels are assumed to be equal. This means the obtained average TSFC is corrected using the LHVs of the two fuels. In section 3.6 the used reference TSFC as well as the method used to obtain it is explained.

For the alternate flight phase the Breguet range equation is also used. Corrections are applied to the inputs, as the optimal cruise altitude cannot be reached in the alternate phase. The L/D value is assumed to be 75 % of the reference cruise L/D. The TSFC is increased with 50 %, while the alternate cruise velocity is assumed to be 250 kts. An alternate range of 200 km is used. All those values are taken from Roskam [76].

For the loiter flight phase cruise conditions are assumed. A loiter period of one hour is assumed, based on the loiter time assumed in Roskam [76]. The fuel fraction for this phase is computed using the Breguet endurance equation given in Equation 3.4, where E is the endurance time.

$$\Pi_{\text{loiter}} = \frac{1}{e^{\frac{E \cdot g \cdot \text{TSFC}}{(L/D)}}} \tag{3.4}$$

The total design mission fuel fraction (Π_{total}) is then obtained by taking the product of all the individual fuel fractions. The next step is constructing a trendline between the OEM and MTOM of other H2 BWB concepts from literature. This trendline can be used in combination with the total mission fuel fraction and known payload mass to obtain the OEM, MTOM and FM. The different mass groups and fuel fraction are related to each other with Equation 3.5 and the OEM-MTOM trendline, which allows the determination of each mass group. The trendline is given in Figure 3.2. The datapoints are several H2 BWB concepts taken from literature, which are discussed in more detail in section 2.3 [16–18, 20–23].

$$\text{MTOM} = \frac{\text{OEM} + \text{PM}}{\Pi_{total}} \tag{3.5}$$

[2] https://customer.janes.com/

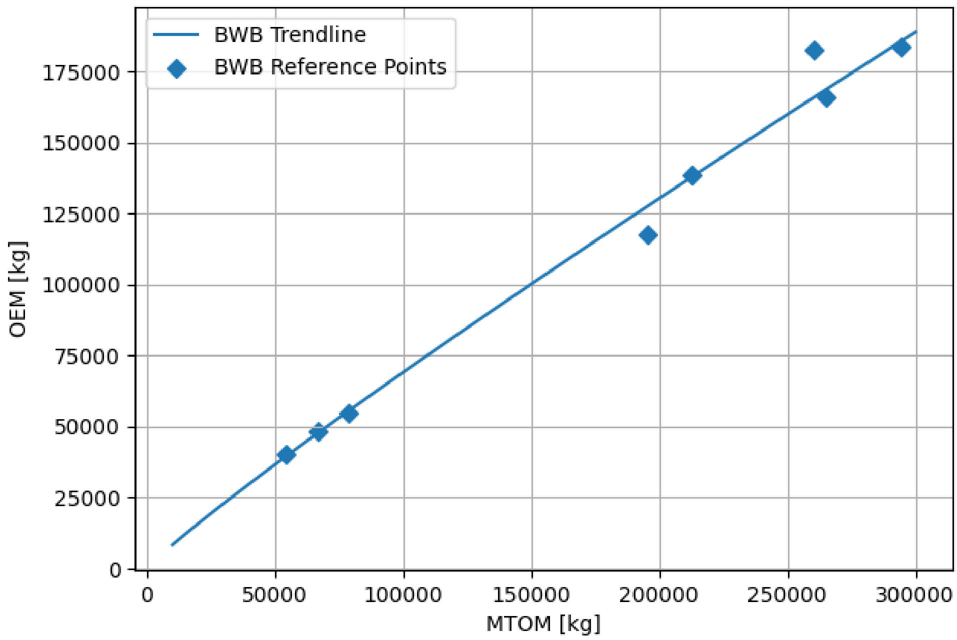

Figure 3.2: Trendline of OEM and MTOM of H2 BWB concepts from literature

3.2.2. Constraint Analysis

After computing the Class 1 weight estimations the wing and thrust loading of the aircraft needs to be determined. This is done based on a number of critical flight cases from CS25 certification specifications [79]. These flight cases impose constraints on the wing and thrust loading of the BWB concept aircraft. The sizing method for each constraint is based on the methods explained in Roskam [76]. The following flight cases/constraints are taken into account in the constraint analysis:

- Landing field length.
- Take-off field length.
- Climb gradients: one engine inoperative (OEI) take-off climb gradients (CS25.111, CS25.121a-c), all engines operative (AEO) balked landing (CS25.119) and OEI balked landing (CS25.121d).
- Cruise speed requirements.
- Maximum wing span.

Landing Field Length

The landing field length imposes a constraint on the wing loading based on the approach speed. The aircraft should have a margin to the stall speed during landing. The approach speed is related to the landing field length by Equation 3.6 [76], where s_{FL} is the landing field length in ft and V_A is the approach speed in kts. The approach speed is assumed to be 23 % higher than the stall speed (CS25.125). After determining the stall speed using the landing field length, based on the maximum lift coefficient in landing configuration the wing loading constraint from the landing field length can be computed (maximum wing loading to meet stall speed).

$$s_{FL} = 0.3V_A^2 \tag{3.6}$$

The landing field length is assumed to be equal to the landing field length of the A350-900 at sea level conditions [80], which is a length of 2000 m. The maximum lift coefficient for the BWB concept is an estimated value based on several literature sources. Like in Brown [58] the maximum lift coefficient in clean configuration is 1.1, while in take-off and landing configuration it is 1.3. This is based on Kawai [81] and van Dommelen and Vos [82]. As mentioned in subsection 2.4.1 high lift device design for a BWB aircraft is not straightforward, while several sources highlight challenges with using flaps. Therefore for the conceptual design of a BWB aircraft reference lift coefficient values are assumed, along with only the use of leading edge slats (which represents the 0.2 increase in lift coefficient from the clean configuration).

Take-Off Field Length

For the take-off field length the take-off parameter (TOP) method described in Roskam [76] is used. Some modifications are made based on Nieuwenhuizen [54] however. Rather than using a certain field length as an input, Equation 3.7 is used to compute the required take-off parameter for the BWB concept aircraft, where W/S is the wing loading, T/W is the thrust loading and $C_{L_{TO}}$ is the take-off lift coefficient. Reference data for existing aircraft is taken from Jenkinson et al. [78] to compute the TOP for those aircraft (B777-200, A330-200, B767-200, B767-300). An average TOP is then computed which is used for the BWB concept constraint analysis. The average reference TOP used for the BWB concept is 7500 N m^{-2}. Note that the TOP sizing is performed for sea level conditions. This average TOP is equivalent to a TOFL of roughly 1790 m, based on the relation given in Roskam [76].

$$\text{TOP} = \frac{W}{S}\frac{W}{T}\frac{1}{C_{L_{TO}}} \tag{3.7}$$

Climb Gradients

Sizing the thrust loading to climb gradient requirements is done for several conditions, as mentioned earlier. The following conditions are taken into account:

- CS25.111: minimum climb gradient of 1.2 % at take-off with OEI, slats extended, gear up, $V = 1.2V_S$ and take-off thrust.
- CS25.121a: minimum climb gradient of 0 % (lift-off) at take-off with OEI, slats extended, gear down, $V = 1.1V_S$, $V = 1.2V_S$ and take-off thrust.
- CS25.121b: minimum climb gradient of 2.4 % at take-off with OEI, slats extended, gear up, $V = 1.2V_S$ and take-off thrust.
- CS25.121c: minimum climb gradient of 1.2 % at take-off with OEI, slats retracted, gear up, $V = 1.25V_S$ and at maximum continuous thrust.
- CS25.121d: Minimum climb gradient of 2.1 % at aborted landing with OEI, slats extended, gear down, $V = 1.4V_S$ and take-off thrust.
- CS25.119: Minimum climb gradient of 3.2 % at aborted landing with AEO, slats extended, gear down, $V = 1.23V_S$ and take-off thrust.

In order to compute the required thrust loading for each flight condition Equation 3.8 is used [76], where CGR is the climb gradient percentage divided by 100. In order to apply this equation an estimate of the lift to drag ratio needs to be made. This is done using Equation 3.9 and the estimation method described in Roskam [76] for C_{D_0}. As all the flight velocities for the climb gradient requirements are multiples of the stall velocity, the required lift coefficients can be determined using the maximum lift coefficient and stall velocity multiple. Using the known lift coefficient and Equation 3.9, C_L/C_D can be determined, which is the same as the L/D.

To compute the zero lift drag coefficient, estimates of the reference wing area, wetted surface area and parasite area are required. The estimated wing area is computed using an average from reference wing loadings for BWB aircraft from literature [12, 15, 23, 53, 58], which is 2500 N m^{-2}. The wetted surface area is then calculated using an estimation method from Roskam [76] which is based on regression relations and requires the MTOM of the aircraft. The wetted area is reduced by 33 % to account for lower wetted surface areas of BWB aircraft [10, 19]. The parasite area is also computed using regression relations from Roskam [76], assuming a flat plate friction coefficient of 0.003. The clean C_{D_0} can then be computed, using Equation 3.10 and the estimated wetted surface area (f) and reference planform area (S). Based on the aircraft configuration (slats, landing gear) corrections are applied to the zero lift drag coefficient and the Oswald efficiency factor. With the required lift coefficient known, the total drag coefficient can be determined.

$$\frac{T}{W} = \frac{1}{L/D} + \text{CGR} \qquad (3.8) \qquad C_D = C_{D_0} + \frac{C_L^2}{\pi A e} \qquad (3.9) \qquad C_{D_0} = \frac{f}{S} \qquad (3.10)$$

Cruise Speed and Maximum Wing Span

The required thrust and wing loading for cruise conditions are also estimated using the method from Roskam [76]. The thrust and wing loading are related to each other by Equation 3.11. The clean zero lift drag coefficient found for the climb gradient is used again, however 15 drag counts are added to account for the wave drag in cruise conditions, based on Moens [59] and Brown [58]. Note that the thrust and wing loadings are to be corrected for the aircraft weight at start of cruise (known from the fuel fractions earlier described), while the thrust loading is to be corrected for the available thrust at cruise altitude (23 % of the take-off thrust is available at cruise altitude [76]).

$$\frac{T}{W} = C_{D_0} q \frac{S}{W} + \frac{W}{S} \frac{1}{\pi q A e} \qquad (3.11)$$

The maximum wing span constraint is based on a reference aspect ratio, maximum wing span and corresponding maximum wing area. The reference aspect ratio is 4.8 and is taken from BWB concepts from literature [15, 58]. The maximum wing area is then calculated using Equation 3.12.

$$S = \frac{b^2}{A} \qquad (3.12)$$

All the constraints are combined to find the maximum possible wing loading and minimum required thrust loading. In Table 3.2 the assumed reference values for the initial sizing and constraint analysis are compiled. An example constraint map for a BWB concept is given in Figure 3.3.

Table 3.2: Assumed reference values for preliminary sizing

Parameter	Value	Unit
$(L/D)_{ref}$	20	-
$(L/D)_{alt}$	15	-
V_{alt}	250	kts
R_{alt}	200	km
E_{loit}	60	min
Landing Field Length	2000	m
Take-Off Parameter	7500	N/m^2
Clean $C_{L_{max}}$	1.1	-
Take-Off/Landing $C_{L_{max}}$	1.3	-
$(W/S)_{ref}$	2500	N/m^2
$C_{f,ref}$	0.003	-
e_{clean}	0.8	-
e_{slats}	0.75	-
Cruise Thrust Ratio	0.23	-
A_{ref}	4.8	-

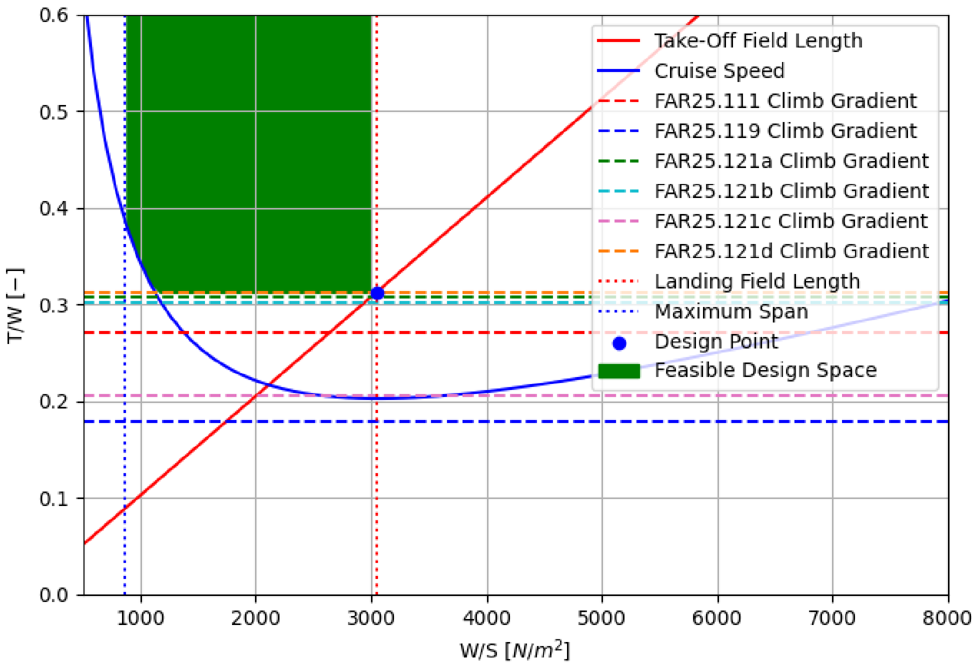

Figure 3.3: Example constraint map of a 250 passenger BWB concept aircraft

3.3. BWB Geometry Definition

After performing a first estimate of the aircraft weight breakdown, thrust requirements and size of the aircraft, the geometry is generated. This includes the internal geometry such as the cabin and tanks, after which the external geometry is constructed using airfoil sections along the span of the aircraft. Placement and fitting of these airfoil sections will be explained later in this section.

3.3.1. Cabin Sizing and Exit Design

The first step in the generation of the aircraft geometry is the sizing of the cabin, as all other components will be placed around the cabin which will result in the full internal geometry of the aircraft. The cabin is sized to fit the number of passengers, as well as required cargo volume. The method of Bradley [68] is used to define the cabin shape. In this method a regular cabin is divided in multiple bays, which are placed side by side to create a homeplate shape. A typical cabin layout with 3 bays is shown in Figure 3.4. The cabin sizing also includes the design of the exits, which will be explained in more detail later.

Cabin Sizing

First the total cabin length to fit the passengers, lavatories and galleys needs to be computed. For the cabin length the method from Roskam [83] is used. This method estimates the cabin length based on the number of passengers in each seating class and the seat pitch. For this work a 2 class configuration is assumed (business and economy). Seat pitches are taken from typical numbers for current long haul carriers. Approximately 90 % of the total capacity is economy class (the exact ratio changes as rows are completely filled). For economy class a 3-3 abreast configuration per bay is used, while for business a 2-2 abreast configuration per bay is used. The 3-3 abreast economy configuration follows from the maximum number of 3 seats abreast for one aisle (and thus one bay). The height and width of a bay are estimated using Roskam [83], at 2.13 m and 3.48 m, respectively. Extra length is added for lavatories and galleys, based on the number of passengers. Using data from Roskam [83] an average galley/lavatory area per passenger is computed, which is used to compute the additional length for the cabin sizing. After determining the total cabin length, the method of Bradley [68] is used to determine the total cabin planform shape, based on the number of spanwise bays.

For the cargo volume it is assumed most of the area under the passenger cabin can be used for cargo. Part of this area is reserved for the landing gear and other components, 20 % of the cabin length (and corresponding area) is reserved at both the front and rear of the cabin for those components. The remaining cabin area can be used to place cargo under. According to Roskam [83] the cargo hold height needs to be a minimum of 0.95 m to allow cargo personnel to work in the hold. From the estimated required cargo volume from Roskam [83] it is found that this minimum height results in more than sufficient available cargo volume under the cabin. The total height of the cabin (passenger + cargo hold) is therefore found to be 3.2 m, by adding the passenger bay height, floor thickness (22 cm) and cargo hold height.

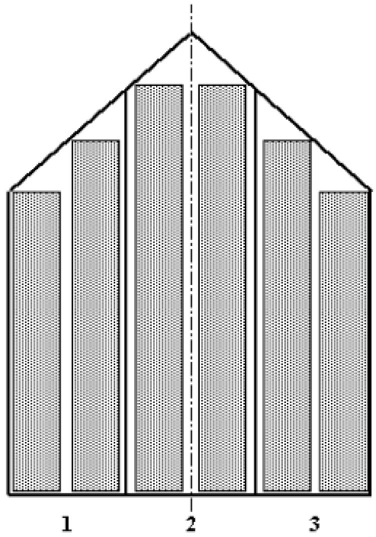

Figure 3.4: BWB cabin layout with 3 bays [68]

Exit Design

Besides sizing the cabin for fitting passengers and cargo, attention needs to be given to the design of exit doors. When considering cabin designs from literature the most commonly used layout is having the main boarding doors at the leading edge of the cabin, with additional exits at the rear portion of the side wall and rear cabin wall [10, 13, 21, 34, 53, 58]. The leading edge doors lead directly out of the aircraft structure, while for the rear doors it is unclear where the doors lead to.

As earlier discussed in chapter 2, emergency evacuation is a challenge for BWB aircraft. Since emergency evacuation times are directly linked to the cabin and exit design, extra attention needs to be given to the exit design. This is further reinforced by a number of requirements from CS25. For the intended aircraft size, requirement CS25.807 states that at least one floor level emergency exit is required at the rear of the cabin, while the longitudinal distance between two exits may not be more than 18.3 m. The location of the cabin within a BWB aircraft poses another point of uncertainty. Rear exits would be situated far inside the centerbody, which means a floor level exit corridor would lead all the way through the centerbody and transition region onto the outer wing. It is not clear what effects this would have on the centerbody structure and if this type of exit would be feasible at all. A solution could be the usage of ventral exits at the rear of the aircraft, leading down through the floor (similar to the Boeing 727 ventral exit [84]). This would however violate the floor level exit requirement from CS25.807.

Considering the CS25.807 requirements, the location of the cabin within a BWB aircraft and the lack of detailed exit designs in literature, the exit design of a BWB cabin is not straightforward. An additional issue is the presence of hydrogen tanks next to and behind the cabin, which limits the placement of exits there. Since this work focuses on the conceptual design of a BWB aircraft, a detailed analysis of the emergency evacuation performance is not performed. Instead, three cabin design options are considered and their effects on the overall aircraft layout and performance are evaluated. The following cabin design options are considered:

1. **Additional LE Doors.** No rear doors are placed while ignoring the sidewall length constraint from CS25.807. Instead, an increased number of doors are placed at the cabin leading edge. This choice

is supported by findings from Chen et al. [85], where evacuation simulations were performed for a 4 bay, 380 passenger BWB cabin. One of the evacuation scenarios had the rear doors fully blocked and found the evacuation time to be sufficient with guidance from the cabin crew. A total of 4 front doors were still available in this scenario. To account for the blockage of one side of the cabin (so half of the leading edge doors) additional doors are placed at the leading edge.

2. **Ventral Exits.** Ventral exits are placed at the rear of the cabin which lead sideways and are assumed to satisfy the rear door requirement from CS25. To account for the ventral exits an area next to the cabin is kept free from hydrogen tanks, the width of this area is based on the B727 ventral exit size. An additional margin is taken to account for structural elements and/or a protective wall.

3. **Max Sidewall Length.** No rear doors are placed to avoid issues with the tank placement or centerbody structure. This will however violate the rear door requirement from CS25. The CS25.807 requirement on distance between exits is imposed on the cabin sidewall length. Half of this distance is taken as the maximum sidewall length (9.15 m). This means that the cabin will have an increased number of bays, increasing the cabin width drastically.

Note that the number of doors placed is dictated by the allowed number of passengers per door from CS25.807. The number of doors placed will in turn have an effect on the length of the cabin, as spanwise aisles are placed between the doors. In Figure 3.5 an example diagram is given of the different cabin exit design options. For simplicity a one class configuration is shown, however in the design tool a two class configuration is assumed (business and economy).

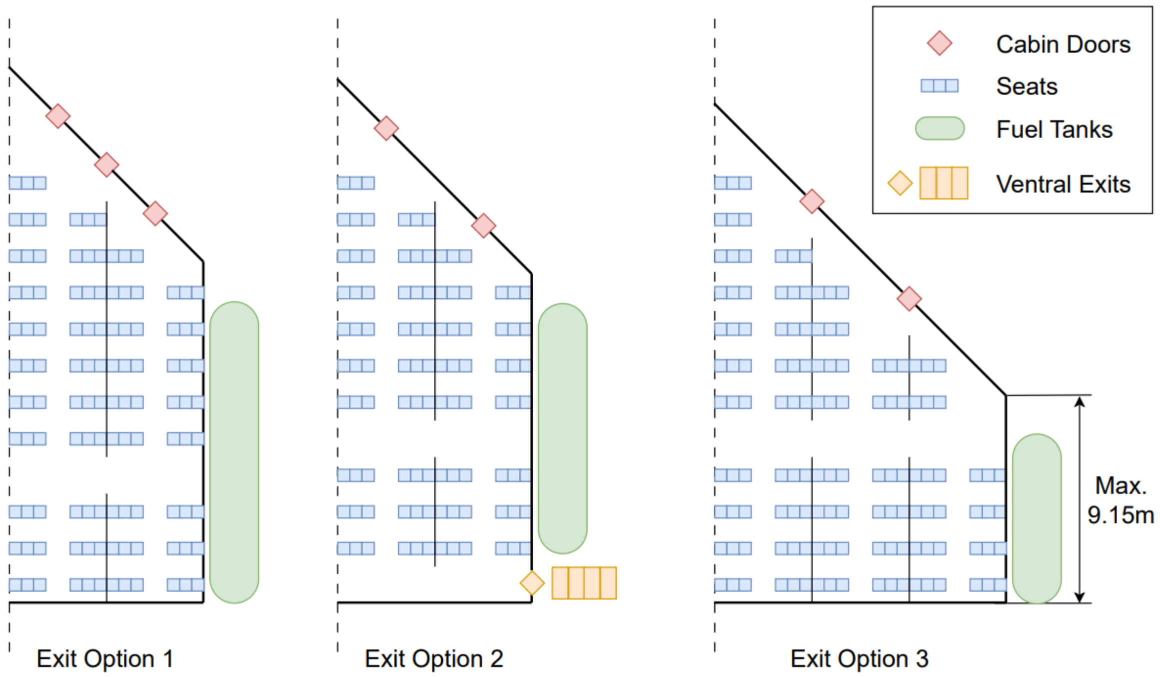

Figure 3.5: Diagram showing the different cabin exit design options

3.3.2. Geometry Parameterisation

Since the generation of the aircraft needs to be performed automatically in a parametric model, an efficient and flexible parameterisation of the geometry is required. This is based on the parameterisation used in Karpuk et al. [17], with some modifications. For this work a tank region behind the cabin is added and a consistent sweep angle of the cabin leading edge (cabin front wall) and the side tank region leading edge (front wall) is maintained. It must be stressed that this means the cabin sweep angle (Λ_{cab}) input determines the leading edge sweep angle of both the centerbody and the transition region. The actual airfoil leading edge sweep of the cabin region will be different due to the addition of the cockpit at the nose. The airfoil leading edge in this region will connect from the cockpit nose to the start of the side tank region leading edge. The top view of the geometry parameterisation is shown in Figure 3.6.

Note that the internal geometry (so excluding the lifting surface constructed using airfoils) is symmetric in z-direction, to avoid complicating the placement of components. As no lateral stability analyses will be performed in this work the outer wing does not have a dihedral angle. Logically, the entire aircraft is symmetric about the centerline (symmetry line is indicated in Figure 3.6).

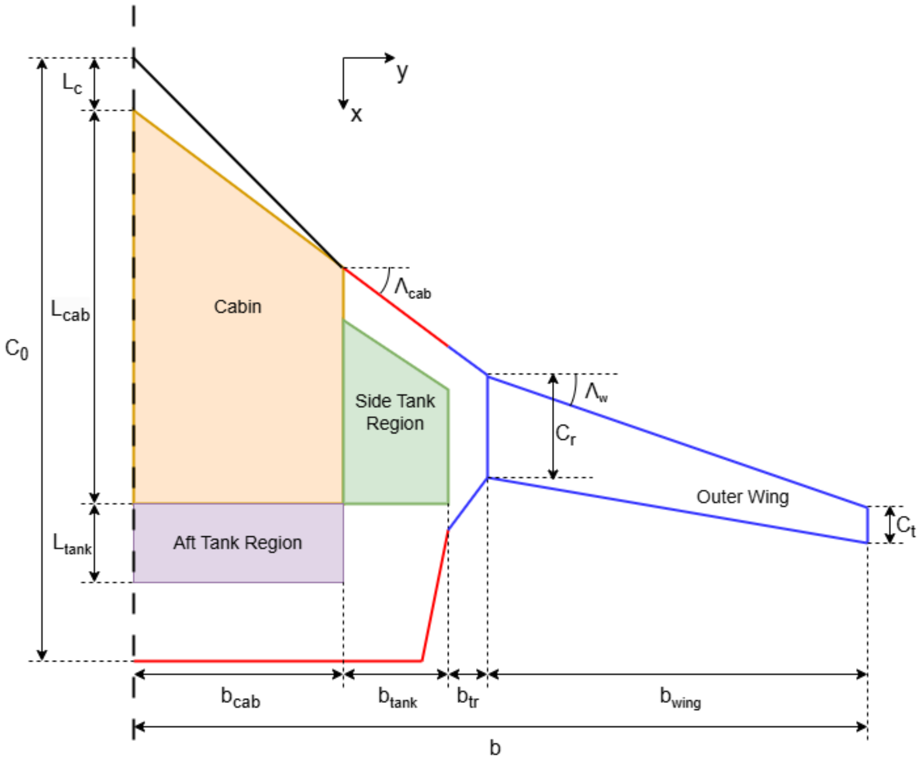

Figure 3.6: Planform parameterisation of generated BWB concepts

3.3.3. Baseline External Geometry

After sizing and generating the internal geometry the external geometry needs to be defined. As mentioned earlier a number of airfoil profiles are placed along the span of the aircraft. The outer shape is then created by lofting along those airfoil profiles. Each airfoil profile will have a position, airfoil shape, thickness, twist and chord. The position is based on the geometry parameterisation earlier described, while the chord and thickness are determined by either fitting of the airfoil around the internal geometry or user inputs (for the outer wing). The airfoil shape and twist have an effect on the aerodynamic performance and stability. Since the conceptual design tool should allow efficient evaluation of different variants and comparisons between those variants will be made it is decided to avoid optimisation of airfoil shapes. Instead, baseline airfoil shapes are taken from the BWB design from Qin et al. [11]. As will be explained later, the twist distribution will be subject to an optimisation. The baseline twist distribution will also be based on Qin et al. [11].

The centerbody region of the aircraft is defined as the region within the cabin and side tank span. The centerbody airfoil section shapes and baseline twists are taken from Qin et al. [11]. Up to 60 % of the centerbody span the reflexed airfoil shape shown in Figure 3.7 is used. From 75 % of the centerbody span until the start of the transition region a symmetric airfoil shape is used. Between 60 and 75 % of the centerbody span the airfoil shape is an interpolation between the reflexed and symmetric airfoils. For the outer wing the supercritical airfoil shown in Figure 3.8 is used. The airfoil shape in the transition region is an interpolation between the symmetric and supercritical airfoils.

The baseline twist distribution is based on the twist distribution given in Qin et al. [11]. Since the spanwise position of the airfoil sections is different compared to Qin et al. [11], it is replicated as much as possible. In Figure 3.9 the twist distribution from Qin et al. [11] is shown, while in Figure 3.10 the baseline twist distribution used in this work is shown. The twist angle of the airfoil sections is defined as being positive for a nose up rotation of the airfoil. Note that the spanwise position of the sections may vary across different concept variants and the twist angles will be included in a design optimisation. The twist angles of the first three centerbody sections (the most central ones) are constant across those sections to avoid large jumps in twist angle due to the close spanwise proximity of those sections. Those large jumps are observed to cause large lift coefficient spikes in the AVL computations.

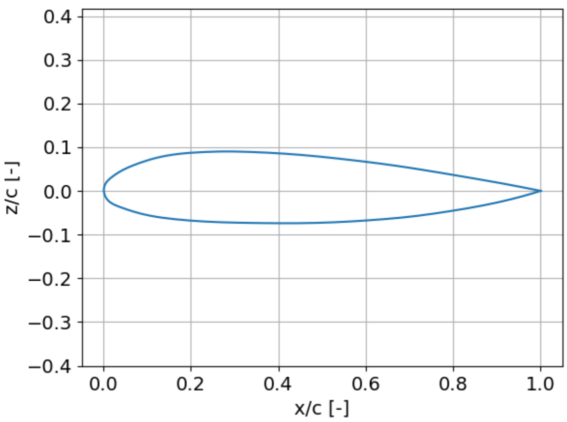

Figure 3.7: Reflexed centerbody airfoil profile [11]

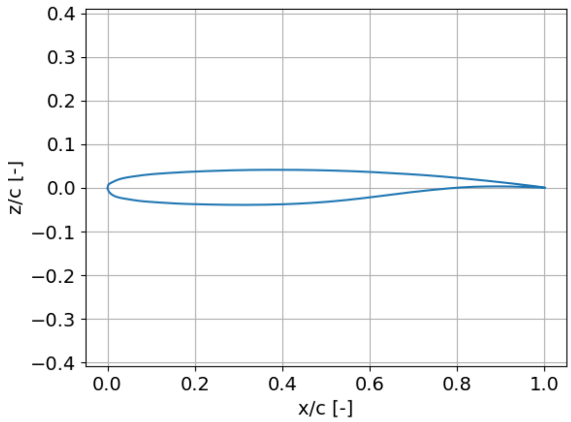

Figure 3.8: Supercritical outer wing airfoil profile [11]

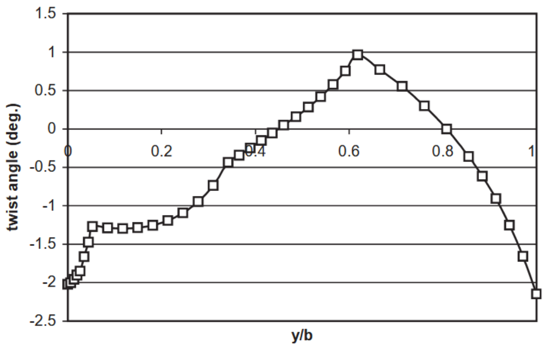

Figure 3.9: Twist distribution of the reference BWB geometry [11]

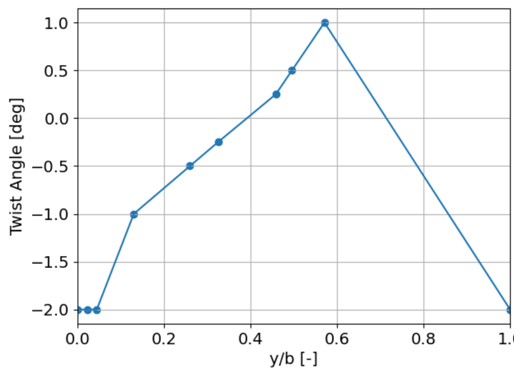

Figure 3.10: Baseline twist distribution of a typical BWB concept generated by own design tool

3.3.4. Fuel Tank and Airfoil Fitting

With the cabin sized, the fuel tanks can be placed around the cabin. As shown in Figure 3.6 there are two regions in which the tanks can be placed. The amount of tanks to be placed in each region depends on the fuel fraction of the total fuel per region, which is determined by the user as an input. The total required fuel mass follows from Breguet range equation applied in the Class 1 weight estimation. Then the total fuel volume can be computed using the density of LH_2, which is $71\,kg/m^3$ [7]. The available fuel volume in a tank is based on the tank sizing method, which is explained in detail in section 3.5. The placement of fuel tanks is done automatically by the design tool for both the side and aft fuel tanks.

Side Fuel Tank Fitting

The method to fit the side fuel tanks is based on the method described in Karpuk et al. [17]. The tanks are placed side by side next to the cabin, fitting between the front wall of the tank region and the aft wall of the tank region. The aft wall of the side tank region can be moved based on the margins required for optional rear ventral exits. A top view of the side tank fuel region is shown in Figure 3.11 and a rear view of the fuel tank region is shown in Figure 3.12. Note that w_d is the rear door margin, which depends on the exit design and required margin for potential rear doors. The height of the outboard side tank region wall ($h_{t,s}$) is a user input.

The hydrogen tanks are assumed to be cylindrical tanks with hemispherical end caps, as this is the most extensively researched tank shape based on the literature findings presented in subsection 2.2.1. As can be seen in Figure 3.12 in the y-z plane the tanks are circles fitted in a trapezoid. Karpuk et al. [17] uses a method to fit diameters in a trapezoid, with the maximum possible diameter. As found in subsection 2.2.1 the diameter of hydrogen tanks should be as high as possible to achieve better gravimetric efficiencies. This fitting method is therefore used to determine the tank diameters, the resulting spanwise position of each tank and the corresponding length of each tank (based on the front and aft wall positions at that spanwise station). An optimisation algorithm can vary the side tank region span to find the span at which the available fuel volume in the side tanks satisfies the required fuel volume for this tank region. Some jumps in volume are present when a new tank is added. To solve this, if the optimiser is unable to find a span that satisfies the volume requirement a second optimisation is performed that applies small variations to the outboard wall height to satisfy the volume requirement.

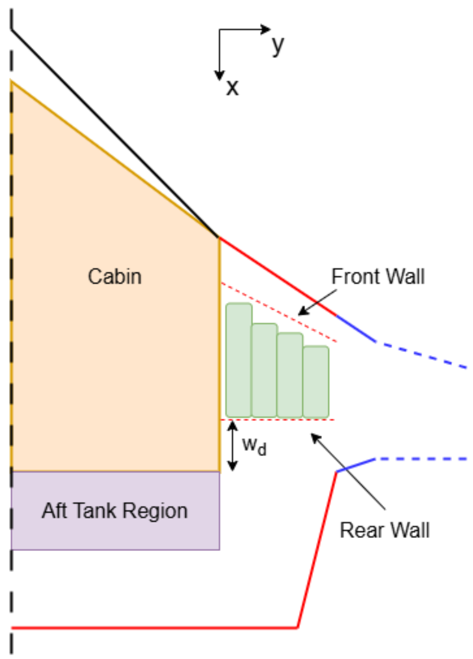

Figure 3.11: Top view of side tank region

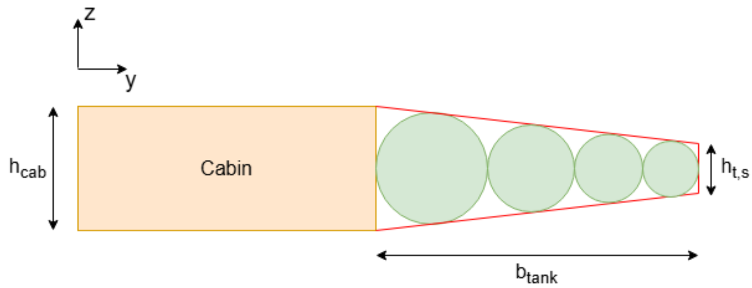

Figure 3.12: Rear view of side tank region

Aft Fuel Tank Fitting

A similar method is used to fit the tanks in the aft fuel tank region. The procedure for this is slightly more complex as the airfoil fitting depends on the length of this region. A top and side view of the aft tank region are given in Figure 3.13 and Figure 3.14, respectively.

The position of the trailing edge of the centerbody is determined using the airfoil fitted around the cabin sidewall. The aft wall of the centerbody internal components is placed at 75 % chord of this airfoil section, while the front wall of the cabin is placed at 10 % chord of this section (based on the values used in Karpuk et al. [17]). This is indicated in Figure 3.14. The height of the aft wall is the cabin height if there are no aft tanks, however when aft tanks are placed determining this height is more complex. In this case the airfoil thickness is scaled such that there is enough height for the cabin at the location of the cabin aft wall. From this scaling the available height at the tank region aft wall is determined.

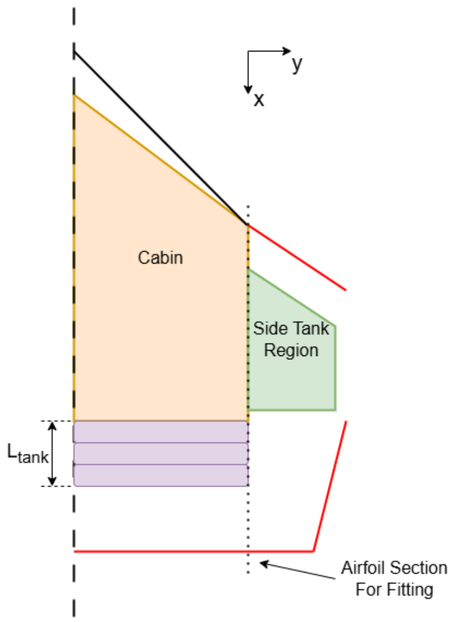

Figure 3.13: Top view of aft tank region

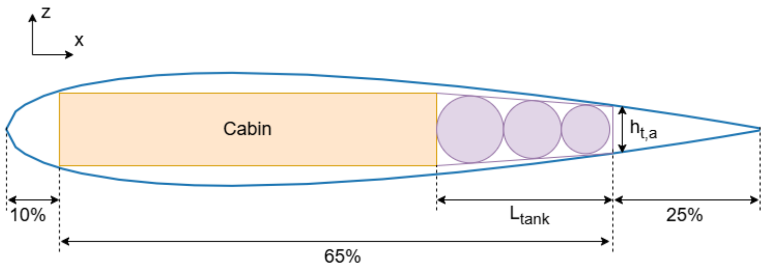

Figure 3.14: Side view of aft tank region

Viewed from the side, this forms a trapezoid shape in which circles can be fitted using the method from Karpuk et al. [17]. Again an optimisation algorithm is used which can vary the aft tank region length, finding the optimal tank region length to satisfy the required fuel volume in this region. Some modifications are made to this algorithm, as the length of the tanks depends on the available center-body width and is equal for all tanks. This causes a jump in available fuel volume when a new tank is added, which results in the optimiser not finding a suitable tank region length in some cases. To fix this, the tank region length which results in the closest matching fuel volume is computed, after which the length of the last tank is corrected to match the required fuel volume. An example of this is given in Figure 3.15. When both side tanks and aft tanks are present, a margin of 0.5 m is taken at the rear of the cabin between the two tank regions to account for fuel system components attached to the tanks. This margin is also taken into account when ventral exits are placed at the rear of the cabin.

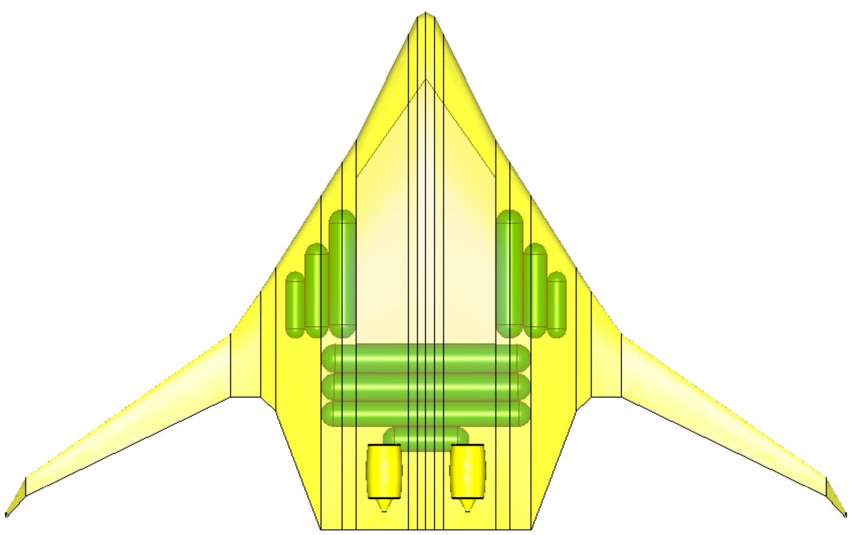

Figure 3.15: Example of modification of length of last aft tank to satisfy required fuel volume

Airfoil Fitting

As the internal components are now all placed, the outer geometry can be fitted around the internal components which results in the lifting surface of the BWB aircraft. As mentioned earlier, the position of the trailing edge of the centerbody is determined during the fitting of the aft tanks. All the other centerbody airfoil sections will have the same trailing edge position, leading to a straight trailing edge. Determination of the leading edge of each section follows from the front edge of the internal geometry being at 10 % chord of the airfoil section. With the leading edge and trailing edge positions known, the chord of each airfoil section is also known. The position and height of the aft wall of the internal geometry is then used to determine the required thickness to chord ratio of each airfoil section. A margin in the required airfoil height at the aft wall position is taken to account for structural elements.

It must be noted that the airfoils are fitted with no twist angle, while the internal components are aligned with the aircraft reference frame. After fitting the airfoils the airfoil twist is applied. In chapter 4 it will be verified whether the airfoil fitting is done sufficiently, without any components clipping through the outer skin.

The outer wing is sized following the method from Karpuk et al. [17]. The centerbody planform area follows from the internal components, while the total planform area is known from the Class 1 sizing. The root chord of the outer wing is determined based on the aircraft span and required outer wing planform area. The transition region span is 7.5 % of the total span. This is to create a smooth transition in thickness from the centerbody to the outer wing. An additional airfoil section is placed between the centerbody and start of the transition region with its trailing edge more forward than the centerbody trailing edge. This ensures a more smooth transition from the centerbody to the outer wing at the trailing edge.

A constraint is placed on the outer wing aspect ratio and root chord. As a certain wing loading is required from the constraint analysis, based on the estimated MTOM a certain total planform area is required. The required centerbody planform area turns out to be large, which is a result of the hydrogen tanks and cabin area required for an LH_2 BWB aircraft. This means in many cases the required outer wing planform area to match the required total area is very small or even negative. To avoid the generation of unfeasible or unrealistic outer wing shapes the aspect ratio is defaulted to 10 if the aspect ratio is higher than 10 or negative (which is a result of the very low/negative planform area). The root chord is constrained with a minimum value of 5 m for aircraft with more than 300 passengers, and a minimum of 4 m for aircraft with less than 300 passengers. The outer wing is generated up to the total wing span which is a user input. A conservative value of 10 is chosen to ensure aerodynamic efficiency of the outer wing while keeping confidence in the structural weight estimate of the outer wing by avoiding very high aspect ratios. If outer wing constraints are enforced, the actual wing loading of the concept will be different from the estimated wing loading from the constraint analysis. The user can input other geometrical parameters of the outer wing, such as the thickness to chord ratio, taper ratio and leading edge sweep angle. A winglet is also generated at the wing tip, with constant inputs. The winglet has a cant angle of 30°, a leading edge sweep angle of 60°, a taper ratio of 0.32 and a length of 4 m. As will be explained in more detail in section 3.8 the lateral stability of the BWB concepts is not considered. This means there is no method which sizes the winglets and any vertical tails according to stability requirements.

Assumed reference values that are used in the geometry definition of the BWB concepts are listed in Table 3.3.

Table 3.3: Assumed reference values for the BWB geometry definition

Parameter	Value	Unit
Economy Seats Fraction	90	%
Business Seats Fraction	10	%
Economy Seats Abreast	3-3	-
Business Seats Abreast	2-2	-
Cabin Height	3.2	m
Cabin Bay Width	3.48	m
Front Bulkhead Chordwise Position	10	%
Rear Bulkhead Chordwise Position	75	%
b_{tr}/b	0.075	-
Winglet Cant Angle	30	deg
Winglet Leading Edge Sweep Angle	60	deg
Winglet Taper Ratio	0.32	-
Winglet Length	4	m
Outer Wing Aspect Ratio Limit	10	-

3.4. Aerodynamic Analysis Model

A crucial part of the conceptual design tool is the aerodynamic analysis model. As mentioned in section 2.4 the unconventional nature of BWB aircraft complicates the usage of low fidelity aerodynamic models. For this work methods from literature are selected which have been applied to BWB aircraft in earlier studies. Validation of the methods in those studies and validation of the methods used in this work will improve the confidence in the aerodynamic model. This will be explained in detail in chapter 4.

3.4.1. Pressure Forces

For the pressure forces a vortex lattice method is used. Besides being computationally efficient, the method has been used in several earlier BWB studies in which the accuracy of the method has also been proven sufficient (refer back to subsection 2.4.1). As the design tool is made in ParaPy, the choice is made to use AVL to compute the pressure forces. ParaPy offers a direct link between the generated geometry from ParaPy and the input for AVL, which improves consistency between the generated geometry and the AVL input. Flight conditions are automatically computed and set by the design tool depending on the cruise condition inputs chosen by the user.

3.4.2. Drag Components

The AVL analysis computes the induced drag using the Trefftz plane analysis [57], however it is unable to compute the viscous drag components. Those components are therefore computed using other methods. The drag buildup method explained in Gur et al. [86] is used as a reference to compute the total drag of the aircraft. The full drag buildup includes the induced drag (computed by AVL), profile drag and wave drag. Following Gur et al. [86] the additional profile drag due to lift is ignored, as it is small. The interference drag is also ignored, as it is assumed that variations in thickness are smooth enough to not cause significant interference drag.

Profile Drag

For the profile drag the basic method explained in Gur et al. [86] is used. The profile drag for each individual external aircraft component is computed using Equation 3.13, where C_f is a flat plate friction coefficient, S_{wet} is the wetted surface area of the component, S_{ref} is the reference wing area of the aircraft and FF is the form factor of the component. The total profile drag coefficient is found by summing all the individual components. The lifting surface is divided in trapezoidal wing elements by AVL, which are used for the profile drag computation. The profile drag of the nacelles is also computed.

$$C_{D_p} = C_f \mathrm{FF} \frac{S_{wet}}{S_{ref}} \tag{3.13}$$

First the flat plate friction coefficient needs to be determined. A composition of the laminar and turbulent friction coefficients is computed based on the length of the laminar and turbulent flow regions. To determine the length of each region the transition point is estimated. Based on a diagram given in Gur et al. [86], an assumed technology factor of 0 and the leading edge sweep angle of the trapezoidal wing elements being over 30°, the transition Reynold number is assumed to be 4×10^6. In case the leading edge sweep angle of a wing element is lower than 30° this transition Reynolds number is a conservative number, as later transition would be expected for lower sweep angles. Based on the total Reynolds number of the wing element and the transition Reynolds number the location of the transition point can be computed. The laminar friction coefficient is computed using the Blasius relation (Equation 3.14) and the turbulent friction coefficient is computed using the compressible Schlichting relation (Equation 3.15). The form factors are computed using the relations given in Moens [59]. For the wing form factor Equation 3.16 is used and for nacelles Equation 3.17 is used. Note that t/c is the thickness to chord ratio of the wing element and $\Lambda_{c/2}$ is the half chord sweep angle of the wing element.

$$C_{f,lam} = \frac{1.328}{\sqrt{Re}} \tag{3.14}$$

$$C_{f,turb} = \frac{0.455}{(\log_{10} Re)^{2.58}(1+0.144M^2)^{0.65}} \tag{3.15}$$

$$\mathrm{FF}_{wing} = \left[3.4004\frac{t}{c} - 0.4578\left(\frac{t}{c}\right)^2 + 13.0119\left(\frac{t}{c}\right)^3\right]\cos^2\Lambda_{c/2} + 1 \tag{3.16}$$

$$\mathrm{FF}_{nac} = 1 + 0.35\frac{D_{nac}}{L_{nac}} \tag{3.17}$$

For the engine nacelle drag computation the method from Moens [59] is used. The nacelle is composed of two casings, one for the engine fan and one for the engine core. The profile drag for each casing is computed separately, after which they are combined to compute the total nacelle profile drag. To compute the total nacelle profile drag Equation 3.18 is used. Q_N is an interference coefficient which accounts for interference effects between the engine nacelle and the aircraft surface. This coefficient depends on the distance between the nacelle and the aircraft surface and is determined using the method from Moens [59]. For the nacelle drag the flow is assumed to be fully turbulent, which means the turbulent flat plate friction coefficient is used. The Reynolds number depends on the length of the nacelle.

$$C_{D_{eng}} = N_{eng}\left(Q_N C_{D_{nac1}} + C_{D_{nac2}}\right) \tag{3.18}$$

Parasite drag from small components such as probes or antennas is added as a constant percentage of the total profile drag. Similar to Moens [59] 2.5 % is added.

Wave Drag

Since the BWB aircraft will be operating at high Mach numbers in cruise, the wave drag needs to be determined. When using empirical relations this is not straightforward for BWB aircraft, as those relations are for conventional aircraft configurations. Still, empirical relations are used to compute the wave drag, with some modifications based on findings in literature. Similarly to the profile drag computation the wing elements used by AVL are used for the wave drag computation. The wave drag for each wing element is computed and the total wave drag is found by summing all the individual contributions.

First the divergence Mach number of a wing element is computed using the Korn equation extended with simple sweep theory, which is given in Equation 3.19 [87]. The Korn coefficient κ_A depends on the airfoil and the values are taken from Gur et al. [86]. For supercritical airfoils a Korn factor of 0.95 is used and for conventional airfoils a Korn factor of 0.87 is used. The lift coefficient C_L of each wing element is available from the AVL results. The critical Mach number can now be determined using Equation 3.20.

$$M_{DD}\cos\Lambda_{c/2} + \frac{C_L}{10\cos^2\Lambda_{c/2}} + \frac{t/c}{\cos\Lambda_{c/2}} = \kappa_A \tag{3.19}$$

$$M_{cr} = M_{DD} - \sqrt[3]{\frac{0.1}{80}} \tag{3.20}$$

With the critical Mach number now known, Lock's fourth power law can be used to compute the wave drag per wing element (Equation 3.21 [88]. If the freestream Mach number is larger than the critical Mach number Lock's fourth power law is used to compute the wave drag of the wing element. If not, no wave drag is added.

$$C_{D_w} = 20(M - M_{cr})^4 \frac{S_{ref}}{S_{wet}} \tag{3.21}$$

At first this method was applied to the whole BWB geometry, however this resulted in unrealistically high wave drag values. This prompted further research into wave drag of BWB aircraft. Wave drag results from the CFD analysis performed in Qin et al. [11] show that a negligible amount of wave drag is present over the thick centerbody of the BWB aircraft (as shown in Figure 3.16). Sargeant et al. [89] supports these findings, showing strong shocks over the centerbody with a 2D aerodynamic calculation. However, a 3D Navier-Stokes calculation does not show any strong shocks over the thick centerbody due to 3D pressure relief effects. Lyu and Martins [90] shows similar findings with a CFD analysis of a BWB aircraft. Strong shocks are observed over the transition region and outer wing, but no shocks over the centerbody as shown in Figure 3.17. In Qin et al. [11] the wave drag diminishes from a t/c of around 12 %. In Sargeant et al. [89] it is mentioned no wave drag is present over the thick centerbody with a t/c of 14 %. Based on these findings it is decided to ignore the centerbody in the wave drag calculations and only calculate the wave drag for the transition region and outer wing. A limit of 15 % is also imposed on the t/c of a wing strip, meaning if the t/c exceeds this value the wave drag is assumed to be 0 due to the thickness effects observed in literature. The absolute sweep angle of a wing strip is limited to 70° to avoid unrealistic spikes in wave drag. Mason [87] only includes empirical data for sweep angles up to 70°, thus this sweep angle is taken as the limit.

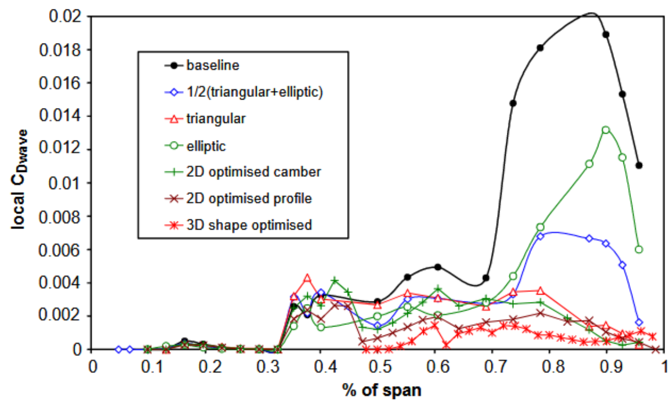

Figure 3.16: Spanwise local wave drag coefficient distribution over a BWB aircraft [11]

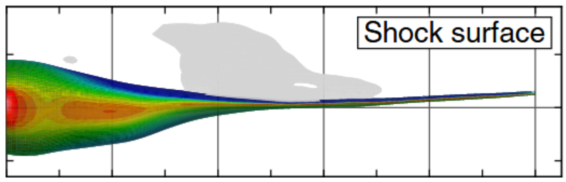

Figure 3.17: Shocks (indicated in gray) over a BWB aircraft surface [90]

3.4.3. Optimal Lift Coefficient Estimate

For evaluating the maximum achievable L/D of a concept, the optimal lift coefficient is estimated. This is done to avoid evaluating the L/D at a sweep of lift coefficients, which is computationally expensive (especially when performing the sensitivity analysis). As a simplification to avoid large computation times, the drag polar of the concepts is assumed to follow the standard form, which is given in Equation 3.22. Using this assumption the optimal lift coefficient for maximum L/D can be estimated, which results in Equation 3.23. The aspect ratio A is known from the aircraft geometry, however the span efficiency factor e and C_{D_0} need to be determined. As is found later in section 4.1 the optimal lift coefficient typically lies between 0.2 and 0.3. For this reason the span efficiency factor and C_{D_0} at a lift coefficient of 0.25 are used to estimate the optimal lift coefficient. Knowing the optimal lift coefficient, the aerodynamic model is run again to estimate the maximum L/D.

$$C_D = C_{D_0} + \frac{C_L^2}{\pi A e} \tag{3.22}$$

$$C_{L,opt} = \sqrt{C_{D_0} \pi A e} \tag{3.23}$$

Assumed reference values used in the aerodynamic analysis method used in this work are summarised in Table 3.4

Table 3.4: Assumed reference values for the aerodynamic analysis method

Parameter	Value	Unit
Profile Drag Technology Factor	0	-
Transition Reynolds Number	4×10^6	-
Parasite Drag/Profile Drag	0.025	-
Conventional Airfoil Korn Factor	0.87	-
Supercritical Airfoil Korn Factor	0.95	-
Wave Drag t/c Limit	0.15	-
Wave Drag Leading Edge Sweep Limit	70	deg

3.5. Liquid Hydrogen Tank Sizing

To assess the effect of different tank sizes and aspect ratios (length to diameter ratio) a tank sizing method based on methods from literature is included in the conceptual design tool. The aim of this sizing method is to make an estimate of the tank mass and available hydrogen volume in the tank based on the outer shell geometry of the tank. Note that the sizing model computes the available hydrogen volume, as the outer shell geometry of the tanks is determined by the available room in the aircraft's interior. An optimiser then finds the required size of the tank regions (and thus the size, shape and number of tanks) to satisfy the required fuel volume. The sizing method is incorporated in the Class 1 – Class 2 iterations and subsequent optimisation, meaning long computation times are to be avoided.

The tanks in this work are assumed to be cylindrical, non-integral tanks with hemispherical end caps. The structural shell is made out of Aluminium 2219-T851 (based on Onorato et al. [43]), while the insulation material used is polysterene (based on Tarbah [74]). The tanks consist of an outer insulation layer and inner structural shell, as shown in Figure 3.18. This choice is based on the tank design described in Onorato et al. [43]. The tank is non-integral, which means mounting points are required for the tanks. The mass of those mounting points is included in the structural sizing explained in subsection 3.5.1. The outer tank radius r_{tank} and tank length L_t follow from the tank fitting discussed in subsection 3.3.4. The structural and thermal sizing of the tank determine the structural thickness t_s, insulation thickness t_{in} and resulting inner radius r_i. As mentioned in subsection 3.3.4 the tanks are fitted based on a required fuel volume in an iterative manner using an optimisation algorithm. As the available fuel volume of a tank depends on the thickness of the structural and insulation layers of the tank, for each iteration in this optimisation those layers are sized.

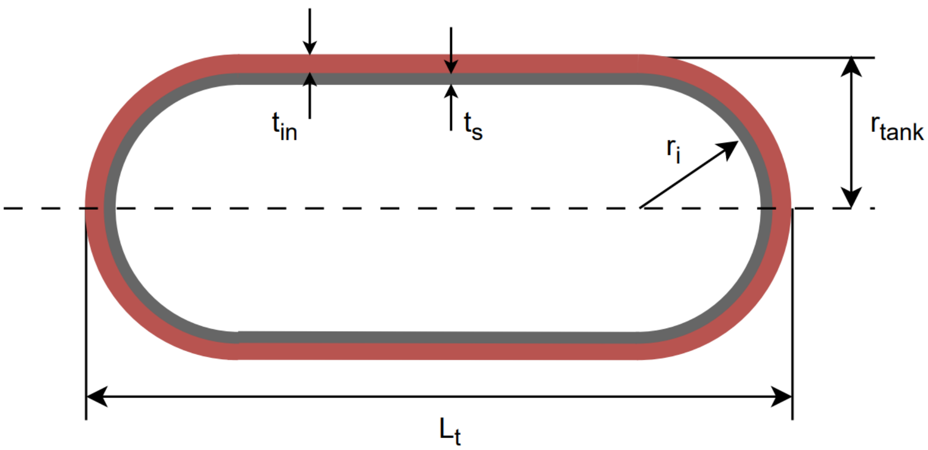

Figure 3.18: Diagram of LH_2 storage tank

3.5.1. Structural Sizing

The structural sizing is performed using the method described in Onorato et al. [43]. This method sizes the structural shell thickness according to the pressure loads acting on the tank. Tank and material properties used in the sizing of the structural shell are given in Table 3.5. The properties are taken from Brewer [7], which are also used by Onorato et al. [43]. For the maximum pressure in the tank a higher value is assumed to make a conservative estimate of the structural shell thickness. To compute the thickness of the cylindrical part of the structural shell Barlow's formula is used (Equation 3.24). The maximum pressure P_{max} is a design choice, while the ambient pressure P_{amb} depends on the flight altitude. Note that the ambient pressure is used, meaning the tanks are not placed in the pressurised part of the centerbody. The radius used for sizing the structural shell is the tank outer radius. As the outer radius, structural shell thickness and insulation thickness are all dependent on each other, another iteration loop is avoided by assuming the structural shell radius to be the outer tank radius. This is a conservative assumption as the actual radius of the structural shell will be lower than the tank outer radius due to the insulation thickness. This means the required structural thickness will be higher than the thickness that would be found with an iteration loop. The weld efficiency e_w is taken from Brewer [7].

Table 3.5: Tank properties used for structural sizing [7, 43]

Parameter	Value	Unit
Maximum Tank Pressure	4	bar
Design Stress Aluminium 2219-T851	172	MPa
Ultimate Stress Aluminium 2219-T851	234	MPa
Stress Ratio R_1	0.43	-
Weld Efficiency	0.8	-
Density Aluminium 2219-T851	2840	kg/m^3

$$t_s = \frac{(P_{max} - P_{amb}) \cdot r_{tank}}{\sigma \cdot e_w} \tag{3.24}$$

As explained in Onorato et al. [43], determination of the design stress σ is done by applying the Goodman relation twice to account for fatigue limits. Equation 3.25 is used to compute the fatigue limit for reversed loading, where $\sigma_{a,-1}$ is the fatigue limit, σ_{a,R_1} is the design stress of the material, σ_b is the ultimate stress of the material and R_1 is the stress ratio (ratio between maximum and minimum stress experienced by the material). The values for reversed loading are all taken from Brewer [7]. The same relation is used again with Equation 3.26 to obtain the design stress for the structural shell. Note that the stress ratio R_2 depends on the minimum and maximum stress experienced by the structural shell. As this is directly proportional to the pressure difference in the tank, the ratio between the minimum and maximum pressure difference is used to determine R_2.

$$\sigma_{a,-1} = \frac{\sigma_{a,R_1}}{1 - \frac{\sigma_{a,R_1} \cdot 0.5 \cdot (1+R_1)}{\sigma_b}} \tag{3.25}$$

$$\sigma = \frac{\sigma_{a,-1}}{1 - \frac{\sigma_{a,-1} \cdot 0.5 \cdot (1+R_2)}{\sigma_b}} \tag{3.26}$$

The structural thickness of the spherical end caps is half of the computed structural shell thickness [43]. The mass of the support structure is 1.8 % of the total tank mass (including fuel) and is added after computing the total tank mass. This means the assumption is made that the support mass increases linearly with the tank mass [43].

3.5.2. Thermal Sizing

As no detailed mission analysis with timesteps is performed, it is not possible to evaluate the time-based pressure evolution in the tank. Instead, the insulation thickness will be sized based on a required boil-off rate. This required boil-off rate is based on a dormancy time of 12 hours, which represents overnight parking of the aircraft (based on findings from Huete and Pilidis [39]). The dormancy time is the time it takes for the gaseous hydrogen in the tank to reach the maximum pressure of the tank when the tank is not being used. The method explained in Tarbah [74] will be used with some modifications. The tank is modelled as multiple thermal layers with each their own thermal resistance. In Figure 3.19 the different layers are shown. The tank properties used in the thermal sizing are given in Table 3.6. Note that the air temperature around the tank is assumed to be equal to the ambient temperature. The ambient temperature T_{amb} and hydrogen temperature T_{H_2} are known, while the other temperatures will depend on the heat rate into the tank and the thermal resistance of each layer.

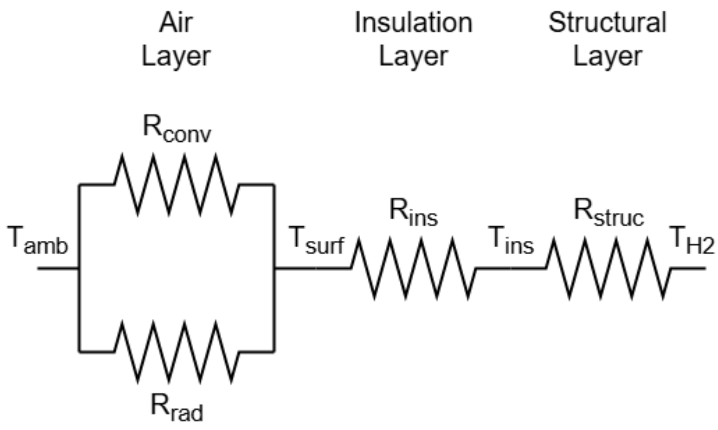

Figure 3.19: Thermal layers used to perform thermal sizing

Table 3.6: Tank properties used for thermal sizing [74, 91, 92]

Parameter	Value	Unit
Ambient Temperature	288.15	K
Dormancy Time	12	hrs
Hydrogen Temperature	20	K
Hydrogen Density	70.85	kg/m^3
Hydrogen Heat of Evaporation	447	kJ/kg
Emissivity Insulation	0.9	-
Conductivity Aluminium 2219-T851	120	W/m/K
Conductivity Polysterene	0.022	W/m/K
Conductivity Air	0.0255	W/m/K
Polysterene Density	32	kg/m^3

The heat rate into the tank depends on the boil-off rate and is computed using Equation 3.27, where $\dot{Q}$ is the heat rate into the tank in W, $\dot{m}_{bo}$ is the hydrogen boil-off rate in kg/s and ΔH_e is the heat of evaporation of liquid hydrogen in J/kg. The maximum boil-off rate that is used to compute the heat rate into the tank is taken from Tarbah [74] and scaled according to the tank volume. As will be discussed further in section 4.2 the boil-off rate scaling based on Tarbah [74] is tuned using gravimetric efficiency results from Huete and Pilidis [39] for a similar tank with a dormancy time of 12 hours. Using Equation 3.28 the required boil-off rate is computed. Note that this means the required boil-off rate is assumed to scale linearly with the total tank volume.

$$\dot{Q} = \dot{m}_{bo} \cdot \Delta H_e \tag{3.27}$$

$$\dot{m}_{bo} = 1.12 \cdot 10^{-4} \cdot V_{tank} \tag{3.28}$$

After determining the required heat rate into the tank the thermal resistance of each layer is computed. First the thermal resistance between the surrounding air and the tank surface is computed. As can be seen in Figure 3.19 radiation and convection is taken into account. The radiation heat transfer coefficient is computed using Equation 3.29, where σ_{bolt} is the Stefan-Boltzmann constant.

$$h_{rad} = \sigma_{bolt} e_o \left(T_{surf}^2 + T_{amb}^2\right)\left(T_{surf} + T_{amb}\right) \tag{3.29}$$

The convection heat transfer coefficient is computed using Equation 3.30, where D_{tank} is the diameter of the tank, k_a is the thermal conductivity of the ambient air and Nu is the Nusselt number of the tank. The Nusselt number of the tank is computed using Equation 3.31 for which the cylinder Nusselt number is computed using Equation 3.32 and the sphere Nusselt number is computed using Equation 3.33.

$$h_{conv} = \frac{k_a \cdot Nu}{D_{tank}} \tag{3.30}$$

$$Nu = \frac{L_{cyl} \cdot Nu_{cyl} + D_{tank} \cdot Nu_{sph}}{L_{cyl} + D_{tank}} \tag{3.31}$$

$$Nu_{cyl} = \left(0.6 + \frac{0.387 Ra^{1/6}}{\left(1 + \left(\frac{0.559}{Pr}\right)^{9/16}\right)^{8/26}} \right)^2 \tag{3.32}$$

$$Nu_{sph} = 2 + \frac{0.589 Ra^{1/4}}{\left(1 + \left(\frac{0.469}{Pr}\right)^{9/16}\right)^{4/9}} \tag{3.33}$$

The Rayleigh (Ra) and Prandtl (Pr) numbers are computed using Equation 3.34 and Equation 3.35, respectively. In these equations g is the gravitational acceleration, ν_a is the kinematic viscosity of the ambient air and α_a is the diffusivity of the ambient air. The volumetric thermal expansion coefficient β for an ideal gas is the inverse of the temperature, which in this case is the ambient temperature. The values of the kinematic viscosity and diffusivity of the ambient air are computed for the ambient air temperature of 288.15 K, using the approximation relations given in Colozza and Kohout [93].

$$Ra = \frac{g \cdot \beta \cdot (T_{amb} - T_{surf}) D_{tank}^3}{\nu_a \cdot \alpha_a} \tag{3.34}$$

$$Pr = \frac{\nu_a}{\alpha_a} \tag{3.35}$$

After calculating the air layer heat transfer coefficients the total thermal resistance of the air layer can be computed using Equation 3.36. With the thermal resistance of this layer now known, the heat transfer through the layer can be computed using Equation 3.37, where ΔT is the temperature difference across the layer and R is the thermal resistance of the layer. The thermal resistance and temperature difference across a layer both depend on each other, meaning an iteration loop is necessary to find the surface temperature of the tank that satisfies the required heat rate into the tank based on the boil-off rate.

$$R_{air} = \frac{1}{2\pi r_{tank} L_{cyl} + 4\pi r_{tank}^2} \cdot \frac{1}{h_{rad} + h_{conv}} \tag{3.36}$$

$$\dot{Q} = \frac{\Delta T}{R} \tag{3.37}$$

After determining the surface temperature of the tank the conductive heat transfer through the insulation and structural layers is computed. Per Tarbah [74], the conduction through the tank layers can be computed based on the conduction through a sphere and cylinder occurring in parallel. The total conductive thermal resistance of a layer is computed using Equation 3.38. The spherical and cylindrical thermal resistances are computed using Equation 3.39 and Equation 3.40, respectively. In these equations k is the thermal conductivity of the material of the layer, r_o is the outer radius of the layer, t is the thickness of the layer and L_{cyl} is the length of the cylindrical section of the tank.

$$R_{cond} = \left(R_{cond,cyl}^{-1} + R_{cond,sph}^{-1} \right)^{-1} \tag{3.38}$$

$$R_{cond,sph} = \frac{1}{4\pi k} \left(\frac{1}{r_o} - \frac{1}{r_o - t} \right) \tag{3.39}$$

$$R_{cond,cyl} = \frac{\ln \frac{r_o}{r_o - t}}{2\pi L_{cyl} k} \tag{3.40}$$

The allowed heat rate into the tank and the thickness of the structural layer are known from Equation 3.27 and Equation 3.24 respectively, however the thickness of the insulation layer is still unknown. The thermal resistance and therefore temperature of each layer depends on those values. The temperatures of the tank surface and of the hydrogen in the tank are known, while temperatures across layers must be consistent. Based on this an iteration loop finds the insulation thickness and resulting thermal resistance of each layer that satisfy the surface and inside temperature of the tank.

After computing the required thickness for each layer the mass of the tank can be computed using the volume of each layer and the density of the materials. The available volume for the liquid hydrogen fuel is computed using the internal volume of the tank and a number of allowances. Based on Onorato et al. [43] a ullage allowance of 2 % is included, an allowance for contraction and expansion of 0.9 %

is included and an allowance of 0.6 % for internal equipment is included. Mass allowances are also accounted for, which are computed as a percentage of the total tank mass including the fuel mass and are added to the tank mass. A mass allowance of 4.3 % is added for hydrogen required to pressurise the tank, while an allowance of 0.3 % is taken to account for trapped fuel in the fuel system. Note that mass allowances for the hydrogen fuel systems (heat exchangers, pumps, pipes etc) are computed separately in the Class 2 weight estimations, which will be explained in detail in section 3.7.

3.6. Engine Sizing

Based on the required thrust loading from the constraint analysis, the engines can be sized. Normally in the conceptual design phase an existing reference engine is chosen that satisfies the thrust requirement, however due to the parametric nature of this work no discrete engine can be chosen. Instead, data of several state of the art turbofan engines is collected and used to size the engines for this work. This data includes TSFC, dry weight and TO thrust data and dimensions of the engines. The collected data is shown in Table 3.7. For the TSFC of the engine an average is taken from all the reference engines, which is computed to be 13.7 g/kN/s. Based on the literature findings earlier discussed in subsection 2.2.2 no SEC penalties are expected when switching from kerosene to liquid hydrogen (minor improvements were found). This means the TSFC of the hydrogen engines is computed based on the assumption that the SEC is equal to the SEC of kerosene engines. The found average TSFC is therefore corrected based on the lower heating values of kerosene and LH_2, resulting in a TSFC of 4.94 g/kN/s for the hydrogen turbofan engines.

Table 3.7: Engine data used for engine sizing [78, 94]

Engine	**TO Thrust** [kN]	**TSFC** [g/kN/s]	**Diameter** [m]	**Length** [m]	**Dry Weight** [kg]
GEnx	310	14	2.8	4.9	5600
GEnx-2B67	295	14	2.67	4.7	5440
Trent 1000	320	14.3	2.85	4.7	5400
Trent XWB84	374	13.5	3.0	5.8	7300
GE9X	490	-	3.35	5.7	9600
Trent 7000	324	14.3	2.85	4.8	6400
LEAP-1A	130	13.1	1.98	3.3	3150
PW1100G	130	12.9	2.06	3.4	2850

For the sizing of the engines the collected engine data is used. The data is used to construct trendlines relating all geometric and weight properties to the take-off thrust of the engines. Since a required take-off thrust is computed by the design tool, using this thrust and the trendlines the engines can be sized. The trendlines are shown in Figure 3.20, Figure 3.21 and Figure 3.22.

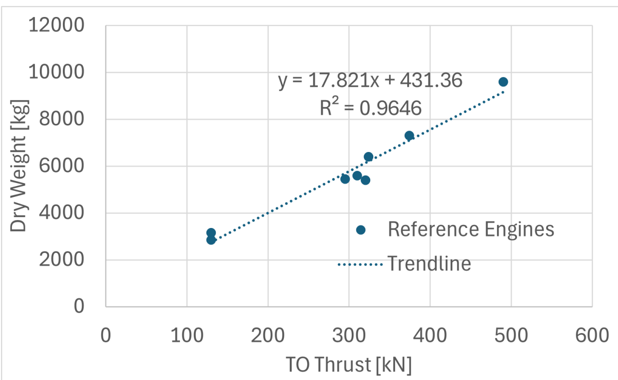

Figure 3.20: Engine TO thrust versus dry weight trendline

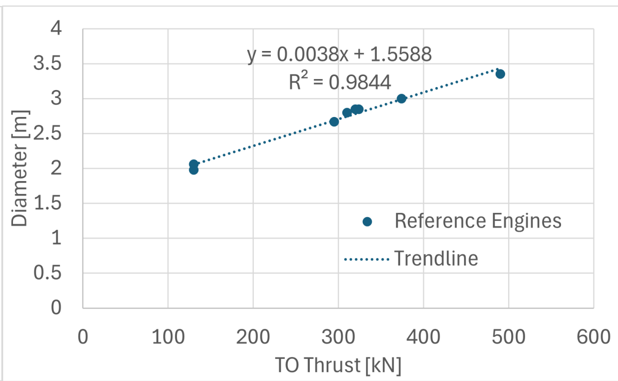

Figure 3.21: Engine TO thrust versus fan diameter trendline

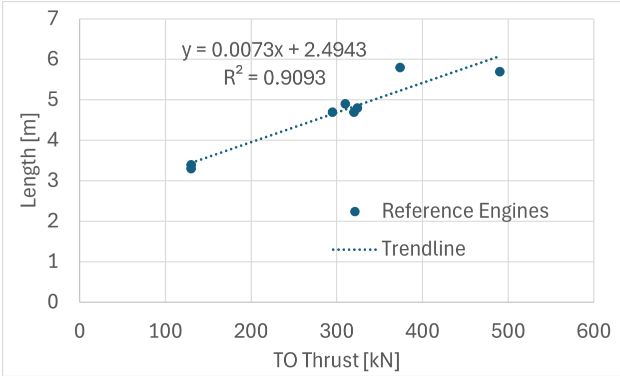

Figure 3.22: Engine TO thrust versus length trendline

After sizing the engines based on the TO thrust a value is added to the fan diameter to account for the engine nacelles. A constant value of 0.6 m is used, which is based on values of the reference engines used. The user of the design tool can choose whether to mount the engines under the wing or on the afterbody. This choice will have effects on the weight estimations of the outer wing and aft body, on the CG of the aircraft and on the nacelle drag (through the interference coefficient Q_N discussed in section 3.4).

3.7. Component Weight Estimation

With the geometry definition, engine sizing and tank sizing complete, the component weight estimation (Class 2 weight estimation) of the aircraft can be performed. Since the BWB concept is an unconventional configuration, special attention is given to the methods used to perform the weight estimations of unconventional components. The Class 2 weight estimation includes the weight of the centerbody, aft body, outer wing, fuel tanks, engines, landing gear and other systems. The fuel tank and engine weight are already computed in the sizing of those components (see the previous sections), while for the landing gear and other systems the empirical Torenbeek relations from Roskam [67] for conventional aircraft are used to estimate the weight. Special attention has been given to the other components, as these cannot be considered similar to conventional aircraft.

3.7.1. Centerbody and Aft Body Weight

Accounting for a large part of the empty weight of the aircraft, adequate estimations of the centerbody and aft body weights is crucial. As explained in section 2.4 the most commonly used method to estimate those weights in literature is the method from Bradley [68]. This method is developed for kerosene BWB aircraft that do not have a large region containing hydrogen tanks next to or behind the passenger cabin. The semi-empirical method was created by performing a FEM analysis on a reference BWB aircraft, for which mass predictions were available from Boeing. A regression analysis was performed to create empirical relations to estimate the structural mass. These relations provided accurate estimations of the centerbody structural weight, compared to the predictions from Boeing. Okonkwo [95] observed decent agreement between the method from Bradley [68] and Howe [71], which is another structural mass estimation method for BWB aircraft. In Okonkwo [95] it was found the method from Howe [71] slightly overestimates the structural weight, while this method also requires several inputs that are hard to obtain at the conceptual design stage.

The method from Bradley [68] divides the centerbody into the front centerbody weight and the aft body weight. The regression formula for the front centerbody is based on the FEM analysis of the pressurised BWB cabin and is given in Equation 3.41. In this equation S_{cab} is the floor area of the passenger cabin in ft^2, the weights are in lbs. In Bradley [68] the aft body is treated as a horizontal tail and its weight is estimated using Equation 3.42, where S_{aft} is the planform area of the aft body, N_{eng} is the number of engines mounted on the aft body and λ_{aft} is the taper ratio of the aft body. With the geometry definition in this work the taper ratio can be 0 in some cases if the center and outboard lengths of the aft body are taken to define the taper ratio. Since a large part of the aft body is rectangular it was chosen to compute an average taper ratio of the aft body (the taper ratio of an equivalent trapezoidal aft body shape). This was done using Equation 3.43, based on the planform area, length of the rectangular area (L_{aft}) and span (b_{aft}) of the aft body.

$$W_{cb} = 5.698865 \cdot 0.316422 \cdot MTOM^{0.166552} \cdot S_{cab}^{1.061158} \tag{3.41}$$

$$W_{aft} = (1 + 0.05 \cdot N_{eng}) \cdot 0.53 \cdot S_{aft} \cdot MTOM^{0.2} \cdot (\lambda_{aft} + 0.5) \tag{3.42}$$

$$\lambda_{aft} = \frac{\frac{2S_{aft}}{b_{aft}} - L_{aft}}{L_{aft}} \tag{3.43}$$

The method explained is created for kerosene BWB aircraft, meaning some modifications are required to account for the structural mass of the hydrogen tank regions. At first the planform area of the side tank region was included in the cabin floor area, while the planform area of the aft tank region was included in the aft body planform area. This yielded significantly higher mass estimations for the front centerbody than expected. The aft body weight estimates did not present issues. Several methods were applied for the front centerbody mass and compared. Jagtap et al. [23] applied the unmodified method from Bradley [68] with a 6 % mass penalty to account for the hydrogen tank regions. This method is tried, as well as considering the side tank region as an outer wing and applying the Torenbeek outer wing weight method from Roskam [67], while computing the cabin weight using the unmodified Bradley method. Another method that is tried is computing the side tank region weight using the aft body Bradley method and computing the cabin weight using the unmodified Bradley method. The final method that is considered also uses the aft body relation, but inputs the number of tanks as N_{eng} in the equation. This offers some physical effects of the structure having to support more or less hydrogen tanks. The estimated front centerbody weights for different side tank region planform areas are given in Figure 3.23. Note that the original centerbody weight method is the method where the side tank area is included in the cabin floor area.

It can clearly be seen that the originally applied method results in very high estimates of the centerbody weight. The overestimation can be explained by the relation for the front centerbody weight being created for a pressurised structure. The side tank regions are not pressurised, meaning including this area in the cabin floor area results in overestimations of the structural weight. The penalty method applied in Jagtap et al. [23] does not account for changes in the side tank area, while the Torenbeek outer wing method results in low weight estimates. Another thing to consider is that the aft tank region structural weight is accounted for with the aft body planform area and the Bradley aft body relation. Drastically different structural weights of the side or aft tank regions could influence the comparison of the overall performance of variants with large differences in fuel distribution. This fact and the uncertainty in what method is the most accurate due to the lack of references from literature, means using different methods for both tank regions could have undesirable effects on the conclusions drawn from this work. It is therefore decided to compute the side tank region structural weight using the aft body relation as well. For both the aft body and side tank region weights the number of tanks placed in each region is used as N_{eng} in Equation 3.42.

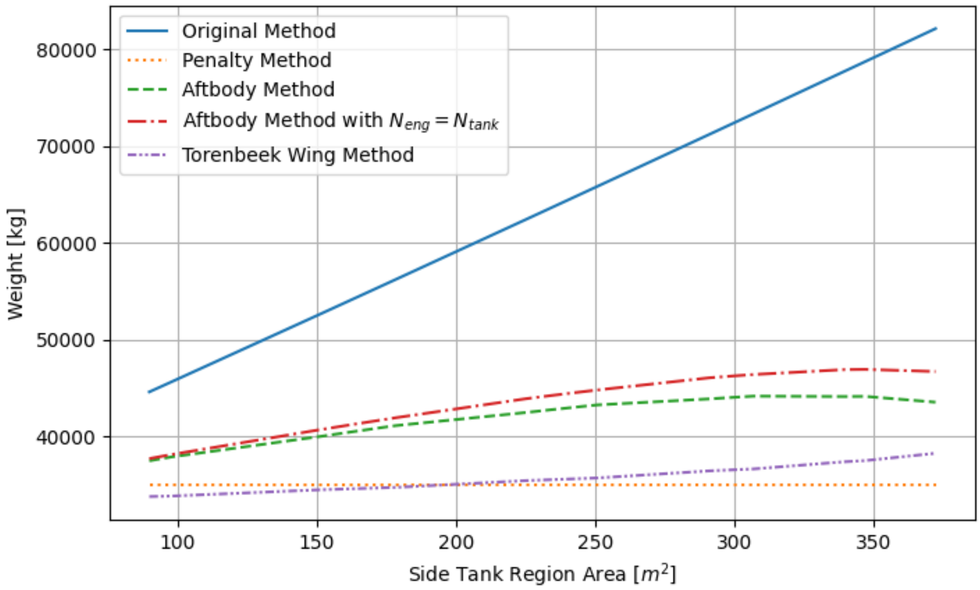

Figure 3.23: Front centerbody weight estimation using different methods, the red dotted method was selected in this study

3.7.2. Outer Wing Weight

The weight estimation of the outer wing requires special attention, as the outer wing will not contain any fuel. Due to the lower weight supported by the wing the bending moment experienced by the wing during flight will be higher. This means empirical weight estimation relations set up for conventional wings need to be adjusted. The Torenbeek wing weight estimation method given in Roskam [67] will be used to compute the unadjusted wing weight. This relation is given in Equation 3.44, where W_{ZF} is the zero fuel weight, n_{ult} is the ultimate load factor, S_w is the reference area of the outer wing and t_r is the thickness of the root airfoil section. All weights are in lbs, while all dimensions are in ft. The minimum value for the ultimate load factor from CS25 is taken, which is 2.5. A safety margin of 50 % is applied to the load factor.

$$W_w = 0.0017 W_{ZF} \left(\frac{b_{wing}}{\cos\Lambda_{c/2}}\right)^{0.75} \left[1 + \left(\frac{6.3\cos\Lambda_{c/2}}{b_{wing}}\right)^{0.5}\right] n_{ult}^{0.55} \left(\frac{b_{wing} S_w}{t_r W_{ZF} \cos\Lambda_{c/2}}\right)^{0.3} \tag{3.44}$$

Based on Roskam [67] weight penalties or benefits are applied to the computed wing weight. For spoilers and speedbrakes 2 % is added, 5 % is substracted as the landing gear are not mounted under the wing and if the engines are mounted under the outer wing another 5 % is substracted. Corrections to the wing weight are applied to account for the wing not carrying any fuel. Healy et al. [96] investigated the effect of dry wings on wing weight. The weight of a dry wing is compared to the reference wing weight for different wing spans for an A320 reference aircraft. The work found the wing weight penalty to be roughly 3.5 % at an aspect ratio of 10, observing an almost linear increase in weight penalty to 6 % for an aspect ratio of 20. Taflan et al. [97] supports those findings, finding a weight penalty of 3.4 % for a B737 reference wing with an aspect ratio of 10. Based on those findings a weight penalty of 3.5 % is applied to outer wings with an aspect ratio of 10 or lower. The generation of outer wings with an aspect ratio higher than 10 is avoided, as explained in subsection 3.3.4.

3.7.3. Center of Gravity Estimation

The center of gravity is estimated using the computed component weights and the position of the components. For the fuel tanks and engines the CG location can be easily found using the built-in CG location attribute of their geometries in the ParaPy model. For the centerbody the CG is assumed to be at the CG location of the passenger cabin. The CG of the side tank region is placed at the area weighted centroid when viewing the planform from the top. Viewed from the side the aft body has a triangular shape, meaning the CG location of this component is assumed to be at 1/3 of its length. The CG location of the outer wing is estimated based on typical locations given in Roskam [67]. For the other systems typical CG locations given in Roskam [67] and Kays [62] are used.

No longitudinal stability analysis is applied to place the landing gear. Instead, the nose gear is assumed to be placed at 10 % of the center section chord, after which the CG location without the main landing gear is computed. The main landing gear is then placed 5 % of the center chord behind this CG location. After this the overall CG location is computed. Note that the landing gear locations are based on recommendations given in Roskam [98] and landing gear locations of BWB designs from literature, such as from Liebeck [10]. The volume required by the landing gear has to be taken into account. This is done by reserving the front and rear 20 % of the cabin (with respect to the cabin length) for the landing gear. This affects the total available volume for cargo. The cargo volume can be checked in the design tool and if not enough volume is available for cargo the cabin height can be increased by the user.

3.8. Stability Analysis

In this work the static longitudinal stability of the BWB concepts in cruise is considered. For the conceptual design phase more detailed analyses, such as dynamic or lateral stability, are not considered. With the center of gravity location determined, the next step is determining the location of the neutral point. Using these two locations the static margin of the aircraft can be determined.

The clean neutral point of the BWB concepts is computed by AVL. For the stability analysis the begin of cruise conditions are taken to determine the clean neutral point. The clean neutral point does not take the engine nacelles into account, meaning a correction is applied to account for those. The nacelle correction method from Torenbeek [66] is used. The relation to compute the neutral point shift is given below.

$$\Delta \frac{x_{np}}{\bar{c}} = \sum_{i=1}^{N_{eng}} k_n \frac{b_n^2 L_n}{C_{L_\alpha} S \bar{c}} \tag{3.45}$$

Where $\Delta x_{np}/\bar{c}$ is the total nondimensional shift in neutral point due to the nacelles, b_n is the width of the nacelle, L_n is the distance between the nacelle and the mean aerodynamic chord, C_{L_α} is the lift slope of the clean aircraft and $\bar{c}$ is the mean aerodynamic chord. The factor k_n takes the type of engine placement into account. The factor is -4 for nacelles mounted in front of the leading edge of the wing and -2.5 for engines mounted to the sides of the rear fuselage. For BWB concepts with engines mounted on the aft body it is assumed the same factor as for rear fuselage mounted engines can be used.

As the correction requires the distance between nacelles and the mean aerodynamic chord and the mean aerodynamic chord length, the mean aerodynamic chord has to be determined. This is done based on the planform of the BWB concept. Since the aircraft planform is defined by airfoil sections at different spanwise positions, the planform is a composition of trapezoidal wing elements. The mean aerodynamic chord of each trapezoidal wing element can be determined using Equation 3.46 and Equation 3.47 for the mean aerodynamic chord length and y coordinate of the leading edge, respectively [99]. The x coordinate of the leading edge is determined using the leading edge sweep angle of the trapezoidal element and the spanwise position of the mean aerodynamic chord. The full aircraft mean aerodynamic chord is found using an area weighted average of the individual element lengths and coordinates. In the equations $\bar{c}_i$ is the mean aerodynamic chord of a trapezoidal element, λ_i is the taper ratio of an element, $C_{r,i}$ is the root chord of an element, $y_{r,i}$ is the y coordinate of the leading edge of an element and b_i is the span of an element.

$$\bar{c}_i = \frac{2}{3} c_{r,i} \left(\frac{1 + \lambda_i + \lambda_i^2}{1 + \lambda_i} \right) \tag{3.46}$$

$$\bar{y}_i = y_{r,i} + \frac{b_i}{2} \cdot \frac{1 + 2 \cdot \lambda_i}{3 + 3 \cdot \lambda_i} \tag{3.47}$$

3.9. Concept Optimisation

After sizing the baseline BWB concept, the design inputs of the concept are not optimal yet. To draw meaningful conclusions regarding the best performing concept, it is important to optimise the concepts for minimum fuel burn. Besides this, the baseline concepts are not guaranteed to be statically stable (positive static margin). The planform of the BWB concepts will be optimised for maximum range, after which the Class 1 – Class 2 iterations are repeated to find a reduced fuel mass for the design range. This will be done for two TLR points. The baseline optimisation will be performed for a 350 pax, 10 000 km range BWB. After this a second optimisation will be performed for a 250 pax, 7000 km range BWB.

3.9.1. Planform Optimisation 350 Passengers

As explained earlier, there are 3 options for the exit design of the passenger cabin. For each exit design the cabin can have different numbers of bays. This means a large number of baseline concepts can be generated, with each requiring an optimisation. Since the available computational time is limited, some concessions are made. First, the number of design variables has to be limited. Based on the outcomes of the sensitivity analysis presented in section 5.1 design variables with a small effect on the aircraft performance are omitted. The variables that are included are the cabin sweep angle, outer wing sweep angle, side fuel ratio and the airfoil section twist angles. Although the sensitivity of the wing thickness is only slightly smaller than that of the outer wing sweep, the large effect of the outer wing sweep on the static margin is the deciding factor for including the outer wing sweep in the design variables and excluding the wing thickness. In the model 10 airfoil sections define the BWB geometry (excluding the winglet tip section). The three center airfoil sections defining the cockpit nose shape will have a constant twist angle between those sections to avoid large jumps in leading edge and trailing edge shape. This caused unrealistic jumps in the lift distributions computed by AVL. This means one twist angle variable will define the twist angle of those 3 sections. A total of 8 twist angles therefore define the twist distribution of the concepts. The twist angles indices are visualised in Figure 3.24.

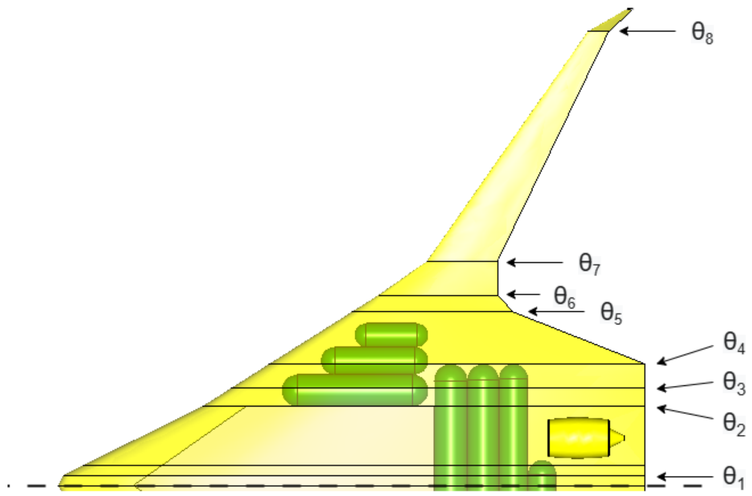

Figure 3.24: Diagram showing twist angle indices

The design variables are written to vector form. The design vector used for the planform optimisations is given in Equation 3.48. A total of 11 design variables are included in the optimisation. Note that Λ_{cab} is the leading edge sweep angle of the cabin, Λ_w is the leading edge sweep angle of the outer wing and ϕ_f is the side fuel ratio (fuel volume next to the cabin as a ratio of the total fuel volume). After performing the Class 1 – Class 2 iterations for the baseline concept a certain fuel mass is found for the required design range. To avoid repeating the Class 1 – Class 2 iterations for every function evaluation in the optimisation, the achievable range with the earlier determined fuel mass is maximised. A minimum static margin is imposed as a constraint. The formal objective function is given in Equation 3.49. The minimum static margin is set at 5 %, which results in the constraint function given in Equation 3.50. A value of 5 % is chosen as the aerodynamic model overestimates the static margin, which will be explained in more detail in section 4.2.

$$\mathbf{x} = \left[\Lambda_{cab}, \Lambda_w, \phi_f, \theta_{1-8}\right] \tag{3.48}$$

$$f(\mathbf{x}) = -\frac{R}{R_{des}} \quad (3.49) \qquad g(\mathbf{x}) = SM - 5 \quad (3.50)$$

The optimisation algorithm used is the COBYLA algorithm included in the SciPy package, available in Python. This is a 0th order method, requiring only the function values. As the model is non-linear, not fully continuous and expensive to run, gradient information will not be reliable and expensive to obtain. A test run was performed with a gradient based algorithm with limited design variables. This test run did not converge to an optimum. The algorithm makes a linear approximation of the design space around the starting point and finds the optimum of this approximation. It then repeats the process from this new point until a certain step size tolerance is met. The algorithm minimises the objective value, hence the negative objective function. The COBYLA algorithm is sensitive to scaling as the initial step size and final tolerance of the design variables are one set value. This means all design variables should have the same scale. The lower and upper bounds for the scaled design variables are set at 0.8 and 1.2. The unscaled bounds are given in Table 3.8, as well as the initial values of the design variables. The upper limit for the cabin sweep angle of 66° is based on the limit used in Karpuk et al. [17]. Note that the initial value of the side fuel ratio ϕ_f and its bounds differ per cabin design, based on a feasible range determined before the optimisations. The twist angle bounds are based on a +/- 2° change in angle with respect to the baseline twist distribution. It must be stressed that the concepts are optimised for cruise conditions only. The performance of the concepts at low speed conditions is not considered, both due to limiting the scope of this work and limitations of the aerodynamic analysis model (see section 4.2).

$$\begin{aligned} \text{minimise} \quad & f(\mathbf{x}) \\ \text{s.t.} \quad & g(\mathbf{x}) \geq 0 \end{aligned}$$

Table 3.8: Design variable bounds for the planform optimisations

Parameter	Initial Value	Lower Bound	Upper Bound
Λ_{cab} [deg]	55	44	66
Λ_w [deg]	35	28	42
θ_1 [deg]	-2	-4	0
θ_2 [deg]	-1	-3	1
θ_3 [deg]	-0.5	-2.5	1.5
θ_4 [deg]	-0.25	-2.25	1.75
θ_5 [deg]	0.25	-1.75	2.25
θ_6 [deg]	0.5	-1.5	2.5
θ_7 [deg]	1	-1	3
θ_8 [deg]	-2	-4	0

As mentioned, the initial side fuel ratio and the bounds depend on the cabin design. Cabins with a low number of bays (long, narrow cabins) have more room next to the cabin, with limited width behind the cabin for tanks. The opposite is true for cabins with more bays (short, wide cabins). Before running the optimisations feasible ranges for the side fuel ratio were evaluated for the different cabin designs. To add to this, the cabin can have three exit design options. For the baseline TLRs considered, which are given below in Table 3.9, exit design option 3 results in only one feasible cabin design to satisfy the sidewall length constraint, a cabin with 7 bays. Exit design options 1 and 2 result in a longer cabin or less room for fuel tanks. This means for a cabin with 7 bays only exit design option 3 is considered, as this results in the smallest cabin with the most room for tanks. It is expected the other two exit designs would result in increased cabin weight due to the additional doors and resulting cabin length. The number of bays considered range from 2 – 6, while there are 2 exit design options per cabin. Each concept also has the option of having wing mounted or aft mounted engines. This means a total of 11 cabin designs are possible which have 2 engine options. A total of 22 concepts will therefore be optimised. In Table 3.10 the variants and their cabin designs are listed. The initial side fuel ratios are also included. Note that for each variant two engine options are considered. The variants will therefore be referred to as variant 1-Wing, 1-Aft, etc.

Table 3.9: TLRs of the BWB concepts for the baseline planform optimisations

Parameter	**Value**	**Unit**
Passengers	350	-
Cruise Altitude	35 000	ft
Design Cruise Range	10 000	km
Cruise Mach Number	0.8	-
Airplane Class	VI	-
Wing Span	80	m

Table 3.10: BWB baseline cabin designs for optimisation

Variant	n_{bays} **[-]**	**Cabin Option**	$\phi_{f,0}$ **[-]**	$\phi_{f,l}$ **[-]**	$\phi_{f,u}$ **[-]**
1	2	1 - Additional LE Doors	1	0.5	1
2	3	1 - Additional LE Doors	0.6	0.5	0.7
3	4	1 - Additional LE Doors	0.45	0.2	0.7
4	5	1 - Additional LE Doors	0.25	0	0.5
5	6	1 - Additional LE Doors	0.1	0	0.5
6	2	2 - Ventral Exits	1	0.5	1
7	3	2 - Ventral Exits	0.6	0.5	0.7
8	4	2 - Ventral Exits	0.3	0.2	0.7
9	5	2 - Ventral Exits	0.15	0	0.5
10	6	2 - Ventral Exits	0.1	0	0.5
11	7	3 - Max Sidewall Length	0	0	0.5

3.9.2. Planform Optimisation 250 Passengers

A second planform optimisation of different BWB concepts is performed for a different TLR point, compared to the baseline. The optimisation procedure is the same as the baseline optimisation, however the TLRs are changed and the baseline concepts are different. The TLRs are given in Table 3.11.

Table 3.11: TLRs of the BWB concepts for the second planform optimisations

Parameter	**Value**	**Unit**
Passengers	250	-
Cruise Altitude	35 000	ft
Design Range	7000	km
Cruise Mach Number	0.8	-
Airplane Class	V	-
Wing Span	65	m

Since the cabin size and required fuel will be different due to the TLR changes, the feasible baseline concepts have to be reconsidered. It is found a 7 bay cabin is not feasible, while two cabins are feasible for exit option 3. As in the first optimisation no direct comparison was made between exit option 3 and the other two options (with the same number of bays) this will be performed in this optimisation for a cabin with 5 bays. For a cabin with 6 bays only exit option 3 is considered. The baseline variants are given in Table 3.12. The other planform parameters have the same initial values and bounds as in the baseline optimisation (Table 3.8).

Table 3.12: BWB baseline cabin designs for the optimisation with TLR changes

Variant	n_{bays} [-]	Cabin Option	$\phi_{f,0}$ [-]	$\phi_{f,l}$ [-]	$\phi_{f,u}$ [-]
A	2	1 - Additional LE Doors	1	0.5	1
B	3	1 - Additional LE Doors	0.45	0.2	0.7
C	4	1 - Additional LE Doors	0.3	0	0.5
D	5	1 - Additional LE Doors	0.1	0	0.5
E	2	2 - Ventral Exits	1	0.5	1
F	3	2 - Ventral Exits	0.45	0.2	0.7
G	4	2 - Ventral Exits	0.3	0	0.5
H	5	2 - Ventral Exits	0.1	0	0.5
K	5	3 - Max Sidewall Length	0	0	0.5
L	6	3 - Max Sidewall Length	0	0	0.5

3.9.3. Cruise Conditions Optimisation

After optimising the planform of the BWB concepts, the cruise conditions of the concepts are optimised. This is to check if the cruise conditions will have a significant effect on what the optimal concept will be. This optimisation is a simpler one, as it only includes two design variables, the cruise altitude and the cruise Mach number. Just like in the planform optimisation the range will be maximised for a constant fuel mass. After this the Class 1 – Class 2 iterations will be performed again to find the new fuel mass for the design range.

The static margin will not be considered in this optimisation, meaning it is an unconstrained optimisation. This is done to reduce computational time. After optimising the cruise conditions the stability is checked manually. The bounds and initial values are given in Table 3.13, note that the maximum Mach number is 0.84. As will be explained later in section 4.2 the aerodynamic model loses its accuracy past higher Mach numbers (0.85+) meaning a bound is imposed on the optimisation. To stay on the conservative side the bound is set at 0.84.

The design space was found to be continuous and smooth. This and the reduced number of design variables resulted in the choice to use the SLSQP algorithm provided by SciPy. This is a gradient based method which approximates the objective function around the starting point of an iteration using gradient information. For smooth and continuous functions this method shows faster convergence than the COBYLA algorithm. This was tested before performing the optimisations for the full concept batches.

It is important to stress that there are limitations of the model with respect to the cruise altitude as well. First of all, pressurisation of the cabin is not considered, meaning effects of a larger or lower pressure difference between the cabin and the ambient air are not captured. A constant TSFC value is used in the model, meaning altitude and velocity effects on the engine efficiency are not considered. Finally, the cruise altitude will affect the time to climb. Effects of a longer or shorter time to climb are also not included in the model.

Table 3.13: Design variable bounds for the cruise conditions optimisations

Parameter	Initial Value	Lower Bound	Upper Bound
Cruise Altitude [ft]	35000	30000	48000
Cruise Mach [-]	0.8	0.76	0.84

3.10. Summary of Assumptions

Because of the unconventional nature of BWB concepts and this work being at a conceptual level, a number of assumptions have been made in the creation of the design tool. It is important to highlight assumptions that are made. The assumptions are also explained in the relevant sections, however here they are summarised for clarity:

- Evacuation times for the different cabin exit options are assumed to meet certification requirements.

- The low speed aerodynamic characteristics of the BWB concepts are not considered in this work. Concepts are optimised for their cruise performance only.
- Only the static longitudinal stability of the concepts is considered. This means the vertical tail sizing is omitted in this work and the concept is symmetric in z-direction, with no dihedral angle applied to the outer wing.
- Additional profile drag due to lift, interference drag and trim drag are ignored.
- The parasite drag is added as a constant percentage of the total profile drag.
- The centerbody wave drag is ignored, meaning the wave drag is only computed for the transition region and outer wing of the BWB concepts.
- For the engines a constant TSFC is assumed, based on the same SEC as state of the art turbofan engines. This means the TSFC is scaled based on the LHV of the fuels. Altitude and velocity effects on the TSFC are not considered.
- Effects of the cabin pressurisation on the cabin structural weight are not considered.
- Effects on the fuel mass due to the time to climb and descent for different cruise altitudes are not considered. For all cruise altitudes the same fuel fractions for those mission phases are used.
- The hydrogen tanks are assumed to be cylindrical, non-integral tanks with spherical end caps. The mass of the mounting structure is added as a constant percentage of the tank mass.
- The hydrogen tank insulation layer is sized based on a required boil-off rate for a dormancy time of 12 hours at sea level conditions at an ambient temperature of 288.15 K. Effects of hot conditions on the dormancy time and required boil-off rate are not considered. Pressure and hydrogen phase evolutions in the tank and their effects on the boil-off rate are not considered.
- The hydrogen tank structural layer is sized based on the largest pressure difference loads experienced by the tank, including fatigue cycles. Other loads are not considered.
- The nose gear is placed at 10 % of the center section chord, with respect to the nose of the aircraft. The main landing gear is placed 5 % behind the center of gravity (excluding the landing gear) of the aircraft.
- For the landing gear 20 % of the cabin length is kept free at the front of the cabin and 20 % of the cabin length at the rear. The volume that is kept free is subtracted from the available cargo hold volume (so no effect on the passenger cabin volume).
- The cabin leading edge sweep angle variable also determines the leading edge sweep angle of the side tank region and transition region of the BWB concepts.

4
Verification & Validation

In this chapter the conceptual design model and the applied methods will be verified and validated where possible, to check if the outputs of the model are reliable and correct. In section 4.1 correct implementation of model elements will be verified, after which the outputs of the analysis models and methods will be validated using reference data from other work in section 4.2.

4.1. Verification

Verification of the implemented models is important to obtain confidence in the created conceptual design tool. Due to the combination of several different methods to create the design tool it is not possible to verify every applied model. Consistency of the created BWB geometries and correct fitting of the hydrogen tanks are verified visually, the Class 2 weight estimation methods are checked by hand, the AVL inputs are verified and the induced drag computed by AVL is checked using the standard induced drag equation. Furthermore, the computations of the neutral point and static margin are verified, the consistency of the Class 1 – Class 2 iterations is checked and the accuracy of the estimated maximum L/D is verified. For verification of the design tool an example BWB is generated. The specifications of this concept are given in Table 4.1.

Table 4.1: Specifications of the example BWB used for verification of the design tool

Parameter	**Value**
Passengers [-]	350
Cruise Altitude [ft]	35 000
Design Range [km]	10 000
Cruise Mach Number [-]	0.8
OEM [kg]	191 000
MTOM [kg]	260 000
n_{bays} [-]	4
ϕ_f [-]	0.4
Λ_{cab} [deg]	55
Λ_w [deg]	35
$(t/c)_w$ [-]	0.08
b [m]	80

The created BWB geometries are verified visually, by inspecting whether airfoil fits are correct without any internal components clipping through the outer aircraft surface. Sweep angles are inspected for consistency across trapezoidal wing elements, as well as the straight trailing edge. The tank fitting algorithm is verified by visualising the trapezoid in which the circles (tank cross-section) are fitted. This is shown in Figure 4.1, where it can be seen the circles are correctly fitted in the trapezoid formed by the cabin side wall and the outboard tank region wall.

The correct functioning of the tank fitting algorithm is also verified using the required and available fuel volumes. Evaluation of several different variants resulted in the available fuel volume satisfying the required fuel volume with a maximum tolerance of around 1 %.

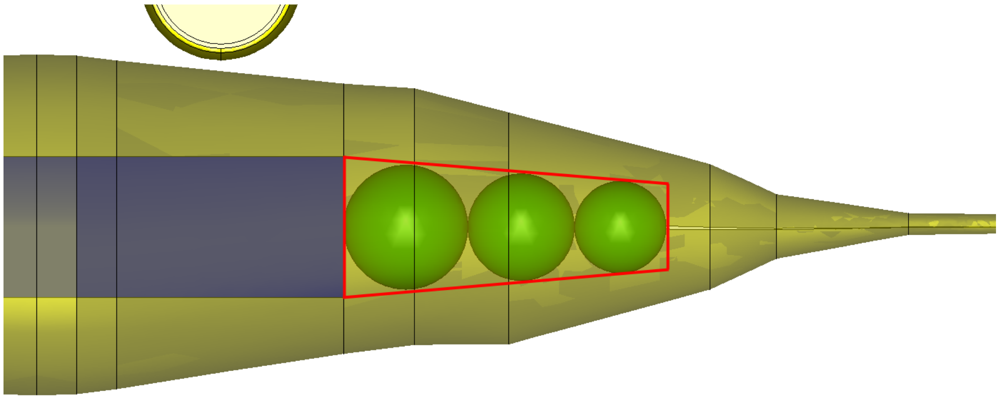

Figure 4.1: Front view of side tank region for verification of the tank fitting algorithm

For the weight of the pressurised cabin the computed weights by the model were compared to results from hand calculations to verify the correct implementation of the weight equation. Similar verifications are performed for the Class 2 weight methods from Roskam [67].

For the AVL analysis the AVL geometry that is generated by ParaPy is verified. In Figure 4.2 the ParaPy geometry of a BWB concept is given and in Figure 4.3 the resulting AVL geometry is shown. As can be seen the geometries are consistent. The AVL input files are also checked manually for consistency in the airfoil section leading edge positions, airfoil coordinates and twist angles.

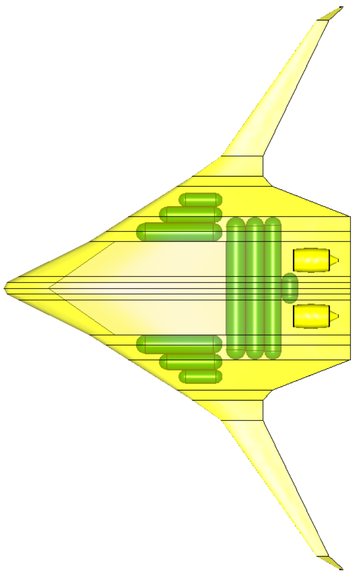

Figure 4.2: Example BWB geometry generated in ParaPy

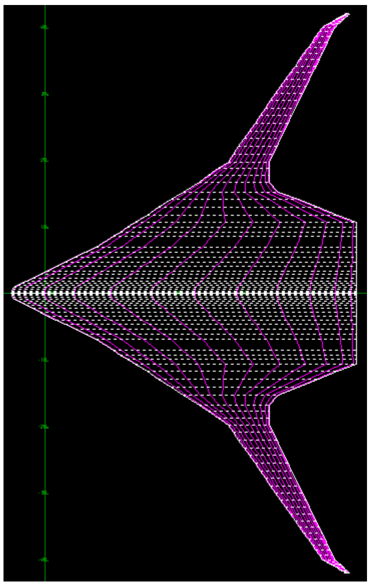

Figure 4.3: Example BWB geometry generated in AVL

Similarly to the verification performed in Brown [58], the induced drag results from AVL are verified using the theoretical induced drag, which is computed using Equation 4.1 where e is the span efficiency factor. In Figure 4.4 the induced drag from AVL and theoretical induced drag for a sweep of lift coefficients and for span efficiency factors of 0.7, 0.8 and 0.9 are shown. The BWB variant used to compute the induced drag has a span efficiency factor of 0.8 at a lift coefficient of 0.2 and an aspect ratio of 4.64. At a lift coefficient of 0.6 the span efficiency factor is 0.86. Note that the aspect ratio used for the theoretical induced drag is set equal to that of the BWB concept.

$$C_{D_i} = \frac{C_L^2}{\pi A e} \tag{4.1}$$

From the computed drag values it is clear AVL provides an accurate estimate of the induced drag of the aircraft. For positive lift coefficients higher than 0.1, the induced drag computed by AVL falls in between the theoretical induced drag lines for a span efficiency factor of 0.8 and 0.9. This is also the range of span efficiency factors computed for the example BWB, meaning it is expected that the AVL induced drag falls in between those two theoretical induced drag values. At low and negative lift coefficients the computed induced drag is higher than expected. This phenomenon is also observed by Brown [58]. At a lift coefficient of 0 the induced drag is nonzero, which is not what is expected theoretically. Due to discretisation errors and nonzero local lift coefficients some downwash is still present in the Trefftz plane, which results in a nonzero induced drag. As the aerodynamic analysis is run for lift coefficients between 0.1 and 0.3, the induced drag computed by AVL and used to generate results for this work is deemed sufficient.

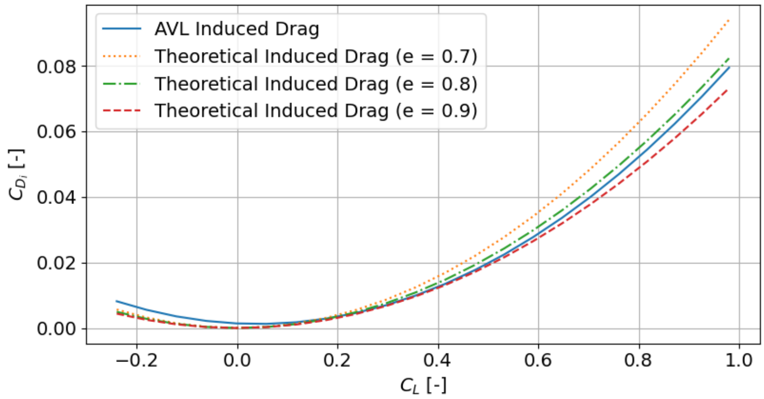

Figure 4.4: Verification of induced drag computed by AVL

AVL is also used to estimate the location of the neutral point of the BWB concepts. The pitching moment around the neutral point should be constant for different angles of attack. To verify the correct estimation of the neutral point, the pitching moment around the neutral point is computed for a sweep of angles of attack. The moment around the center of gravity is also computed. Both pitching moments are plotted, which is shown in Figure 4.5. Note that the neutral point used in this verification is the clean neutral point, as the AVL analysis does not include effects of the nacelles. As observed in the plot, the value of the pitching moment around the neutral point does not change for different angles of attack. This means AVL correctly computes the neutral point position. The pitching moment around the center of gravity has a negative slope, which is also expected. The concept used for these calculations is different from the example BWB used for the other parts and has a positive static margin of 3.60 %.

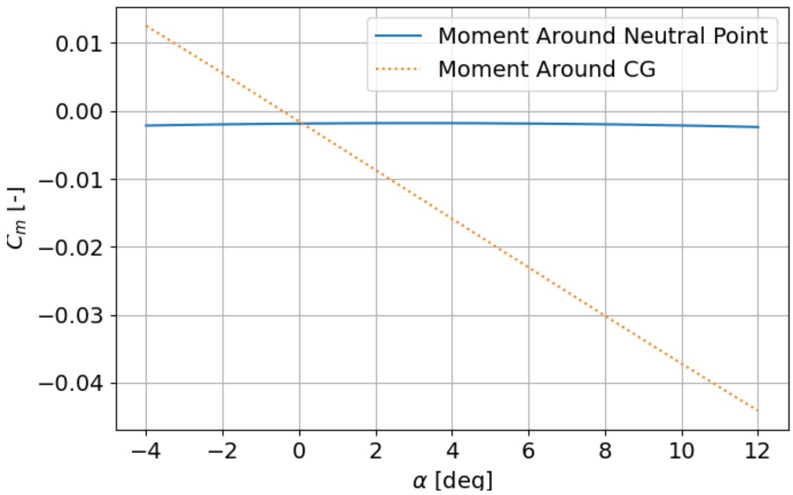

Figure 4.5: Verification of neutral point computed by AVL

The computed static margin from the aerodynamic analysis model can also be verified using the computed moment and lift slopes and Equation 4.2. For the concept used for the neutral point verification dC_m/dC_L was computed to be −0.0365, which means a static margin of 3.65 % (vs 3.60 % computed by the aerodynamic model). The static margin computed by the aerodynamic analysis model includes nacelle corrections, which causes the difference between the two values.

$$-\left(\frac{x_{np}}{\bar{c}} - \frac{x_{cg}}{\bar{c}}\right) = \frac{dC_m}{dC_L} \tag{4.2}$$

As a BWB does not have a tail, the neutral point coincides with the aerodynamic center. The aerodynamic center of a wing can be estimated by computing the aerodynamic center of the mean aerodynamic chord, which is already computed by the aerodynamic analysis model for the nacelle corrections (refer to section 3.8). This method relies purely on the planform of the wing and does not include the lift and moment distribution of the wing or Mach number effects. It can be used to verify whether the computed neutral point is at a reasonable location. For the concept used to verify the AVL analysis the x coordinate of the clean neutral point computed by AVL is 22.93 m. The x coordinate of the aerodynamic center computed using the planform method is found to be 23.96 m. As expected, different locations are found because of the reasons mentioned earlier. The error between the two methods is 4.5 %. The locations are close however, meaning the neutral point determination by AVL is considered to be done correctly.

The consistency of the Class 1 – Class 2 iterations is checked by running the iterations from different starting points. Regardless of starting point the iterations should converge to the same OEM. In Figure 4.6 the iterations are started as would be done regularly, from the first Class 1 sizing for a given concept. In Figure 4.7 the iterations are first done for another concept, after which the planform parameters are set to those of the concept used for the first convergence shown in Figure 4.6. As observed in the plots, in both cases the OEM converges to the same value, which is 174 000 kg. This means convergence is independent of the starting point and no inconsistencies are expected in the Class 1 – Class 2 iterations.

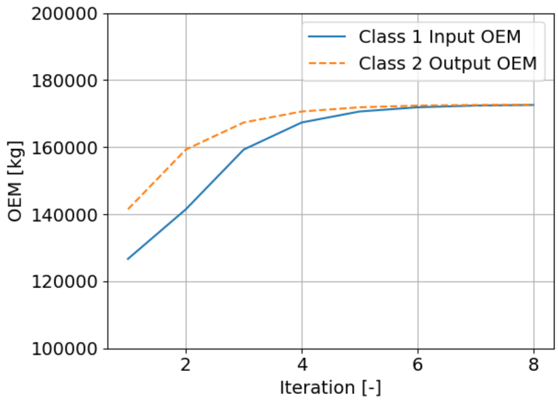

Figure 4.6: Class 1 – Class 2 iterations convergence from initial Class 1 sizing

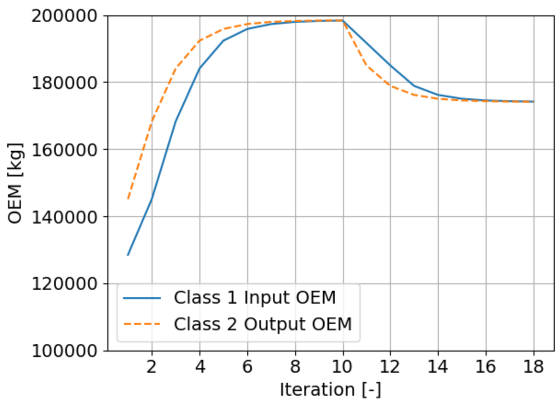

Figure 4.7: Two sequential Class 1 – Class 2 iterations: first for another BWB variant and then for the same BWB planform as in Figure 4.6

As explained in subsection 3.4.3 the optimal lift coefficient for maximum L/D is estimated. To check whether this is done accurately the L/D will be computed for a sweep of lift coefficients using AVL to find the maximum L/D and optimal lift coefficient. This is then compared to the estimated values. In Figure 4.8 the L/D computed by AVL is plotted for a sweep of lift coefficients for an example BWB concept. The estimated optimal lift coefficient using the method explained in section 3.4 and optimal lift coefficient found by AVL are marked in the plot. The estimated optimal lift coefficient is found to be 0.266, while the exact optimal lift coefficient is found to be 0.276. The absolute difference in computed lift coefficient is 3.6 %. Using the optimal lift coefficients to compute L/D with AVL, the estimated maximum L/D is found to be 23.34 and the exact maximum L/D is 23.36, which yields a difference of 0.09 %.

While the lift coefficient has a considerable error, the maximum L/D is estimated accurately. This is due to the L/D being fairly constant around the optimal lift coefficient.

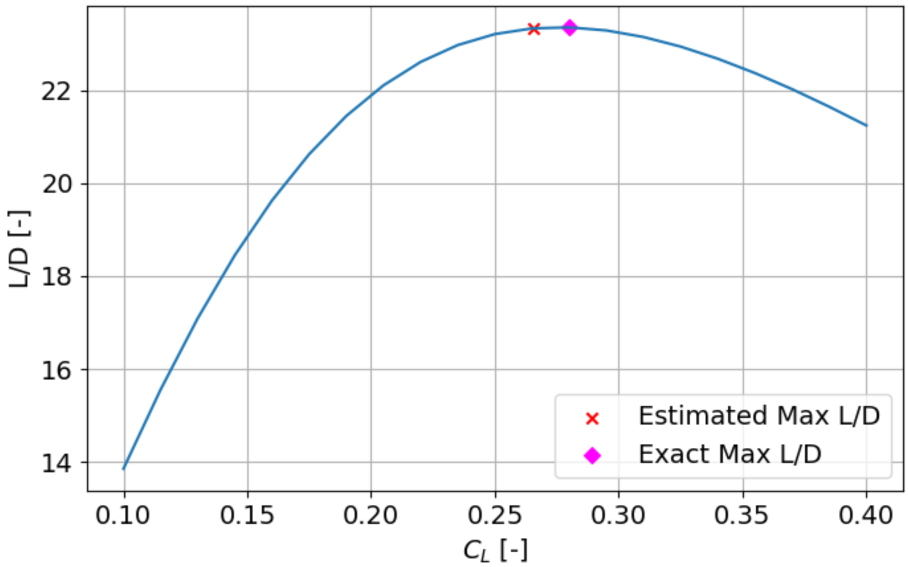

Figure 4.8: L/D versus lift coefficient for the example BWB concept for verification of estimated maximum L/D

4.2. Validation

Validation of the outputs of the model is important to check whether the model produces realistic estimates of the characteristics of the BWB concepts. The cabin sizing method is checked, the Class 2 weight estimations are validated, the high level weight groups are checked and the tank sizing method is validated. After this, a crucial part of the model is validated, which is the aerodynamic analysis method.

The cabin sizing method can be validated using the results from Bradley [68]. In this work a 365 passenger cabin is sized with 5 cabin bays. The same inputs are applied to the cabin sizing function in the design tool. In Table 4.2 the outputs from the design tool are compared to the outputs given in Bradley [68]. Note that L_{wall} is the length of the sidewall. As can be seen, there are some differences in the cabin length and width. This is due to differences in exit design between the cabins and a different bay width. In this work extra doors and aisles are placed to account for evacuation issues with BWB cabins. The cabin area shows good agreement with the results given in Bradley [68].

Table 4.2: Cabin sizing verification results

Parameter	Own Model	Bradley [68]	Difference [%]
Passengers [-]	365	365	-
n_{bays} [-]	5	5	-
Λ_{cab} [deg]	45	45	-
L_{cab} [m]	23.03	22.40	2.81
L_{wall} [m]	14.33	13.26	8.07
b_{cab} [m]	17.4	18.3	-4.92
S_{cab} [m^2]	325.1	326.28	-0.36

Extra attention has been given to the structural weight methods used in the design tool in section 3.7. Validation of the used structural weight methods is therefore necessary to obtain confidence in the used methods. The mass breakdown of the example BWB concept is computed and compared to available data for hydrogen BWB aircraft from literature. The mass breakdown data is given in Table 4.3.

Table 4.3: LH_2 BWB mass breakdown as a ratio of MTOM

Component	Example BWB	Karpuk [17]	Adler [18]	Chung [20]	Patel [22]
Centerbody	0.281	0.106	0.185	0.232	0.164
Outer wing	0.116	0.164	0.175	0.100	0.111
Total structure	0.397	0.270	0.360	0.332	0.275
Landing gear	0.041	0.039	0.054	0.015	0.039
Engines & nacelles	0.123	0.045	0.067	0.108	0.172
LH_2 Tanks	0.071	0.098	0.069	0.014	0.036
Flight controls	0.009			0.011	0.018
Hydraulics	0.01			0.012	0.015
Electrical	0.008			0.016	0.018
Avionics	0.012			0.022	0.017
De-ice	0.01			0.001	0.001
Oxygen	0.002				0.013
APU	0.008				0
Containers	0.004			0.011	0.007
Fuel system	0.011			0.054	
Furnishing	0.027			0.074	0.050
Others				0.022	0.034
Systems & items	0.101	0.172	0.099	0.223	0.173
OEM	0.734	0.625	0.650	0.700	0.695
Payload	0.135	0.268	0.247	0.231	0.210
Fuel	0.131	0.107	0.103	0.069	0.053
MTOM [kg]	260 000	261 000	213 000	260 000	54 000

As observed in the table, there are some discrepancies in weight fractions between the different designs from literature. As weight estimation methods for BWB aircraft are unproven and the designs from literature incorporate different novel technologies and propulsion systems, it is expected that the weight fractions show discrepancies. The weight fractions found in this work are in the same orders of magnitude as those found in literature.

The centerbody weight is taking up a larger portion of the total aircraft weight compared to the designs from literature. The large difference compared to the design from Karpuk et al. [17] can be explained by structural weight reductions applied in that work, through new materials and load alleviation technologies. The total structure weight fraction is quite close to the one found in Adler and Martins [18], however the individual fractions are different. This could be an accounting difference, as the transition region weight is included in the centerbody weight group in this work and might be included in the outer wing group in Adler and Martins [18] (this is not specified). The structural weight fractions are quite close to those from Chung et al. [20].

The fuel tank group also shows some differences, which can be explained by different assumed or calculated tank gravimetric efficiencies. Chung et al. [20] and Patel et al. [22] use different propulsion technologies, which could explain the differences in the engine and nacelle weight group. Considering the higher level weight groups, such as total structure, systems & items, OEM, payload and fuel the different designs show good agreement. The payload fraction found in this work is considerably lower. This can be explained by the payload in this work being only the passengers and their luggage, while in the designs from literature additional cargo weight is added. Since this work aims to compare different BWB variants for the same payload and range, this does not present an issue.

The tank sizing model used in the design tool plays an important part in collecting meaningful data. Validation of the model is therefore crucial to obtain confidence in the results. As explained in section 3.5 the insulation layer of the tank is sized based on a certain boil-off rate when standing on the platform. When using the boil-off rate (normalised for tank volume) given in Tarbah [74] the resulting insulation layer thicknesses and gravimetric efficiencies do not agree with those found in literature well. The input boil-off rate is therefore tuned using data given in Huete and Pilidis [39]. In that work several different tank designs are sized for a certain dormancy time, yielding the gravimetric efficiency of the tank. The outputs of the tank sizing model in this work are compared to those from Huete and Pilidis [39] and the boil-off rate is tuned to fit the gravimetric efficiency as closely as possible for a tank with a dormancy time of 12 hours. In Figure 4.9 the final fit is shown. The data shown is for a 100 m^3 cylindrical foam insulated tank, with an aluminium structural shell. The tank is designed for a dormancy time of 12 hours in Huete and Pilidis [39]. It was found the normalised boil-off rate (normalised by tank volume) had to be decreased with a factor of 6 to obtain a good fit between the computed gravimetric efficiency from this model and that from literature. It can be seen at low tank radii the tank sizing model in this work underestimates the tank gravimetric efficiency, however this is on the conservative side. The tanks generated in this work mostly have radii higher than 0.5 m, meaning the model is deemed accurate enough for its purpose.

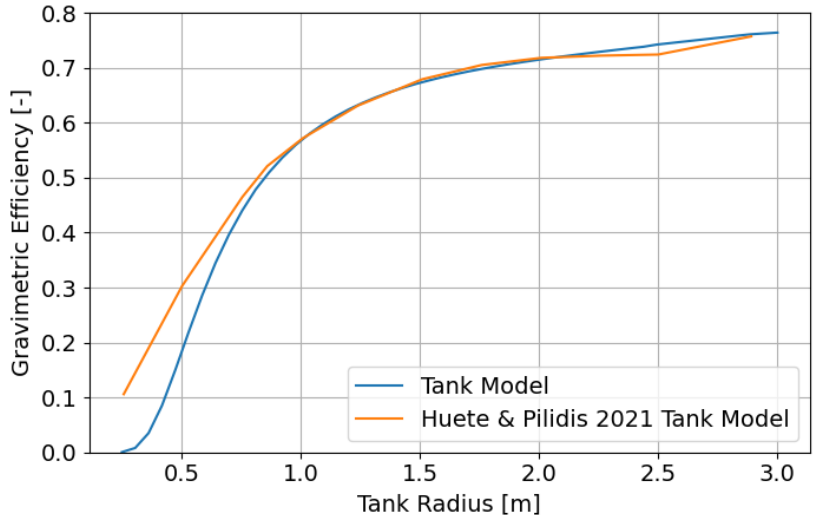

Figure 4.9: Validation of computed tank gravimetric efficiency for different tank radii with a constant tank volume of 100 m^3

The thicknesses of the tank layers and the gravimetric efficiency are further validated by comparing outputs to those given in Onorato et al. [43]. In Table 4.4 the tank inputs and computed sizing outputs are given and compared to those from literature. As can be seen, the insulation thickness is considerably higher for the tank sized using this work's sizing model. This can be explained by the difference in sizing methods, as in this model the tank is sized for a defined boil-off rate. In Onorato et al. [43] the pressure evolution in the tank is computed in a timestep based mission analysis, which is then used to determine the required insulation thickness. The differences in structural shell thickness can be explained by a different stress ratio used (as it is not clear what is used in Onorato et al. [43]) and different tank end caps. Overall the tank sizing model can be considered accurate enough for the purpose of this work, also considering the computational time of the final optimisation loop.

Table 4.4: Validation data of tank sizing model

Parameter	**Own Model**	**Onorato et al. [43]**
P_{max} [bar]	3	3
r_{tank} [m]	1.3	1.3
L_{tank} [m]	3.59	3.59
t_{in} [mm]	206	99
$t_{s,cyl}$ [mm]	2.9	2.0
$t_{s,sph}$ [mm]	1.4	2.0
m_{tank} [kg]	363	303
m_{fuel} [kg]	736	802
η_{grav} [-]	0.670	0.726

The aerodynamic analysis model is a crucial part of the design tool. Reliable and accurate estimates of the lift, drag and stability of the concepts are essential to draw useful conclusions in this work. To validate the aerodynamic model, data from literature is used. Qin et al. [11] analysed the aerodynamic characteristics of a BWB concept using high fidelity CFD analyses. The BWB geometry used is described in detail, meaning it is a useful reference to validate the aerodynamic model in this work with.

The baseline geometry used in Qin et al. [11] is replicated to validate the aerodynamic model used in the design tool. In Figure 4.10 the BWB geometries are shown.

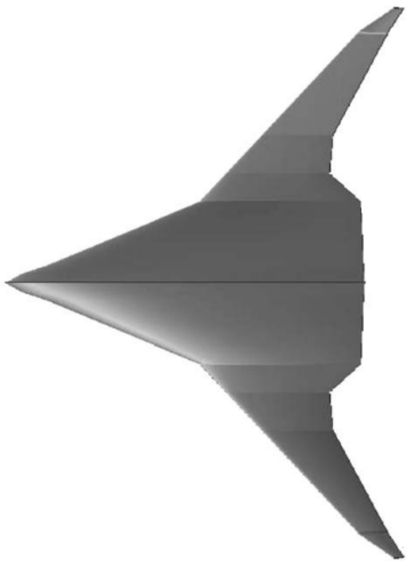

(a) Geometry from Qin et al. [11]

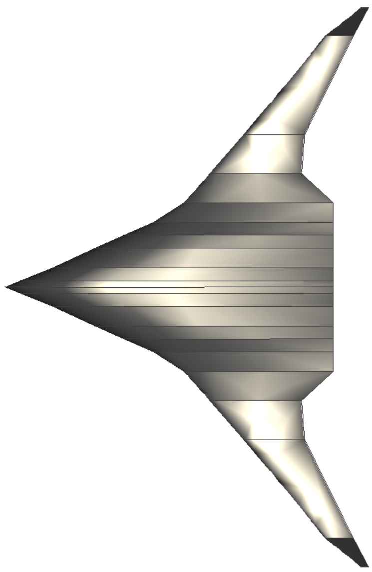

(b) Replicated geometry in ParaPy for AVL analysis

Figure 4.10: BWB geometry used for validation of aerodynamic model

The CFD results for the baseline geometry given in Qin et al. [11] are compared to the results of the aerodynamic model used in the design tool of this work, for a cruise altitude of 37 700 ft and a cruise Mach number of 0.85. In Figure 4.11 the lift and drag vs angle of attack results for the validation BWB geometry are shown, while in Figure 4.12 the drag polar is shown.

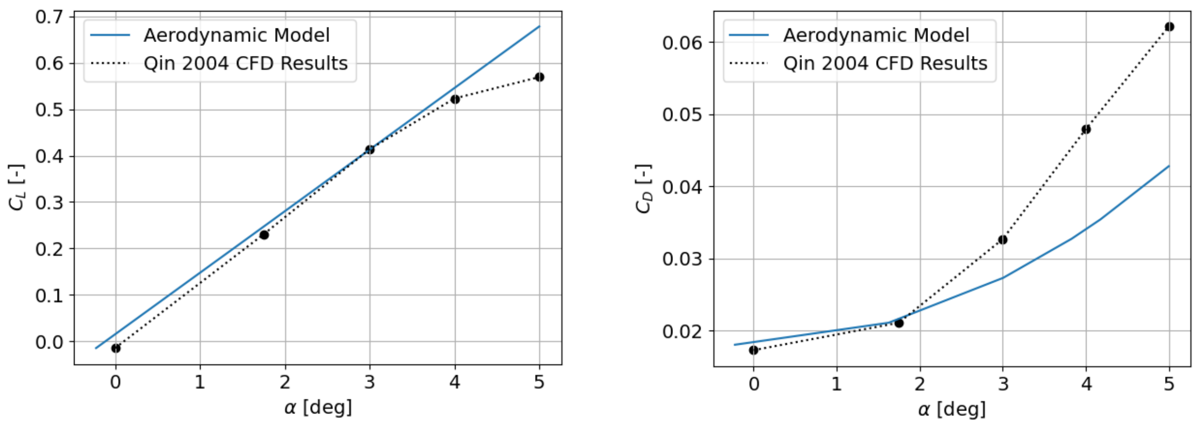

(a) Lift vs angle of attack

(b) Drag vs angle of attack

Figure 4.11: Lift and drag data for validation of aerodynamic model [11]

Considering the lift vs angle of attack results, it is clear the low fidelity aerodynamic model used in this work accurately predicts aircraft lift for an angle of attack below 4°. In the CFD data from Qin et al. [11] a change in lift slope is present from an angle of attack of 4°, due to shock induced flow separation over the outer wing [11]. The low fidelity aerodynamic model is not able to predict flow separation, as AVL only predicts inviscid forces, while the viscous and wave drag forces are estimated using empirical methods that do not take flow separation into account. As explained earlier in section 5.2 the low speed performance of the concepts is not considered. This is in part due to the inability of the aerodynamic analysis method to predict flow separation.

The drag vs angle of attack results show good agreement at low angles of attack. From an angle of attack of 3° and higher the drag is underestimated by the low fidelity model used in this work. This is caused by underestimation of the wave drag at higher angles of attack and not capturing the additional drag created by the stalled outer wings. The same can be observed in the drag polar. At low lift coefficients the low fidelity model accurately predicts the lift and drag characteristics of the BWB concept. At lift coefficients higher than 0.3 the drag is underestimated. This underestimation of the drag at higher lift coefficients by low fidelity models is observed in literature as well. Karpuk et al. [17] and Moens [59] observe the same phenomenon.

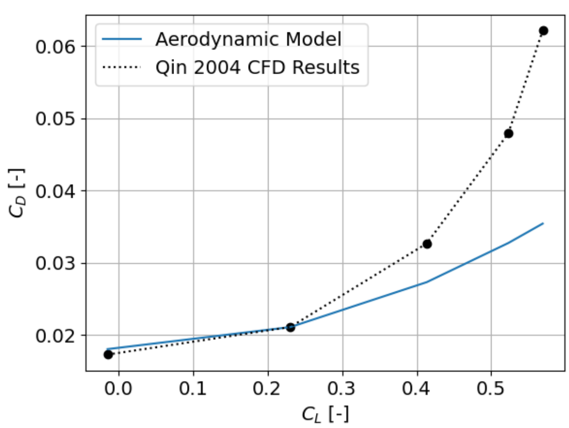

Figure 4.12: Drag polar data for validation of aerodynamic model [11]

In this work only the cruise lift and drag characteristics are required. As LH_2 BWBs require a large planform area to accommodate the hydrogen tanks, the wing loading is low. This means that the required cruise lift coefficient is low as well. Cruise lift coefficients exceeding 0.3 have not been observed in this work. Based on the lift and drag validation data and low required lift coefficients the low fidelity aerodynamic model is considered sufficiently accurate.

The individual drag components are also given in Qin et al. [11], which are used to validate the prediction of those components by the low fidelity aerodynamic model. In Table 4.5 the drag components for the lift coefficient closest to the expected cruise lift coefficient for the concepts in this work are listed. Note that the drag coefficient values are in drag counts (10^{-4}) and $C_{D_{w,i}}$ includes the wave and induced drag components. As observed in the table, the total predicted drag is very accurate, with a precision of 0.4 %. The individual drag components show larger differences. In Qin et al. [11] no separate values for the wave and induced drag are given, which means the wave drag is assumed to be included in the pressure drag component. It is therefore unclear whether the differences lie in the wave drag or induced drag. The profile drag is underestimated by the low fidelity aerodynamic model.

Table 4.5: Drag breakdown validation

Parameter	**Aerodynamic Model**	**Qin et al. [11]**	**Difference [%]**
Cruise Altitude [ft]	37 700	37 700	-
Cruise Mach [-]	0.85	0.85	-
C_L [-]	0.2305	0.2305	-
C_D [cts]	212.0	211.1	0.43
$C_{D_{w,i}}$ [cts]	122.8	132.6	-7.39
C_{D_p} [cts]	89.17	78.48	13.6
L/D [-]	10.87	10.92	-0.43

The pitching moment characteristics predicted by AVL are validated as well. In Figure 4.13 the pitching moment validation results are shown. In the CFD results from Qin et al. [11] a pitch break can be seen from an angle of attack of 3°. This is due to the shock induced flow separation over the outer wings. For the same reasons discussed earlier, the low fidelity aerodynamic model used in the design tool is not able to predict this. When looking at the linear part of the CFD results and comparing to the low fidelity results, it is clear that the low fidelity model predicts a more negative slope. As the lift slopes are similar (shown in Figure 4.11) and the static margin is proportional to dC_m/dC_L (Equation 4.2), the low fidelity aerodynamic model predicts a larger static margin for this BWB geometry than the CFD analysis performed in Qin et al. [11].

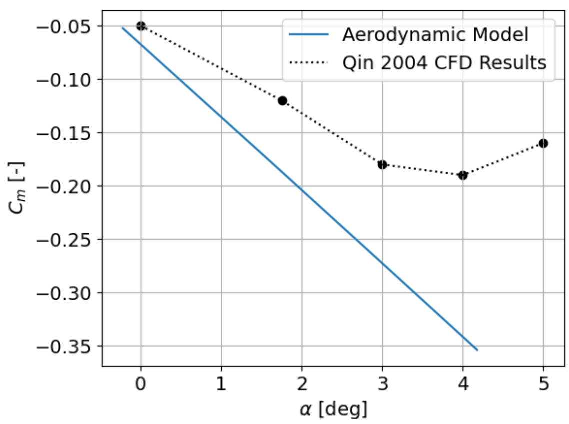

Figure 4.13: Pitching moment data for validation of aerodynamic model [11]

When considering similar validation procedures performed in literature for the pitching moment, differences in moment slope are observed as well. Karpuk et al. [17] also used AVL to predict the pitching moment of BWB concepts and compared the results to high fidelity CFD analyses. For the kerosene BWB concept considered in that work a similar moment slope was found, while for the LH_2 BWB the low fidelity model predicted a smaller static margin than the one predicted by CFD (this is shown in Figure 2.26c). Conflicting accuracies in pitching moment slope are observed between the validation performed in this work and those performed in Karpuk et al. [17], despite AVL being used in all cases. The BWB geometries used for the validations have considerable differences, meaning the differences in accuracy could be a result of different geometries. In any case, the pitching moment predicted by AVL presents a limitation of the aerodynamic model. As the purpose of this work is to compare BWB variants to each other, it is expected the fundamental differences in configuration and their effects on the aircraft level performance will not be clouded by an error in static margin prediction. For future work it is desired to perform a high fidelity analysis of the generated BWB geometries (rather than validating using one geometry from literature) to evaluate the accuracy of the AVL pitching moment more reliably.

5
Results & Discussions

In this chapter the results that are generated by the design tool are presented and discussed. In section 5.1 the results of the sensitivity analysis are presented and in section 5.2 the results of the planform optimisations for both TLR points are shown. Finally in section 5.3 the cruise conditions optimisation results are presented.

5.1. Sensitivity Analysis

Before performing the optimisation of the BWB concepts, a sensitivity analysis is performed to identify the effect of changing design parameters on the aircraft level performance metrics. The performance metrics that are considered are the OEM, fuel mass, cruise L/D and static margin. To find the sensitivities, three different BWB variants are generated and their OEMs are computed until convergence between the Class 1 and Class 2 weights. After this, the design parameters will be changed and the Class 1 – Class 2 iterations will be performed again to find the new converged point. The performance metrics at this new point will then be computed and compared to the metrics of the baseline designs.

5.1.1. Baseline Designs for Sensitivity Analysis

Three different variants are generated to evaluate whether the BWB configuration will have a significant effect on the trends observed in the sensitivity analysis. The variants considered are a BWB concept with all fuel tanks placed behind the cabin, a BWB concept with all fuel tanks placed next to the cabin and a BWB concept with a mix of both fuel tank regions. The top level requirements are given in Table 5.1 and the specifications of the concepts are given in Table 5.2.

Table 5.1: Top level requirements for the BWB concepts used for the sensitivity analysis

Parameter	**Value**
Passengers [-]	350
Cruise Altitude [ft]	35000
Design Range [km]	10000
Cruise Mach Number [-]	0.8

Table 5.2: Baseline specifications of BWB concepts used for the sensitivity analysis

Design Parameter	**Aft Fuel Variant**	**Side Fuel Variant**	**Mixed Fuel Variant**
MTOM [kg]	280 000	238 000	257 000
OEM [kg]	207 000	167 000	188 000
PM [kg]	35 300	35 300	35 300
FM [kg]	36 900	35 200	33 900
L/D_{cruise} [-]	19.9	17.0	19.9
L/D_{max} [-]	21.8	21.1	23.0
Static Margin [%MAC]	-3.8	3.2	-2.6
η_{grav} [-]	0.641	0.642	0.642
A [-]	4.21	4.98	4.70
S_{ref} [m^2]	1520	1290	1360
n_{bays} [-]	7	3	4
ϕ_f [-]	0	1	0.4
Λ_{cab} [deg]	50	50	50
Λ_w [deg]	35	35	35
λ_w [-]	0.3	0.3	0.3
$(t/c)_w$ [-]	0.08	0.08	0.08
b [m]	80	80	80

Note that the concepts are not optimised for range or stability, but have the baseline twist distribution and baseline sweep angles. This means that no conclusions can be drawn from the overall performance of these concepts yet. The shown concepts merely serve to perform the sensitivity analysis. The number of cabin bays n_{bays} is determined based on where the fuel tanks are placed to allow enough space for the tanks. All baseline variants have the engines mounted under the outer wing. The planforms of the BWB concept variants are given in Figure 5.1. The parameters that will be changed are the planform input parameters (Λ_{cab}, Λ_w, λ_w and $(t/c)_w$) and the cruise conditions. The effects of moving the engines from under the wing to the aft body will also be evaluated. The sensitivity of the metrics to the side fuel ratio ϕ_f will be evaluated for the mixed fuel concept only. The sensitivities of the metrics to the tank gravimetric efficiency and the twist angles of the airfoil sections will also be evaluated.

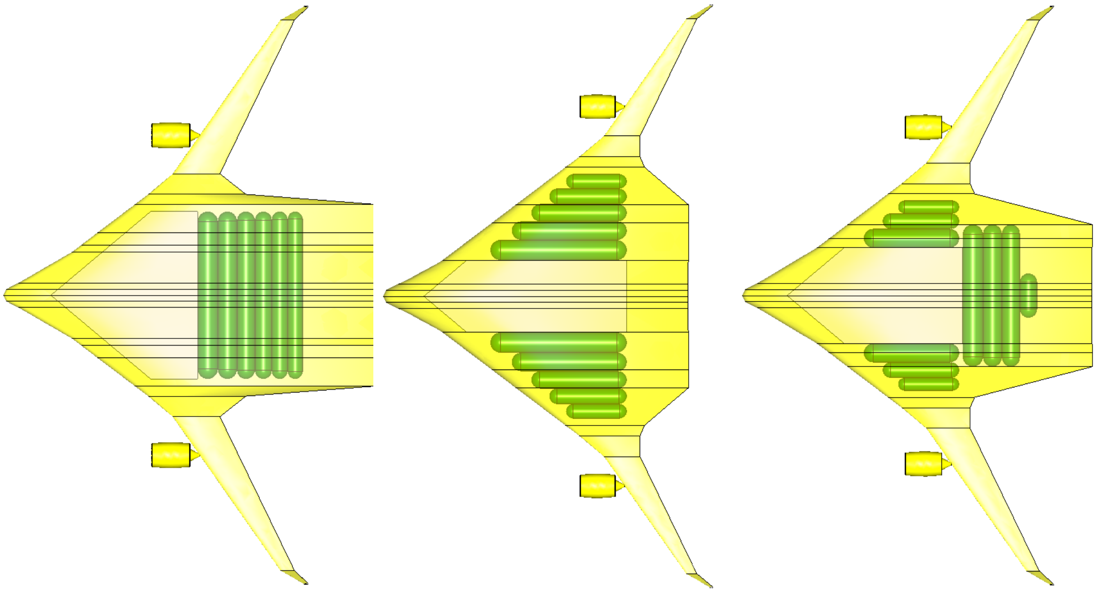

(a) Aft fuel BWB concept (b) Side fuel BWB concept (c) Mixed fuel BWB concept

Figure 5.1: Planforms of the BWB concepts used for the sensitivity analysis

5.1.2. Planform Sensitivity

Evaluation of the sensitivity of the performance metrics to the planform parameters of the BWB concepts helps identify what planform parameters have a large effect on the overall performance of a BWB concept. This provides more insight when performing planform optimisations of a BWB aircraft. In this section the planform sensitivity is evaluated for the aforementioned baseline BWB concepts. The planform parameters that are considered are the cabin sweep angle, outer wing sweep angle, outer wing taper ratio and outer wing t/c. As mentioned, for the mixed fuel concept the effect of moving more fuel volume next to the cabin will be evaluated.

Side Fuel Variant

In Figure 5.2 the planform sensitivity results for the side fuel variant are shown. Note that the + and - in front of the design variables indicate a +10 % or −10 % change of that variable with respect to the baseline values shown in Table 5.2. The percentages shown in the matrix indicate the change of that performance metric with respect to the baseline performance metric. For the static margin the change is expressed as a percentage of the mean aerodynamic chord.

Δ OEM	-6.20	4.93	0.84	-0.61	0.17	-0.14	-0.50	0.64
Δ $(L/D)_{max}$	3.75	-3.31	-0.03	-0.48	0.36	-0.26	-0.31	0.53
Δ $(L/D)_{cr}$	1.43	-1.24	0.73	-0.79	0.42	-0.35	-0.50	0.72
Δ FM	-6.34	5.20	0.03	0.12	-0.22	0.12	-0.04	-0.04
Δ SM	8.12	-6.00	-0.49	0.36	-0.07	0.07	0.11	-0.13
	+ Λ_{cab}	**- Λ_{cab}**	**+ Λ_w**	**- Λ_w**	**+ λ_w**	**- λ_w**	**+ $(t/c)_w$**	**- $(t/c)_w$**

-9%	**-6%**	**-3%**	**0%**	**+3%**	**+6%**	**+9%**

Figure 5.2: Planform sensitivity matrix for the side fuel BWB variant

As observed in Figure 5.2, the cabin sweep angle has a large effect on all the performance metrics. An increase in cabin sweep angle causes a decrease in OEM, which is caused by the side fuel tank region being more tapered. This reduces the structural weight of this region, despite the aftbody getting wider and thus heavier due to the increased centerbody span (due to the larger cabin sweep angle the side tank region span increases but becomes more tapered). The opposite effect is observed for a decrease in cabin sweep angle. For an increase in cabin sweep angle the maximum L/D ratio increases. This is caused by a decrease in profile drag. The magnitude of the maximum L/D changes are between 3 % and 4 %. Again the opposite is observed for a decrease in cabin sweep angle. The effects on the cruise L/D are a result of the changes in OEM and maximum L/D. A decrease in OEM means the cruise lift coefficient decreases, moving it away from the optimal lift coefficient for maximum L/D. In the sensitivity of the side fuel variant this is reflected by the increase in cruise L/D being a lower percentage than the increase in maximum L/D, due to the decreased OEM damping this increase through lift coefficient changes. The fuel mass effects are a result of the changes in cruise L/D and OEM. For the side fuel variant it can be seen an increase in cabin sweep angle causes a decrease in OEM and increase in cruise L/D, meaning the fuel mass decreases by roughly 6 %. The effect of the cabin sweep angle on the static margin is as expected. While an increase in cabin sweep angle will move some cabin mass more aft, the outer centerbody lifting surface and outer wing moving aft overrule the mass effects. The neutral point therefore moves aft more than the center of gravity, increasing the static margin.

For the other planform variables a much smaller sensitivity is observed. The second largest sensitivities are observed for the outer wing leading edge sweep angle. As expected, an increase in outer wing sweep angle results in an increase in OEM. The opposite is observed for a decrease in outer wing sweep angle. More interestingly, the maximum L/D is roughly equal for an increase in outer wing sweep angle, while it decreases for a decrease in sweep angle. The decrease in maximum L/D is caused by an increase in wave drag over the outer wing. Again the cruise L/D is a result of the changes in OEM and maximum L/D. In the case of the outer wing the cruise L/D follows the trend of the OEM. An increase in OEM causes an increase in cruise L/D, despite no changes in maximum L/D. For a lower outer sweep angle the maximum L/D decreases and the OEM decreases, meaning a reduction in cruise L/D is observed. Due to conflicting effects of the OEM and cruise L/D on the fuel mass the sensitivity of the fuel mass to the outer wing sweep angle is small. The static margin follows an opposite trend compared to the cabin sweep angle. In this case the change in center of gravity of the outer wing is larger than the change in neutral point of the outer wing, causing a decrease in static margin for a larger sweep angle. The opposite is observed for a decrease in outer wing sweep angle.

An increase in outer wing taper results in a larger OEM, which is expected. The opposite is observed for a decrease in outer wing taper. The maximum L/D improves for a larger taper ratio and the opposite is observed for a decrease in taper ratio. Combining the OEM and maximum L/D effects, it is seen the cruise L/D increases for an increase in taper ratio, since the OEM and maximum L/D both increase. The sensitivity of the fuel mass is low, as the the cruise L/D and OEM have conflicting effects. The sensitivity of the static margin is also small. Considering the outer wing thickness slightly larger sensitivities are observed than for the taper ratio. A thicker wing results in a lower OEM, with the opposite effect being observed for a thinner wing. The effect of the wing thickness on the maximum L/D is also as expected. The effect of the wing thickness on the cruise L/D and fuel mass then follow from those sensitivities.

Mixed Fuel Variant

In Figure 5.3 the planform sensitivity results for the side fuel variant are shown. For this variant the effect of changing the side fuel ratio is also evaluated.

Δ OEM	-1.55	1.52	1.09	-0.84	0.00	-0.20	-0.68	0.81	-5.14	0.00
Δ $(L/D)_{max}$	0.61	-1.89	-0.25	-0.38	0.16	-0.38	-0.52	-0.01	-0.01	0.83
Δ $(L/D)_{cr}$	-1.53	-0.63	0.72	-0.86	0.33	-0.46	-0.80	0.53	-2.82	1.04
Δ FM	-0.10	1.79	0.20	-0.08	-0.20	0.05	-0.08	0.06	-2.09	-0.85
Δ SM	6.23	-4.65	-0.13	0.02	-0.01	0.02	0.08	-0.08	1.99	-0.65
	$+\Lambda_{cab}$	**$-\Lambda_{cab}$**	**$+\Lambda_w$**	**$-\Lambda_w$**	**$+\lambda_w$**	**$-\lambda_w$**	**$+(t/c)_w$**	**$-(t/c)_w$**	**$+\phi_f$**	**$-\phi_f$**

-9%	**-6%**	**-3%**	**0%**	**+3%**	**+6%**	**+9%**

Figure 5.3: Planform sensitivity matrix for the mixed fuel BWB variant

For the cabin sweep angle sensitivity it is clear lower sensitivities are observed compared to the side fuel variant. As the side fuel tank region is smaller for this variant, the cabin sweep angle will have a smaller effect on the planform of the aircraft (as the cabin sweep also determines the sweep angle of the side tank and transition regions). For an increase in cabin sweep angle the OEM decreases, for the same reasons as for the side fuel variant. The opposite effect is observed for a decrease in sweep angle. Similar sensitivities as for the side fuel variant are also observed for the maximum L/D, albeit a smaller magnitude. In this case for a higher cabin sweep angle the increase in maximum L/D is caused by an improvement in span efficiency. The decrease in maximum L/D is caused by a reduction in span efficiency. The cruise L/D is lower for both an increase and decrease in cabin sweep angle. This is because the increase in aerodynamic efficiency for an increase in sweep angle is outweighed by the decrease in OEM, which results in a reduction in lift coefficient away from the optimal lift coefficient of the variant. In the case of a decreasing cabin sweep angle the decrease in aerodynamic efficiency is the deciding factor, resulting in a decrease in cruise L/D as well. For an increase in cabin sweep angle the cruise L/D and OEM changes are conflicting, resulting in a small sensitivity of the fuel mass to the cabin sweep angle. For a decrease in the cabin sweep angle this is not the case, resulting in a larger sensitivity. Similarly to the side fuel variant, the static margin shows a large sensitivity to the cabin sweep angle.

The sensitivity of the performance metrics to the side fuel ratio is considerable. For an increase in side fuel ratio the side tank region becomes larger, while the aftbody becomes smaller. For the OEM the decrease in aftbody structural mass outweighs the increase in side tank region mass. For a decrease in side fuel ratio the changes in the two mass groups roughly cancel each other out. It must be noted that for both an increase and decrease in side fuel ratio the fuel mass is lower. Since there is a snowball effect and the OEM does not change for a decrease in side fuel ratio, it can be expected the isolated OEM (without Class 1 – Class 2 iterations) of the variant would increase. For an increase in side fuel ratio the maximum L/D does not change much. For a lower side fuel ratio there is an increase in maximum L/D, caused by a slight decrease in profile drag and higher span efficiency. The cruise L/D decreases for a higher side fuel ratio due to the decrease in OEM. For a lower side fuel ratio the increase in cruise L/D is purely caused by the improved aerodynamic efficiency, as the OEM does not change. The fuel mass reduces for both an increase and decrease in side fuel ratio. As a higher side fuel ratio results in a higher fuel and structural mass next to the cabin and a lower one behind the cabin, a higher static margin is observed. The opposite happens for a decrease in side fuel ratio.

The outer wing parameters again have a smaller effect on the performance metrics. The outer wing sweep angle has the most considerable effect on the OEM, cruise L/D and fuel mass. The sensitivities are comparable to those of the side fuel variant.

Aft Fuel Variant

The planform sensitivity results for the aft fuel variant are given below in Figure 5.4.

Δ OEM	-1.23	-0.48	1.29	-0.96	0.25	-0.20	-0.50	0.69
Δ $(L/D)_{max}$	5.29	2.32	-0.42	-0.24	0.19	-0.21	-1.23	0.90
Δ $(L/D)_{cr}$	4.86	2.25	0.50	-0.70	0.32	-0.29	-1.56	1.38
Δ FM	-4.98	-2.26	0.54	-0.27	-0.13	0.08	0.74	-0.60
Δ SM	4.40	-2.98	0.03	-0.14	0.01	-0.03	-0.02	-0.01
	$+\Lambda_{cab}$	$-\Lambda_{cab}$	$+\Lambda_w$	$-\Lambda_w$	$+\lambda_w$	$-\lambda_w$	$+(t/c)_w$	$-(t/c)_w$

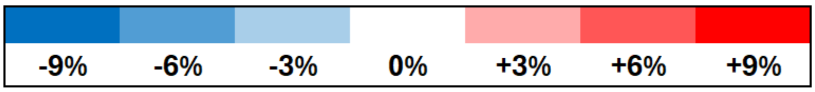

Figure 5.4: Planform sensitivity matrix for the aft fuel BWB variant

The sensitivity of the performance metrics to the cabin sweep angle is highest for this variant as well. However, the trends observed are different. The OEM has a smaller sensitivity and decreases for both an increase and decrease in cabin sweep angle. To get a better understanding of the exact source of the lower OEM sensitivity, the effect of the cabin sweep angle on the isolated structural mass is evaluated. It is found that the structural mass of the aft fuel variant barely changes for a changing cabin sweep angle. This means that the OEM changes observed are due to the snowball effect caused by L/D changes. When considering the maximum L/D changes, for an increase in cabin sweep angle the L/D changes significantly. The improvements in maximum L/D are caused by an improved span efficiency, a slight decrease in profile drag and a decrease in wave drag over the transition region of the variant (since the sweep angle of the transition region is the same as the cabin sweep angle). As discussed in section 3.4, the estimation of the wave drag over the centerbody is a limitation of the aerodynamic model. For this reason the maximum L/D sensitivity to the cabin sweep angle is also computed without the wave drag contributions of the transition region and outer wing. The reason this is not done for the other two variants is because for those variants the total wave drag (and the changes in wave drag) are negligible. For an increase in cabin sweep angle the maximum L/D (ignoring the wave drag) increases with 1.58 %, due to an improved span efficiency and slight decrease in profile drag. For a decrease in cabin sweep angle the opposite happens: the span efficiency reduces and a slight increase in profile drag is observed. The result is a change in maximum L/D of −1.32 %. Since the isolated OEM does not change considerably, it can be expected that the cruise L/D follows the maximum L/D changes, resulting in opposite trends for the cruise L/D and fuel mass for changes in the cabin sweep angle when ignoring the wave drag. When including the wave drag in the sensitivities to the cabin sweep angle, it can be seen the maximum L/D and cruise L/D improve for both an increase and decrease in cabin sweep angle, due to the decrease in wave drag. This results in a lower fuel mass for both cabin sweep angle changes.

For the aft fuel variant the outer wing planform parameters have larger effects on the performance metrics, compared to the other two variants. This can be explained by this concept having a larger outer wing compared to the centerbody (see Figure 5.1), which means changes to the outer wing have a larger impact on the total planform of the aircraft. The sensitivity of the OEM to the outer wing sweep angle is as expected, a larger sweep angle increases the OEM while the opposite is observed for a smaller sweep angle. The maximum L/D effects are more complex, as the L/D decreases for both a smaller and larger outer wing sweep angle. In the case of a larger sweep angle this is caused by a decreased span efficiency. For a smaller sweep angle the small decrease in maximum L/D is caused by an increase in wave drag over the outer wing, despite a small improvement in span efficiency. In terms of cruise L/D the OEM effects are dominating, meaning a larger sweep angle results in a larger cruise L/D due to an increase in OEM. The opposite is observed for a smaller sweep angle. The sensitivity of the performance metrics to the wing taper ratio are small, however the thickness of the outer wing has a larger effect on the metrics. The effects are as expected. The effect of the outer wing parameters on the static margin is quite small for this variant.

Engine Positioning

The effects of mounting the engines under the wing or on the aftbody are also evaluated. The performance metrics of the side fuel variant with both engine options are included in Figure 5.5. The differences stated are with respect to the variant with wing mounted engines.

The effects of moving the engines from the wings to the aftbody are similar for all three variants. The increase in OEM is caused by an increase in aftbody and outer wing structural weight. As no engines are mounted under the wing, less load alleviation is present resulting in an increase in outer wing weight. Since the engines are now mounted on the aftbody, this structure has to carry the weight of the engines, meaning the aftbody weight increases as well. The result is a considerable OEM increase for all three variants. The maximum L/D improves with aft mounted engines for all variants. This is due to the engines being placed at a more favourable distance from the aircraft surface, which means less interference drag between the nacelles and aftbody surface is estimated. The cruise L/D increases with a larger percentage, which is due to the aircraft flying at a higher and more optimal lift coefficient as a result of the increased OEM.

Combining the effects on the OEM and cruise L/D, the fuel mass increases for the mixed and aft fuel variants due to the OEM increase outweighing the L/D improvements. As the side fuel variant has a smaller OEM increase the fuel mass change is negligible. It must be noted that this work does not take boundary layer ingestion into account, which can be implemented for aft mounted engines. The effect on fuel burn of aft mounted engines could therefore change with the implementation of this technology. Another consideration for aft mounted engines is shielding of engine noise. The static margin of all variants decreases significantly, due to the center of gravity moving aft.

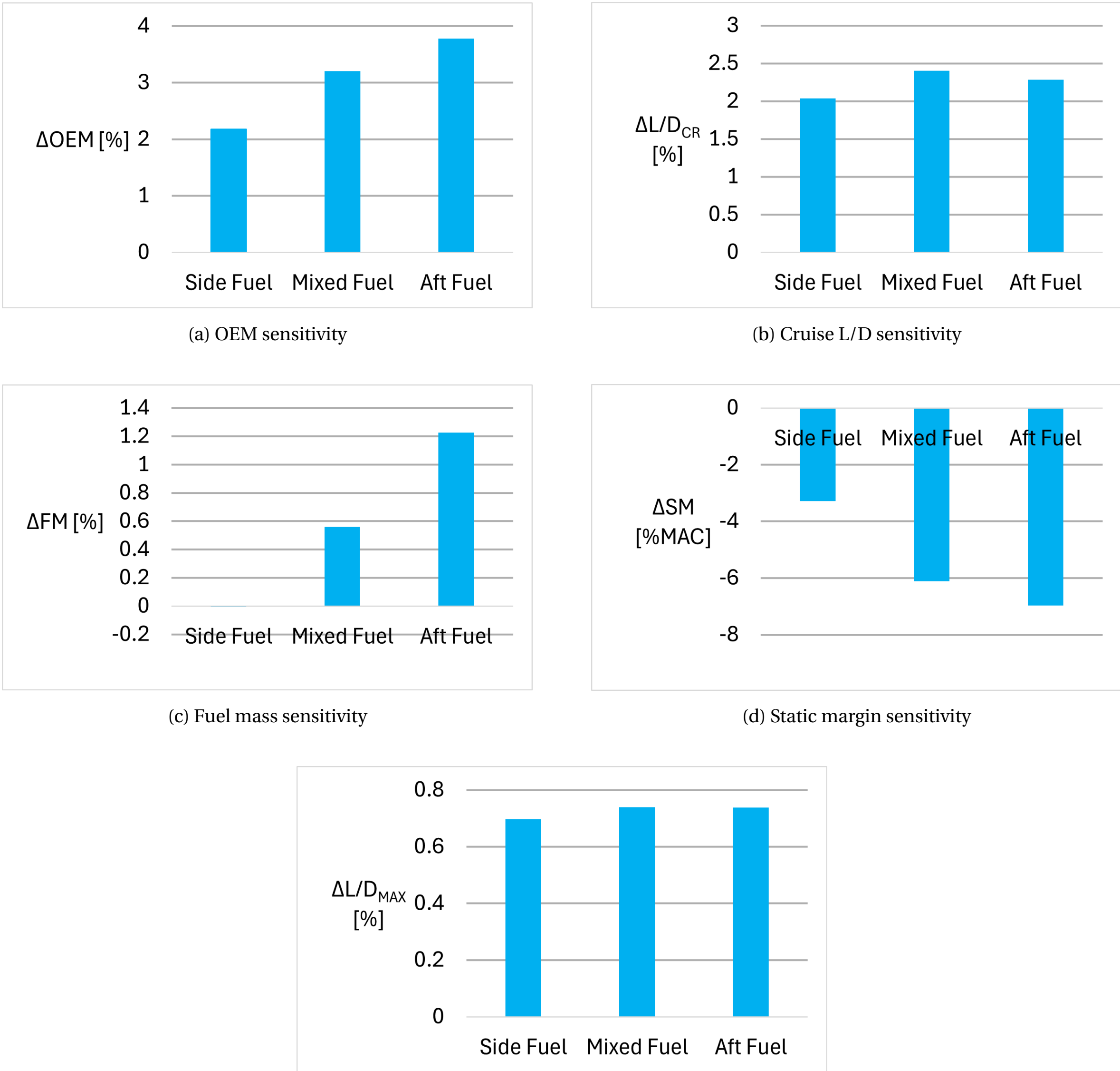

(a) OEM sensitivity

(b) Cruise L/D sensitivity

(c) Fuel mass sensitivity

(d) Static margin sensitivity

(e) Maximum L/D sensitivity

Figure 5.5: Sensitivity of performance metrics to engine position for different BWB variants. Differences indicate change from wing mounted to aft mounted engines

5.1.3. Twist Angle Sensitivity

The effects of changing the twist angles of the airfoil sections on the cruise L/D and static margin are evaluated to determine whether the twist angles are to be included in the optimisations. The twist angles have no direct effect on the weights of the aircraft, only through cruise L/D changes the weights will change when iterating between Class 1 and Class 2. In the optimisations the Class 1 – Class 2 iterations are not performed, meaning the twist angle sensitivity is computed without performing the iterations. The changes of the performance metrics are calculated for a 2° increase of each individual twist angle.

The results for the cruise L/D sensitivity to the twist angles for the BWB variants are given below in Figure 5.6. As explained earlier in section 3.3, the twist angle of the first three centerbody airfoil sections is constant across those sections. This means twist angle 1 is the twist angle of those three sections, which are the sections defining the cockpit shape. Twist angles 2 and 3 are the twist angles of the 4th and 5th centerbody airfoil sections, which still have a reflexed airfoil profile. Twist angles 4–6 are those of the airfoil sections defining the transition region, which have a symmetric airfoil profile. Twist angles 7 and 8 are those of the outer wing airfoil sections with a supercritical airfoil profile.

When considering the effect of the different twist angles on the cruise L/D, it can be seen the centerbody section twist angles have a comparable effect on the L/D. Increasing twist angle 1 results in an increase in cruise L/D, while increasing twist angles 2–6 results in a decrease in cruise L/D (except for twist angles 2 and 3 for the side fuel variant). An increase in twist angle of the outer wing root section results in a decrease in cruise L/D, with a slight increase in cruise L/D for an increase in the twist angle of the tip airfoil section.

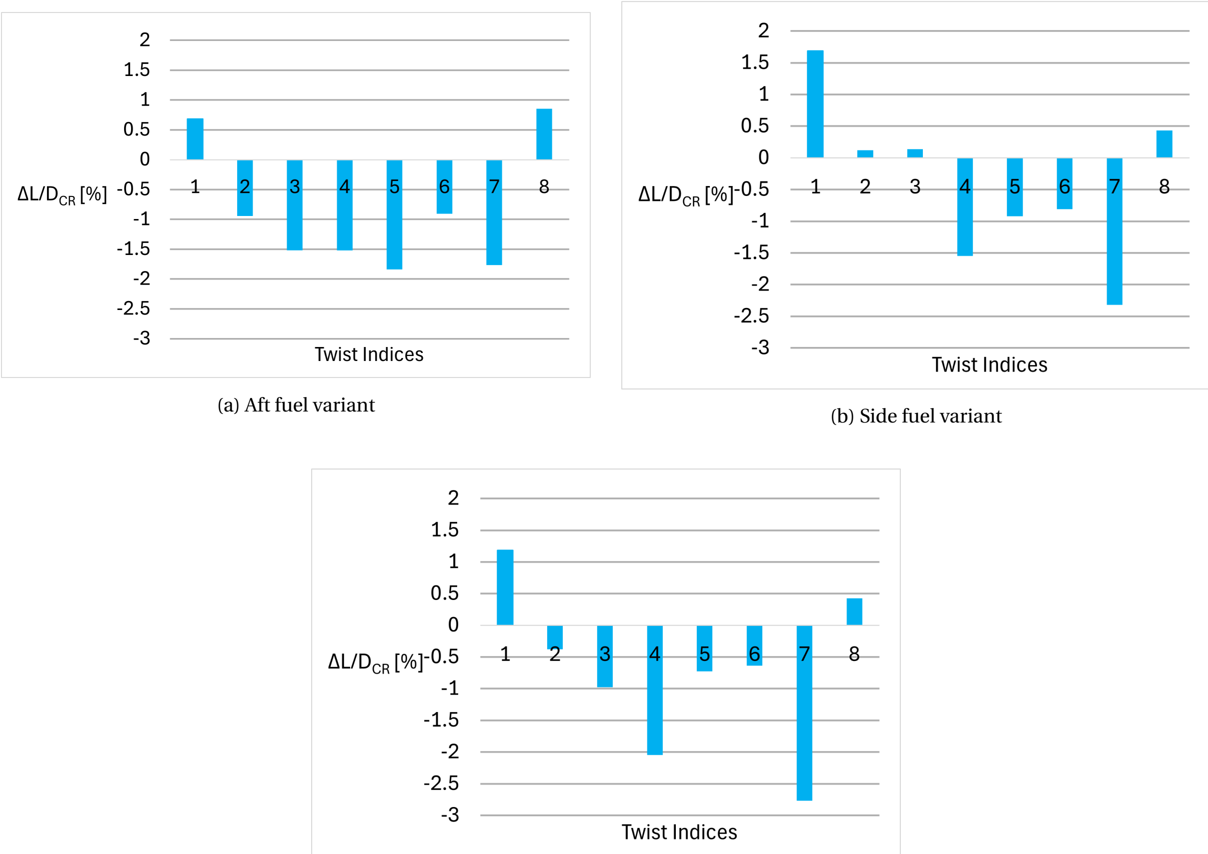

(a) Aft fuel variant

(b) Side fuel variant

(c) Mixed fuel variant

Figure 5.6: Cruise L/D sensitivity to a 2° twist angle increase for the BWB variants

The effect of the twist angles on the static margin of the variants is evaluated and the results are given in Figure 5.7. As shown in the results, the effect of each individual twist angle on the static margin is not very large. The trends across the variants are similar. Increasing the first twist angle improves the static margin, while increasing twist angles 3–5 results in a decrease in static margin. Twist angle 6 shows an improvement in static margin for an increase in twist angle for all the variants. For the outer wing, increasing the twist angle of the root section (twist angle 7) decreases the static margin, while increasing the angle of the tip section improves the static margin.

Considering the significant effects on the L/D of the aircraft and considering that combined changes of the twist angles could improve the static margin significantly, all the twist angles analysed in this section are included in the optimisations. The outer wing taper ratio and t/c are not included in the optimisations. As shown in subsection 5.1.2 the sensitivities of the performance metrics to those design parameters are relatively small. The decision is made to reduce the computational time of the optimisations by not including those design variables. Overall, it is clear that the complex sensitivities of all the performance metrics to the planform parameters and twist angles of the BWB concepts require an optimisation procedure to thoroughly search the design space for an optimal concept.

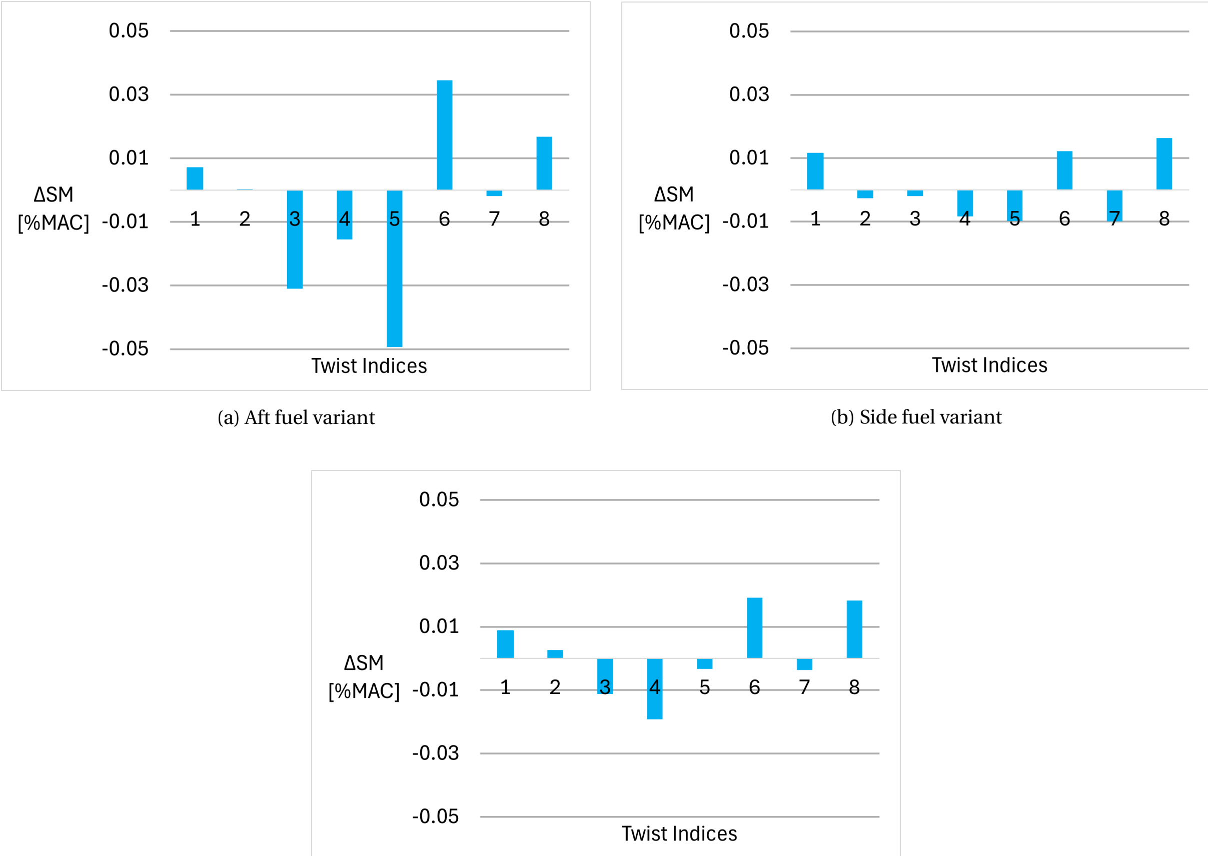

(a) Aft fuel variant

(b) Side fuel variant

(c) Mixed fuel variant

Figure 5.7: Static margin sensitivity to a 2° twist angle increase for the BWB variants

5.1.4. Cruise Conditions Sensitivity

The sensitivities of the OEM, cruise L/D, fuel mass and maximum L/D to the cruise conditions have been computed for the three variants. The cruise Mach number and cruise altitude were changed with respect to the baseline values. The Class 1 – Class 2 iterations were then performed to find the new converged design for the changed cruise conditions.

Side Fuel Variant

In Figure 5.8 the cruise condition sensitivity results for the side fuel variant are shown. In the matrix it is shown that the maximum L/D decreases for a higher Mach number, with the opposite happening for a decrease in Mach number. The changes in maximum L/D are mainly caused by wave drag changes, for a higher Mach number the wave drag increases and the opposite happens for a lower Mach number. The sensitivity of the cruise L/D to the Mach number follows the same trend, however the magnitude of the sensitivity is higher. This is due to the aircraft flying at a lower lift coefficient (further away from the optimal) when flying faster and due to the aerodynamic efficiency decreasing for a higher Mach number. The opposite is observed for a lower Mach number. The changes to the OEM are caused by the snowball effect which is a result of fuel mass changes. When considering the Breguet range equation, flying faster is beneficial for the required fuel mass. The cruise L/D reductions when flying faster however outweigh this benefit, resulting in an increase in required fuel mass. The opposite is again observed for a lower Mach number.

When considering the sensitivity of the metrics to the cruise altitude it is clear this BWB variant has a high sensitivity to the altitude. When flying higher, the maximum L/D increases. While the wave drag and profile drag slightly increase, a considerable increase in maximum L/D is observed. This can be explained by a large change in fuel mass when flying higher or lower. This has a large effect on the span and size of the side fuel tank region. This results in large changes in the aspect ratio of this BWB variant when changing the cruise altitude. At the same time flying at a different altitude will change the air density, resulting in a change in the required cruise lift coefficient. For an increase in cruise altitude the maximum L/D increases as well as the cruise lift coefficient, resulting in an increase in cruise L/D. Logically, the fuel mass required reduces. The opposite is observed for flying at a lower altitude.

Δ OEM	0.22	-0.11	-1.41	0.03
Δ $(L/D)_{max}$	-2.15	1.22	2.59	-1.59
Δ $(L/D)_{cr}$	-4.07	3.76	10.37	-11.21
Δ FM	1.83	-1.32	-8.95	6.98
	+ 0.02M	**- 0.02M**	**+ 3000ft**	**- 3000ft**

-12%	**-8%**	**-4%**	**0%**	**+4%**	**+8%**	**+12%**

Figure 5.8: Cruise condition sensitivity matrix for the side fuel BWB variant

Mixed Fuel Variant

The cruise condition sensitivities are also computed for the mixed fuel variant. In Figure 5.9 the results for this variant are shown. Similar sensitivities of the metrics to the cruise Mach number are observed as for the side fuel BWB variant, with only the magnitude of the sensitivities being slightly lower.

For changes in the cruise altitude different sensitivities are observed for the maximum L/D. When flying at a higher altitude the profile drag increases slightly, which causes the small reduction in maximum L/D. The opposite happens for a lower altitude. The effects of the cruise lift coefficient changing due to the different air densities are dominating, which means the sensitivities of the cruise L/D and fuel mass are comparable to those of the side fuel BWB variant, albeit a smaller magnitude. The different maximum L/D sensitivity can be explained by this BWB variant having a much smaller side fuel tank region. This means changes in fuel mass have a smaller effect on the aspect ratio of this variant.

Δ OEM	0.22	-0.11	-1.13	1.37
Δ $(L/D)_{max}$	-1.45	0.42	-0.22	0.13
Δ $(L/D)_{cr}$	-3.32	2.82	6.11	-6.82
Δ FM	0.97	-0.60	-5.58	6.18
	+ 0.02M	**- 0.02M**	**+ 3000ft**	**- 3000ft**

-12%	**-8%**	**-4%**	**0%**	**+4%**	**+8%**	**+12%**

Figure 5.9: Cruise condition sensitivity matrix for the mixed fuel BWB variant

Aft Fuel Variant

The cruise condition sensitivities of the last BWB variant, the aft fuel variant, are shown in Figure 5.10. When considering the magnitude of the sensitivities of the performance metrics to the cruise Mach number it is clear they are higher compared to those of the side fuel and mixed fuel BWB variants.

Changes in the wave drag for different Mach numbers are larger for this BWB variant than for the other two, which results in a higher sensitivity of the maximum L/D to the cruise Mach number. The cruise L/D and fuel mass sensitivities are also higher as a result of this.

The sensitivity of the maximum L/D to the cruise altitude is comparable to that of the mixed fuel variant. Flying at a higher altitude results in an increases in profile drag, which causes a reduction in maximum L/D. Despite this the higher lift coefficient required causes the cruise L/D to increase, which results in a decrease in required fuel mass. The opposite is observed when flying at a lower altitude.

Δ OEM	0.94	-0.47	-0.92	1.38
Δ $(L/D)_{max}$	-3.83	2.61	-0.50	0.19
Δ $(L/D)_{cr}$	-5.41	4.51	4.37	-5.66
Δ FM	3.60	-2.06	-3.95	5.24
	+ 0.02M	**- 0.02M**	**+ 3000ft**	**- 3000ft**

-12%	**-8%**	**-4%**	**0%**	**+4%**	**+8%**	**+12%**

Figure 5.10: Cruise condition sensitivity matrix for the aft fuel BWB variant

5.1.5. Gravimetric Efficiency Sensitivity

The sensitivity of the OEM, fuel mass and cruise L/D to the tank gravimetric efficiency is analysed. This is done by multiplying the total tank mass by a mass factor and performing the Class 1 – Class 2 iterations as usual. This means any volume effects of having thicker structural or insulation layers are not considered, solely the mass effects. Across the different variants the same trends are observed. The results for the side fuel variant are given in Figure 5.11, the results for all the variants are given in Appendix A.

The results obtained for the OEM and fuel mass are as expected. As the tank mass increases the required fuel mass for the design mission and the OEM of the aircraft increase as well. As there is a snowball effect (more fuel means more OEM, which means more fuel etc.), for low gravimetric efficiencies the OEM and fuel mass increase at a higher rate. For gravimetric efficiencies below what is shown in the results the weights increase rapidly, causing a sharp increase in the required amount of tanks. For the side fuel variant this means not enough room is available next to the cabin for all the required tanks. The gravimetric efficiency at which this happens is below 0.45.

The effect of the gravimetric efficiency on the cruise L/D depends on the outer shape of the aircraft and the cruise lift coefficient. For all variants similar behaviour is observed. As the gravimetric efficiency decreases, the cruise L/D increases slowly. This is due to the aircraft getting heavier and flying at a higher cruise lift coefficient. At a certain point the increased fuel mass requires additional tanks which causes a large change in outer shape, which is the jump to a different cruise L/D observed for the side fuel and aft fuel variants (for the aft fuel results see Appendix A). After this the increasing weight increases the cruise lift coefficient while the outer shape does not change significantly, meaning the cruise L/D slowly increases again.

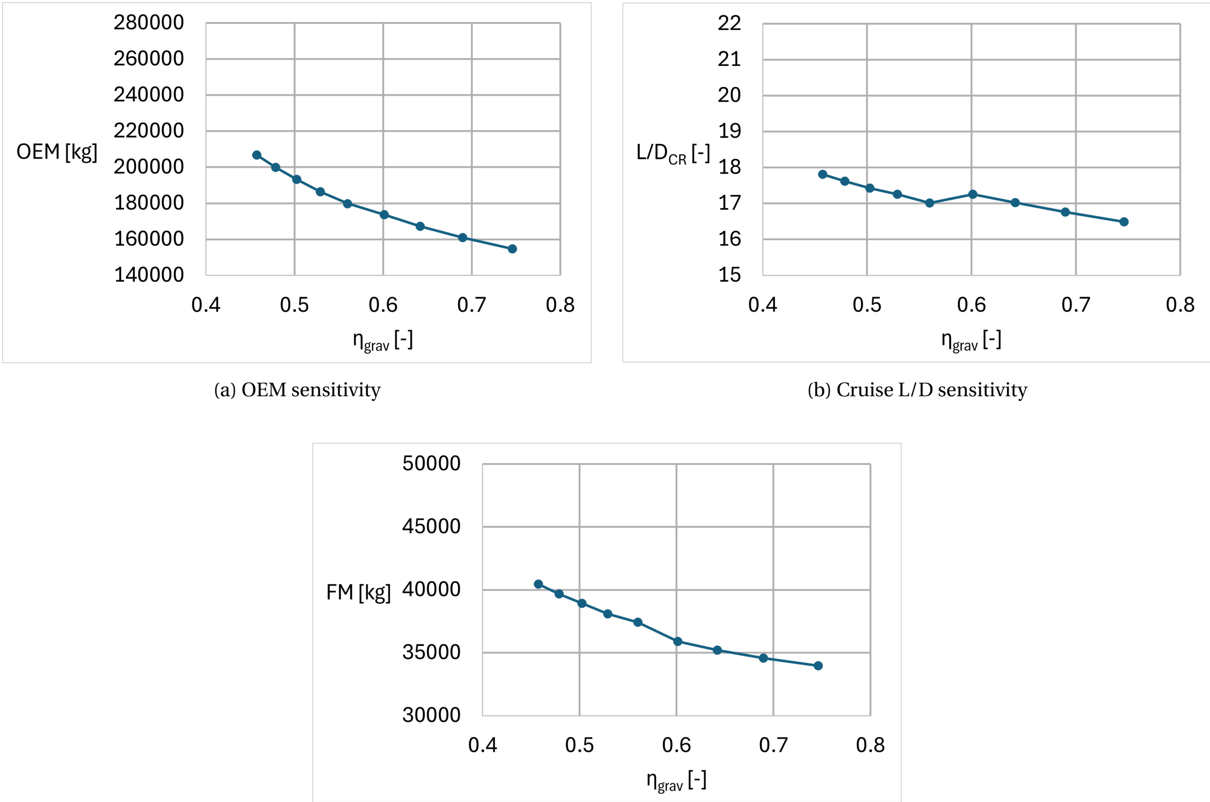

(a) OEM sensitivity

(b) Cruise L/D sensitivity

(c) Fuel mass sensitivity

Figure 5.11: OEM, cruise L/D and fuel mass sensitivity to tank gravimetric efficiency for the side fuel BWB variant

5.2. Planform Optimisation

As explained in section 3.9, an optimisation is performed to find the optimal BWB concept. Since there are 3 different exit design options and it is unclear which option offers the best evacuation and safety features, the best concept for each exit design will be presented and compared to each other. For the full list of the considered baseline variants refer back to section 3.9. The aircraft concepts will be ranked based on the fuel burn for the design missions. Only feasible designs (statically stable and able to reach the range) will be considered. If the difference in fuel burn between the wing engine and aft engine variants is small, the aft engine variant will be prioritised. When mounting the engines on the aft body this provides noise shielding, as well as the opportunity to apply BLI technologies. For reference, the planform optimisation of one BWB concept takes around 1 hour of computational time on a regular laptop.

5.2.1. 350 Passenger TLR Point

The planform optimisation results for the 350 passenger TLR point are presented in this subsection. For exit option 1 the optimal variant is found to be 2-Aft (3 cabin bays). Variant 6-Aft (2 cabin bays) is found to be the optimal variant for exit option 2. As there is only one viable cabin design for exit option 3, this variant is logically the optimal one for this exit option. Renders of the 3 concepts are given in Figure 5.12 and diagrams of the planforms are given in Figure 5.13. The weight specifications and performance metrics of the 3 concepts are listed in Table 5.3 and the geometrical specifications of the concepts are listed in Table 5.4. Note that b_{cb} is the width of the complete centerbody, including the side tank region and excluding the transition region.

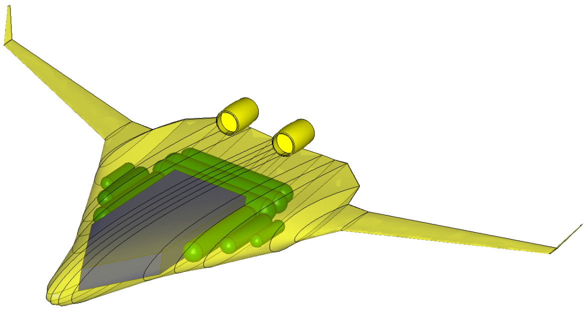

(a) BWB variant 2-Aft

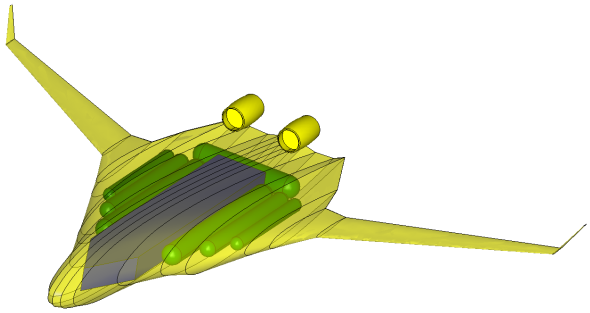

(b) BWB variant 6-Aft

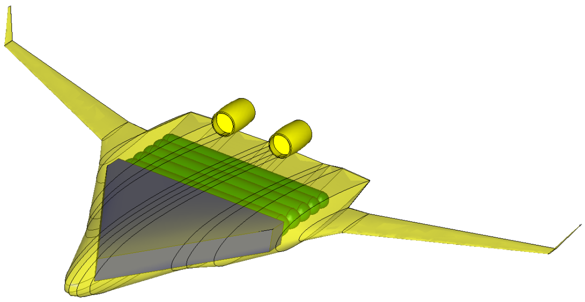

(c) BWB variant 11-Aft

Figure 5.12: Isometric view renders of the planform optimised concepts (350pax, 10 000 km)

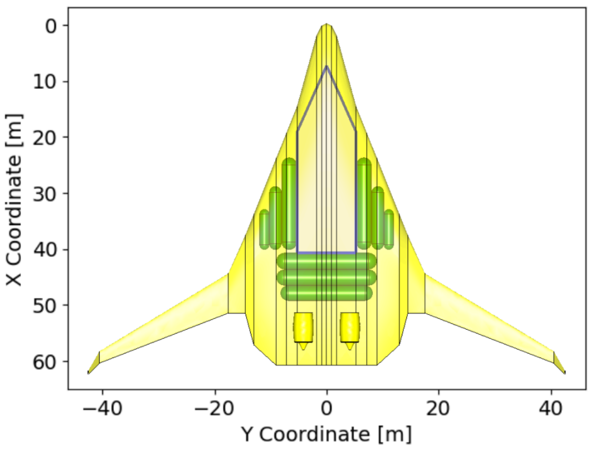

(a) BWB variant 2-Aft

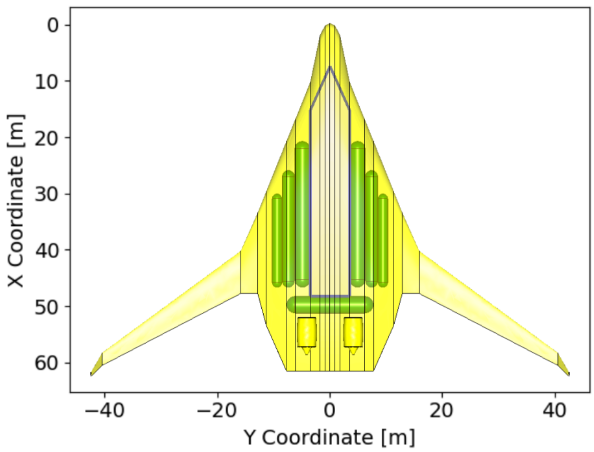

(b) BWB variant 6-Aft

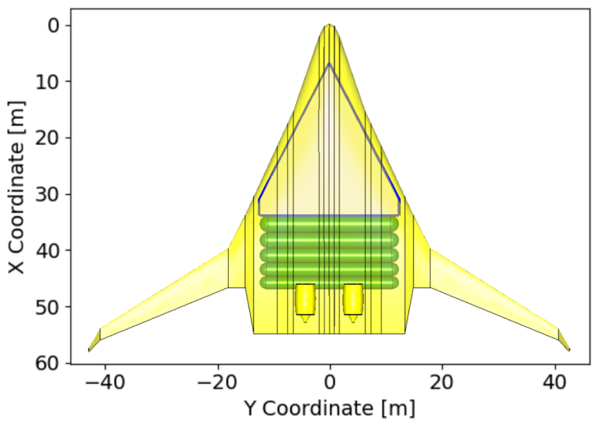

(c) BWB variant 11-Aft

Figure 5.13: Planform diagrams of the planform optimised concepts (350pax, 10 000 km)

For all the exit design options the best concepts had a small difference in fuel burn between the wing mounted and aft mounted engine options. It is therefore decided to select the aft engine variants for reasons discussed earlier. As can be seen, the concept with exit design option 1 has the lowest fuel burn for the design mission. All the concepts have an ample static margin, giving confidence in the stability in the concepts despite the AVL pitching moment limitations discussed earlier in section 4.2. Compared to the best performing concept, 2-Aft, concept 7-Aft has an increase in fuel burn of 0.3 %, which is negligible considering the accuracy of the model. The fuel burn of concept 11-Aft is 3.6 % higher. When comparing the fuel burn of the absolute worst concept (of all cabin designs) to the best concept, the difference in fuel burn is 21.9 %. The largest difference in maximum L/D between the optimal concepts per exit option is computed to be 2 %. The maximum difference in OEM is 8.4 %.

Table 5.3: Weight and performance specifications of the planform optimised concepts for the different exit options (350pax, 10 000 km)

Parameter	**Exit Option 1**	**Exit Option 2**	**Exit Option 3**
Variant	2-Aft	6-Aft	11-Aft
OEM [kg]	182 000	179 000	194 000
FM [kg]	30 200	30 300	31 300
MTOM [kg]	247 000	244 000	261 000
SM [%]	13.1	7.3	9.7
L/D_{cr} [-]	22.1	21.6	22.7
L/D_{max} [-]	25.2	24.7	25.2
$C_{L,cr}$ [-]	0.153	0.158	0.172
m_{tank} [kg]	16 800	18 200	17 400
η_{grav} [-]	0.642	0.625	0.642

Table 5.4: Geometrical specifications of planform optimised concepts for the different exit options (350pax, 10 000 km). Design variables that are on a variable bound are in bold

Parameter	**Exit Option 1**	**Exit Option 2**	**Exit Option 3**
Variant	2-Aft	6-Aft	11-Aft
n_{bays} [-]	3	2	7
n_{tanks} [-]	9	7	5
ϕ_f [-]	0.46	0.83	**0**
Λ_{cab} [deg]	**66.0**	**66.0**	62.8
Λ_w [deg]	31.1	36.3	32.0
S_{ref} [m^2]	1430	1370	1350
b [m]	80	80	80
b_{cb} [m]	23.7	20.4	24.4
b_{tr} [m]	10.9	11.0	11.0
b_{wing} [m]	45.4	48.6	44.6
A [-]	4.48	4.68	4.75
c_0 [m]	60.3	61.2	54.2
L_{cab} [m]	33.0	40.4	26.6
b_{cab} [m]	10.4	7.0	24.4
S_{cab} m^2	283	254	359

The larger fuel burn of concept 11-Aft can be explained by the drastically different cabin shape due to the sidewall length constraint of exit design option 3. Since the cabin is almost a perfect triangular shape, the larger diagonal part in the cabin makes for a more inefficient distribution of the cabin bays. This is clearly shown by the much larger cabin floor area of the 7 bays cabin, compared to the cabins with 2 or 3 bays. Since the cabin structural weight depends highly on the cabin floor area, the cabin structure of concept 11-Aft is much heavier. This is reflected by the larger OEM of this concept. The cruise L/D is larger for concept 11-Aft, as it is flying at a higher cruise lift coefficient due to the increased weight, while the maximum L/D is comparable for the 2 concepts. Despite the cruise L/D improvements, the fuel burn is larger due to the larger aircraft weight.

When comparing the concepts for exit options 1 and 2, the difference in fuel burn is very small. The addition of the ventral exits at the rear of the cabin limits the length of the tanks next to the cabin to keep space free for the ventral exits. It appears the addition of the ventral exits at the rear of the cabin has a considerable effect on the aircraft level performance, as the concept with ventral exits and 3 cabin bays, concept 7-Aft, has an increase in fuel burn of 3.3 % compared to concept 2-Aft (which has exit option 1). This is caused by a lower cabin leading edge sweep angle, which leads to a lower cruise L/D. The leading edge sweep angle is lower to allow the side tank region span to be higher. The increased side tank region span offsets the limited length of the tanks in terms of available volume in the tank region. The side tank fuel ratios of concepts 2-Aft (0.461) and 7-Aft (0.459) are roughly equal. For the ventral exit option (option 2) it turns out that a 2 bay cabin with the ventral exits (concept 6-Aft) has a lower fuel burn than one with 3 bays (concept 7-Aft), leading to concept 6-Aft being the optimal one for exit option 2. The cabin of concept 2-Aft is wider compared to the cabin of concept 6-Aft, which leads to a larger triangular part of the cabin. For the same reasons as discussed earleir, the result is a higher cabin area. The higher cabin area of concept 2-Aft causes the OEM to be higher, compared to concept 6-Aft. Despite the higher OEM the cruise L/D of concept 2-Aft is higher, resulting in a slightly lower fuel burn for this concept.

As the fuel tank fitting is based on the cabin height (including the cargo hold), the tank diameters of the different concepts are comparable, as the cabin height is constant for the concepts. This results in comparable gravimetric efficiencies for the concepts as well. Concept 6-Aft has a slightly lower gravimetric efficiency, which is caused by its tanks being roughly the same diameter, but considerably longer. This affects the total gravimetric efficiency.

When comparing the planforms and shapes of the concepts, it is clear a large cabin sweep angle leading to a narrow centerbody leads to the best aircraft performance. In fact, the cabin sweep angle of 66° is on the upper bound, which is the case for concepts 2-Aft and 6-Aft. Even with a drastically different cabin shape the outer shape is quite comparable. It can be argued that the difference in fuel burn between the best and worst cabin exit designs of 3.6 % indicates drastically different internal layouts lead to a comparable aircraft level performance.

The twist and thickness distributions of the optimal concepts for each exit design are given in Figure 5.14 and Figure 5.15, respectively. For all the concepts the thickness of the centerbody increases when moving further outboard. This is due to the required height of the internal components not changing, however due to the swept cabin leading edge the chord length of the airfoil sections decreases. The jump in twist distribution at around 25 % of the semi-span observed for each of the concepts is caused by the change in airfoil profile at roughly this location. The airfoil profile changes from a reflexed one to a symmetrical one.

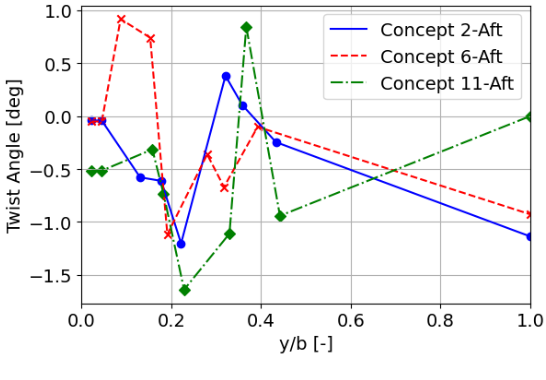

Figure 5.14: Twist angle distribution of the optimal BWB concepts (350pax, 10 000 km)

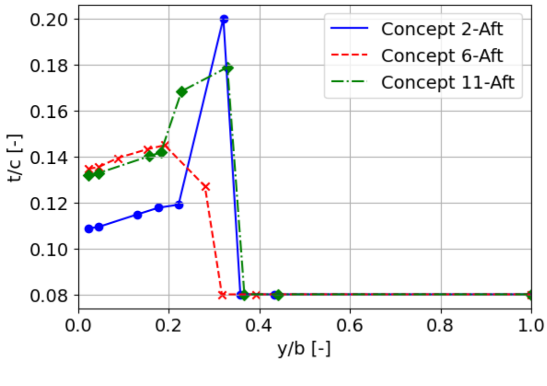

Figure 5.15: Thickness to chord ratio distribution of the optimal BWB concepts (350pax, 10 000 km)

5.2.2. 250 Passenger TLR Point

The planform optimisation is also performed for BWB concepts with 250 passengers and a design range of 7000 km. For this TLR point only the aft-mounted engine options are considered, for the same reasons as discussed in the previous subsection. For exit option 1 the optimal variant is found to be concept B (3 cabin bays), while concept F (3 cabin bays) is the optimal variant for exit option 2. Two different cabin designs are feasible for exit option 3 (meaning they satisfy the sidewall length constraint), however the optimal variant is concept K (5 cabin bays). Renders of the optimal concepts are given in Figure 5.16 and planform diagrams are given in Figure 5.17 The weight specifications and performance metrics of the 3 optimal concepts are listed in Table 5.5, while the geometrical specifications are listed in Table 5.6

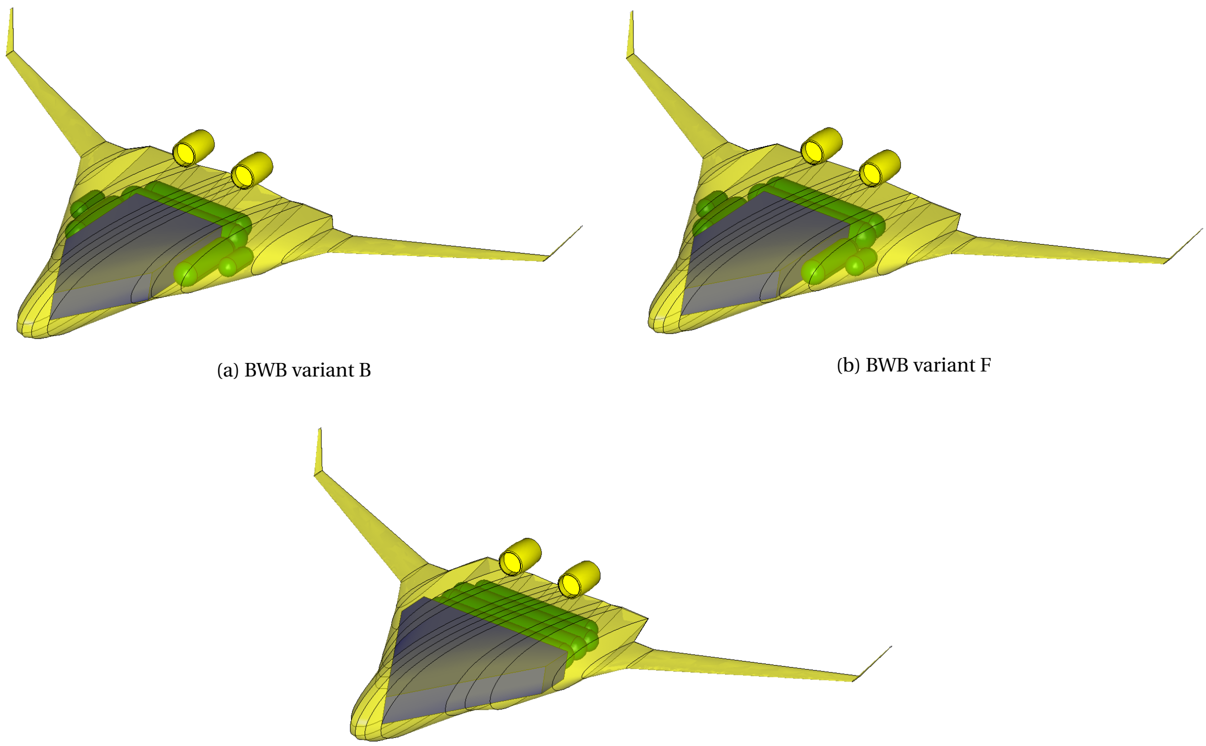

(a) BWB variant B

(b) BWB variant F

(c) BWB variant K

Figure 5.16: Isometric view renders of the planform optimised concepts (250pax, 7000 km)

Table 5.5: Weight and performance specifications of the planform optimised concepts for the different exit options (250pax, 7000 km)

Parameter	**Exit Option 1**	**Exit Option 2**	**Exit Option 3**
Variant	B	F	K
OEM [kg]	109 000	108 000	114 000
FM [kg]	15 800	15 700	15 900
MTOM [kg]	151 000	149 000	155 000
SM [%]	20.4	18.1	15.0
L/D_{cr} [-]	20.0	19.6	20.6
L/D_{max} [-]	24.8	24.6	24.9
$C_{L,cr}$ [-]	0.147	0.145	0.160
m_{tank} [kg]	8600	8400	9100
η_{grav} [-]	0.648	0.651	0.636

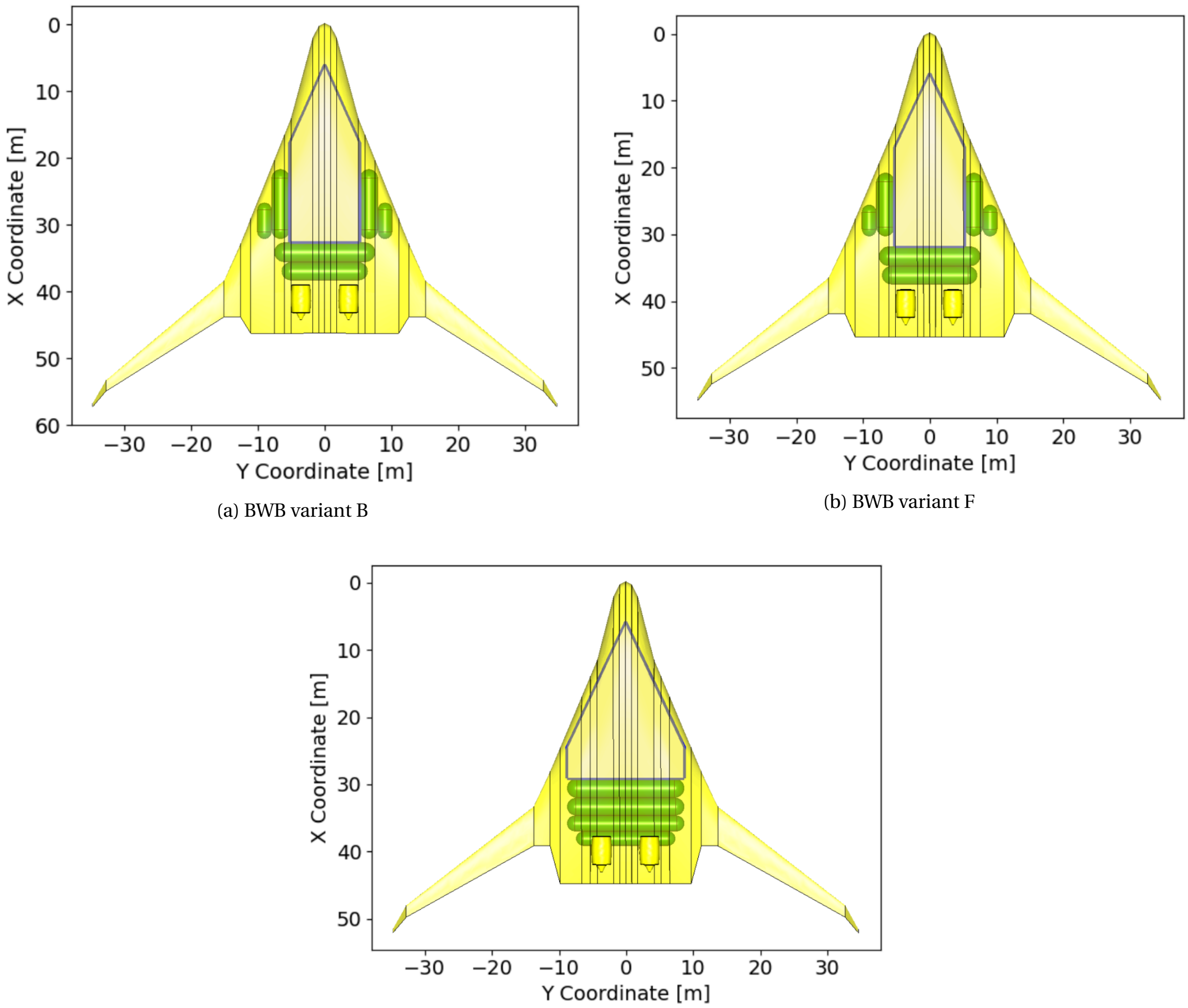

(a) BWB variant B

(b) BWB variant F

(c) BWB variant K

Figure 5.17: Planform diagrams of the planform optimised concepts (250pax, 7000 km)

Table 5.6: Geometrical specifications of the planform optimised concepts for the different exit options (250pax, 7000 km). Design variables that are on a variable bound are in bold

Parameter	Exit Option 1	Exit Option 2	Exit Option 3
Variant	B	F	K
n_{bays} [-]	3	3	5
n_{tanks} [-]	6	6	4
ϕ_f [-]	0.45	0.41	**0**
Λ_{cab} [deg]	**66.0**	64.8	64.9
Λ_w [deg]	40.2	39.2	37.8
S_{ref} [m^2]	910	910	860
b [m]	65	65	65
b_{cb} [m]	20.0	20.2	17.4
b_{tr} [m]	9.9	9.9	9.9
b_{wing} [m]	35.1	34.9	37.7
A [-]	4.66	4.66	4.89
c_0 [m]	46.2	45.4	44.8
L_{cab} [m]	26.6	25.9	23.2
b_{cab} [m]	10.4	10.4	17.4
S_{cab} m^2	216	212	243

The concept with exit option 2 (ventral exits, concept F) offers the best performance in terms of fuel burn, however the difference compared to the other concepts is small. Although the cruise L/D of this concept is the lowest out of the 3 concepts, it has the lowest OEM, which results in a slightly lower fuel burn than the other concepts. The low cruise L/D is caused by both a low lift coefficient and low aerodynamic efficiency overall, which can be seen when comparing the maximum L/D values of the concepts. The low OEM of concept F can be explained by the tank gravimetric efficiency being the highest out of the concepts and the cabin area being the smallest. The optimal concept for exit option 1, concept B, has a 0.6 % higher fuel burn compared to concept F. Concept K, with exit option 3, has a 1.3 % higher fuel burn for the design mission. The largest difference in maximum L/D between the optimal concepts for the exit options is found to be 1.2 %, while the maximum difference in OEM is 5.7 %.

When comparing the optimal concepts for exit options 1 and 2, the concepts appear to be very similar. Both concepts B and F have a cabin with 3 bays and around 40 to 45 % of the total fuel next to the cabin. Similarly to what is observed for the other TLR point, the ventral exits limit the length of the side tanks. This causes more tanks to be placed behind the cabin for concept F (represented by the lower side tank ratio). It also causes the cabin leading edge sweep angle to be slightly lower, to allow a larger side tank region span. Although those changes compared to concept B cause the aerodynamic efficiency of this concept to be lower, the shorter cabin of concept F (due to the different exit design) results in a lower cabin weight. As the side fuel tanks of concept F are shorter than those of concept B, but the same length, the gravimetric efficiency is slightly higher. Those factors result in a lower OEM and ultimately in a slightly lower fuel burn for concept F.

Larger differences in planform are observed between concept F and concept K. Due to the sidewall length constraint the optimal concept for exit option 3 has 5 cabin bays and all of the fuel tanks behind the cabin. Similar to what is seen for the 350 passenger concepts, a wider cabin results in a larger cabin area. This causes the OEM of concept K to be considerably higher than that of concept F. Another factor contributing to the higher OEM is the gravimetric efficiency. Although the tanks have similar radii as those of concept F, the length of the tanks behind the cabin is higher, causing a lower gravimetric efficiency. On the other hand, the cruise L/D of concept K is much better, resulting in only a slightly higher fuel burn for this concept. The higher cruise L/D of concept K can be explained both by a higher cruise lift coefficient and a better aerodynamic efficiency, which is represented by the higher maximum L/D of this concept. When considering the geometrical specifications of concept K, it is clear the aspect ratio of this concept is higher than that of concept F due to a lower planform area. This lower planform area can be explained by the concepts with side fuel tanks having an unused part of the aftbody behind the side tanks. The concept with only fuel tanks behind the cabin has the fuel tanks stretching the whole aftbody span.

Just as for the 350 passenger TLR point, the argument can be made that although the internal layouts of the BWB variants differ significantly, the aircraft level performance is comparable. Even more so for this TLR point, as the worst exit option has a 1.3 % higher fuel burn compared to the best exit option. For the 350 passenger TLR point this difference is 3.6 %. The difference in fuel burn between the absolute best and worst BWB variants (across all the cabin designs) for the 250 passenger TLR point is found to be 8.7 %. This difference is 21.9 % for the other TLR point. The outer shapes of the optimal BWB concepts are very similar as well, when considering the planform diagrams in Figure 5.17.

In Figure 5.18 the twist angle distributions of the optimal concepts are shown and in Figure 5.19 the thickness to chord distributions are shown. The thickness distributions of concepts B and F are very similar, while the thickness of the centerbody of concept K is considerably higher. The twist angle distributions of concept B and F are quite similar as well, with larger differences observed for concept K.

To confirm that exit options 1 and 2 result in reduced performance compared to exit option 3 for wide cabins, a cabin with 5 bays was evaluated for all the exit options. As expected the concept with exit option 3 delivered the best performance in terms of fuel burn out of the three concepts considered.

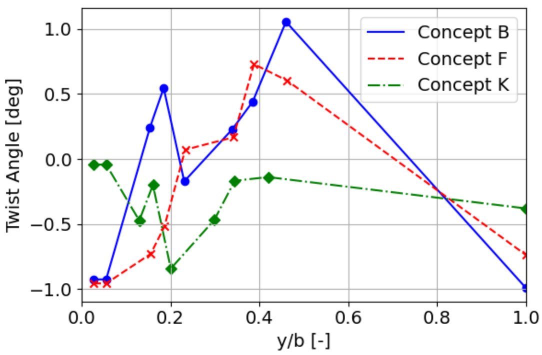

Figure 5.18: Twist angle distribution of the optimal BWB concepts (250pax, 7000 km)

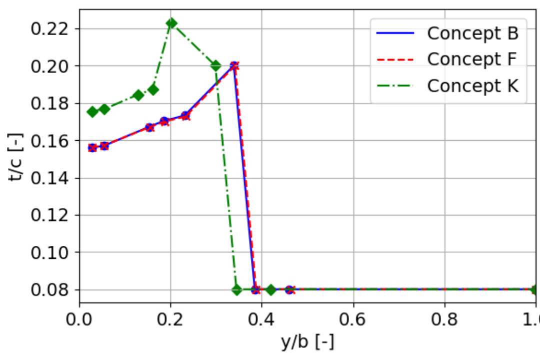

Figure 5.19: Thickness to chord ratio distribution of the optimal BWB concepts (250pax, 7000 km)

5.3. Cruise Conditions Optimisation

After obtaining the planform optimised concepts, the cruise conditions of those concepts are optimised. As explained in subsection 3.9.3 the planform input parameters of the BWB concepts are not changed and only the cruise altitude and cruise Mach number are changed. After finding the optimal cruise conditions the Class 1 – Class 2 iterations are performed to find the new fuel mass required for the design mission. The new converged BWB concepts are indicated by the addition of '-cruise' to their variant names.

5.3.1. 350 Passengers TLR Point

The results for the BWB concepts for a design mission of 350 passengers and range of 10 000 km are presented and discussed in this subsection. Just as for the planform optimisation the optimal concept for each exit design is presented. The weight, performance and cruise condition data of the optimal concepts is given in Table 5.7. The geometrical specifications of the concepts are listed in Table 5.8

Table 5.7: Weight, performance and cruise condition specifications of the cruise condition optimised concepts for the different exit options (350pax, 10000 km). Design variables that are on a variable bound are in bold

Parameter	**Exit Option 1**	**Exit Option 2**	**Exit Option 3**
Variant	1-Aft-cruise	6-Aft-cruise	11-Aft-cruise
Cruise Mach [-]	**0.84**	**0.84**	**0.84**
Cruise Altitude [ft]	46400	41000	43900
OEM [kg]	179000	176000	190000
FM [kg]	27000	27300	28400
MTOM [kg]	241000	238000	254000
SM [%]	6.9	7.2	11.3
L/D_{cr} [-]	24.0	23.3	24.1
L/D_{max} [-]	24.0	24.7	24.2
$C_{L,cr}$ [-]	0.244	0.189	0.232
m_{tank} [kg]	18700	17200	15500
η_{grav} [-]	0.590	0.613	0.647

Table 5.8: Geometrical specifications of the cruise condition optimised concepts for the different exit options (350pax, 10000 km). Design variables that are on a variable bound are in bold

Parameter	**Exit Option 1**	**Exit Option 2**	**Exit Option 3**
Variant	1-Aft-cruise	6-Aft-cruise	11-Aft-cruise
n_{bays} [-]	2	2	7
n_{tanks} [-]	7	7	5
ϕ_f [-]	0.95	0.83	**0**
Λ_{cab} [deg]	**66.0**	**66.0**	62.8
Λ_w [deg]	33.4	36.3	32.0
S_{ref} [m^2]	1370	1350	1350
b [m]	80	80	80
b_{cb} [m]	20.2	19.7	24.4
b_{tr} [m]	11.0	11.0	11.0
b_{wing} [m]	48.8	49.3	44.6
A [-]	4.68	4.74	4.75
c_0 [m]	61.6	61.2	54.2
L_{cab} [m]	40.6	40.4	23.2
b_{cab} [m]	7.0	7.0	24.4
S_{cab} m^2	256	254	359

At first the optimiser found the optimal cruise altitude for variant 6-Aft-cruise to be 47000 ft, however the removal of 2 side tanks due to a reduced required fuel mass caused the concept to be unstable (SM < 5 %). When imposing the static margin constraint on this concept it is found the cruise altitude is limited to 41000 ft.

For exit option 2 the optimal concept did not change, however for the first exit option concept 1-Aft-cruise is now the optimal concept. The required fuel mass for the design mission reduced by 10.8 % for the optimal concept for exit option 1, when optimising the cruise conditions. For exit option 2 the required fuel mass reduced by 10 % and for exit option 3 it reduced by 9.4 %. The difference in fuel mass of concept 6-Aft-cruise compared to concept 1-Aft-cruise is now 1.1 %, while the difference of concept 11-Aft-cruise compared to 1-Aft-cruise is now 5.2 %. The percentage difference in fuel burn between the optimal concepts increases when the cruise conditions of each concept are optimised, compared to the optimal concepts with constant cruise conditions. The difference in fuel burn between the absolute best and worst cruise condition optimised concepts is found to be 18.4 %, which is slightly lower than the spread in fuel burn for the planform optimised concepts for this TLR point. The difference in maximum

L/D for the optimal concepts for each exit design is 2.9 %. For the OEM spread of the optimal concepts the difference is found to be 8 %. This is comparable to the differences found for the planform optimised concepts, with constant cruise conditions.

As observed in Table 5.4 the cruise lift coefficients of the planform optimised concepts for constant cruise conditions are quite low, resulting in a considerably lower cruise L/D compared to the maximum achievable L/D. The low cruise lift coefficients can be explained by a low wing loading of the BWB concepts. To fly at a higher lift coefficient the altitude can be increased, which is what is observed in the cruise condition optimisations. For this TLR point the optimal cruise altitudes found are in the range of 41 000 to 46 000 ft, which is quite high. As mentioned in subsection 3.9.3 the effects of changing the cruise altitude are not captured fully in this model, through limitations which are explained in that subsection. The cruise Mach number of all the concepts is at the upper limit (which is set due to limitations of the wave drag estimations), as flying faster means less time is spent in the air, reducing the fuel burn. The estimated wave drag did not significantly limit the cruise Mach number within the bounds, only in a few concepts (3-Aft-cruise, 5-Aft-cruise). A more accurate wave drag estimation could impose different limits on the cruise Mach number, meaning the used model has some limitations with respect to the accuracy of the optimal cruise Mach number.

In Figure 5.20 renders of the optimal concepts are given and in Figure 5.23 planform diagrams are given. In Figure 5.21 the twist distributions are shown and in Figure 5.22 the thickness to chord distributions are given. When comparing the different concepts it is again clear concept 11-Aft has the worst performance due to the larger OEM, caused by the wider cabin. Despite having the best gravimetric efficiency and cruise L/D, the large OEM of this concept causes the fuel burn to be higher. Concept 6-Aft-cruise is very similar to concept 1-Aft-cruise, however due to the margin taken at the rear for the ventral exits more fuel is placed behind the cabin for concept 6-Aft-cruise. This is represented by the lower side fuel ratio of this concept. It can also be seen that the gravimetric efficiencies of concepts 1-Aft-cruise and 6-Aft-cruise are quite low, which is a result of the side tanks being quite long, while the most outboard side tanks have a relatively low tank radius as well. It is clear the designs with a narrow cabin (2 cabin bays) and most of the fuel next to the cabin are the best performing concepts for this TLR point.

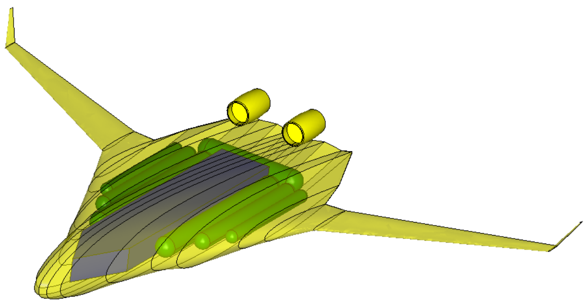

(a) BWB variant 1-Aft-cruise

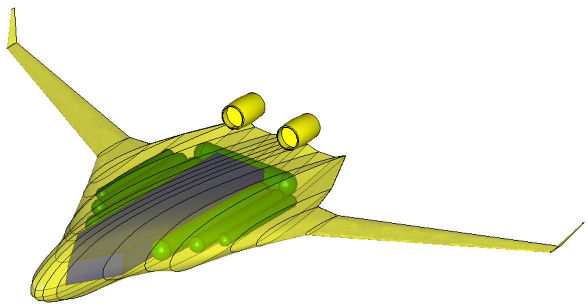

(b) BWB variant 6-Aft-cruise

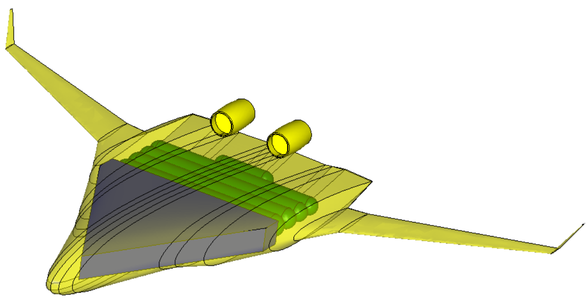

(c) BWB variant 11-Aft-cruise

Figure 5.20: Isometric view renders of the cruise condition optimised concepts (350pax, 10 000 km)

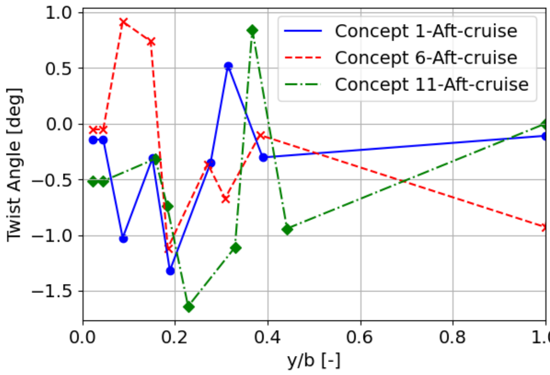

Figure 5.21: Twist angle distribution of the cruise condition optimised BWB concepts (350pax, 10 000 km)

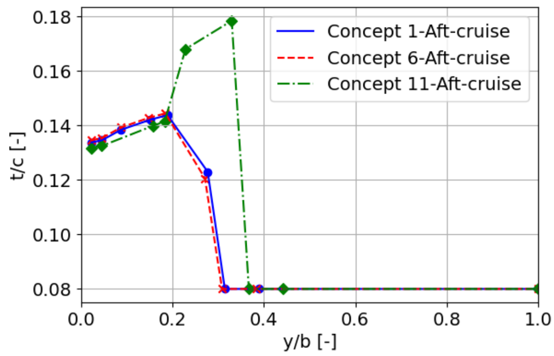

Figure 5.22: Thickness to chord ratio distribution of the cruise condition optimised BWB concepts (350pax, 10 000 km)

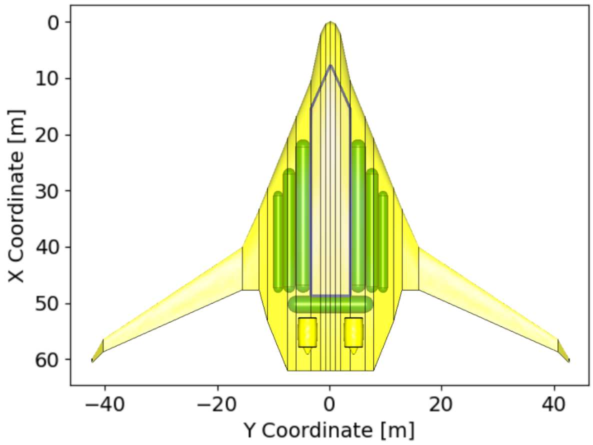

(a) BWB variant 1-Aft-cruise

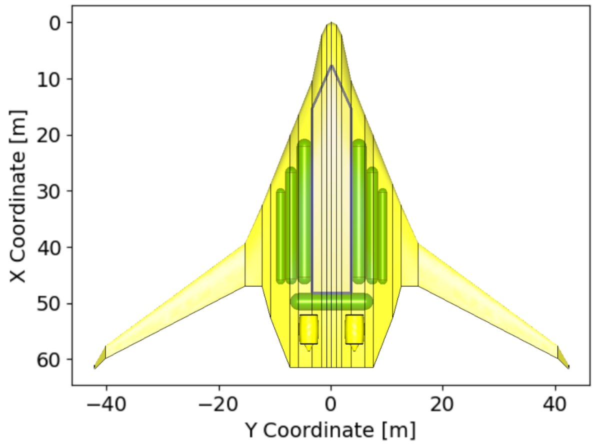

(b) BWB variant 6-Aft-cruise

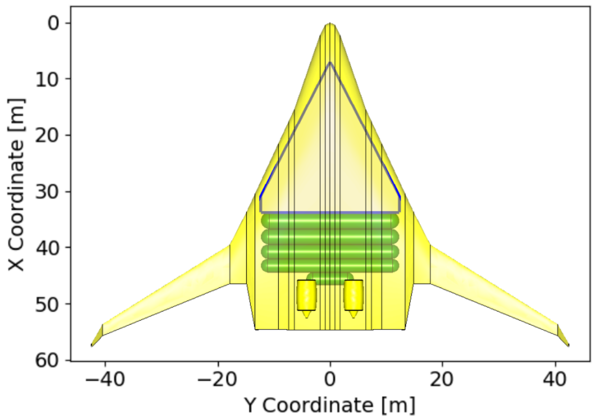

(c) BWB variant 11-Aft-cruise

Figure 5.23: Planform diagrams of the cruise condition optimised concepts (350pax, 10 000 km)

5.3.2. 250 Passenger TLR Point

The cruise condition optimisations are also performed for the second TLR point, which is 250 passengers and a design cruise range of 7000 km. The weight, performance and cruise condition specifications of the optimal concepts are given in Table 5.9 and the geometrical specifications are listed in Table 5.10.

Table 5.9: Weight, performance and cruise condition specifications of the cruise condition optimised concepts for the different exit options (250pax, 7000 km). Design variables that are on a variable bound are in bold

Parameter	**Exit Option 1**	**Exit Option 2**	**Exit Option 3**
Variant	A-cruise	E-cruise	K-cruise
Cruise Mach [-]	**0.84**	**0.84**	**0.84**
Cruise Altitude [ft]	**48000**	**48000**	**48000**
OEM [kg]	102 000	101 000	105 000
FM [kg]	13 000	12 800	12 800
MTOM [kg]	140 000	139 000	143 000
SM [%]	15.3	17.1	22.2
L/D_{cr} [-]	23.1	23.3	24.1
L/D_{max} [-]	23.4	23.7	24.4
$C_{L,cr}$ [-]	0.243	0.240	0.272
m_{tank} [kg]	8100	7600	7200
η_{grav} [-]	0.616	0.626	0.639

Table 5.10: Geometrical specifications of the cruise condition optimised concepts for the different exit options (250pax, 7000 km). Design variables that are on a variable bound are in bold

Parameter	**Exit Option 1**	**Exit Option 2**	**Exit Option 3**
Variant	A-cruise	E-cruise	K-cruise
n_{bays} [-]	2	2	5
n_{tanks} [-]	4	4	3
ϕ_f [-]	**1**	**1**	**0**
Λ_{cab} [deg]	**66.0**	65.9	64.8
Λ_w [deg]	36.2	39.9	37.8
S_{ref} [m^2]	870	870	790
b [m]	65	65	65
b_{cb} [m]	15.9	16.3	17.4
b_{tr} [m]	9.9	9.9	9.9
b_{wing} [m]	39.2	38.8	37.7
A [-]	4.88	4.87	5.36
c_0 [m]	46.9	46.5	41.1
L_{cab} [m]	31.6	31.3	23.2
b_{cab} [m]	7.0	7.0	17.4
S_{cab} m^2	192	191	242

The optimal cruise altitudes of all the optimal concepts is found to be the upper bound set in the optimisation, which is 48 000 ft. Again the limitations of the model with respect to the cruise altitude and the low wing loading of the original concepts causes the cruise altitude to be quite high. At this altitude the cruise L/D of all three concepts is much closer to the maximum L/D, as the lift coefficient is closer to the optimal one. The cruise Mach numbers are also on the upper bound, for reasons discussed in the previous subsection.

For this TLR point the optimal concepts for the first two exit options shifts to a more narrow cabin when optimising the cruise conditions. Instead of the optimal designs having 3 cabin bays for those exit options, the optimal designs now have 2 cabin bays and all of the fuel next to the cabin. Similarly to the planform optimised concepts, exit option 2 provides the best performance in terms of fuel burn, together with exit option 1. The optimal concepts for the other exit options have a very comparable performance though, as concept A-cruise has a 1.6 % higher fuel burn than concept E-cruise. Concept K-cruise has a similar fuel burn to concept E-cruise. When comparing concepts A-cruise and E-cruise it can be seen the concepts are very similar. The tank gravimetric efficiency of concept E-cruise is slightly better, as the length of the side tanks is smaller. Although this results in a slightly wider centerbody, the reduced fuel tank mass and slightly lower cabin mass result in an overall lower OEM of this concept. The aerodynamic efficiency of this concept is also better, resulting in the lower fuel burn. Concept K-cruise has a larger OEM due to the wider cabin, which has a larger cabin floor area and thus larger cabin mass. However, the cruise and maximum L/D of this concept are higher than those of concept E-cruise. The OEM and L/D differences cancel each other out, with a similar fuel burn as a result.

The fuel burn of the best cruise condition optimised concept for the first exit option reduced by 17.8 %, while for the second exit option this reduction is 18.7 %. For the third exit option the fuel burn of the best concept reduced by 19.3 %. The difference in fuel burn between the absolute best and worst cruise condition optimised BWB concepts for this TLR point is 8.5 %. The percentage spread between the best and worst concepts did not change much when optimising the cruise conditions, as this spread is 8.7 % for the planform optimised concepts. For the maximum L/D the difference between the optimal concepts each exit option is 4.3 %, which is slightly higher than what is observed for the planform optimised concepts. The difference in OEM of the optimal concepts is found to be 4 %, which is lower than the difference in OEM of the planform optimised concepts.

Renders of the cruise condition optimised concepts for the 250 passenger TLR point are shown in Figure 5.24 and planform diagrams of the concepts are shown in Figure 5.27. The twist and thickness distributions are presented in Figure 5.25 and Figure 5.26, respectively. The planforms of concepts A-cruise and E-cruise are very similar, which is also represented by the thickness distribution. Concept K-cruise has a larger centerbody thickness to chord ratio, which is caused by the shorter centerbody. When moving outboard the thickness increases further, which is due to the constant cabin height but decreasing chord length of the airfoil sections. For concepts A-cruise and E-cruise this effect is less, as the tank radius is decreasing when moving outboard. This means although the chord length of the airfoil sections is decreasing, the required height of the sections is also decreasing. The same trends in the thickness to chord ratio distributions are observed for the concepts of the other TLR point as well. The twist angle distributions are different between the concepts for this TLR point.

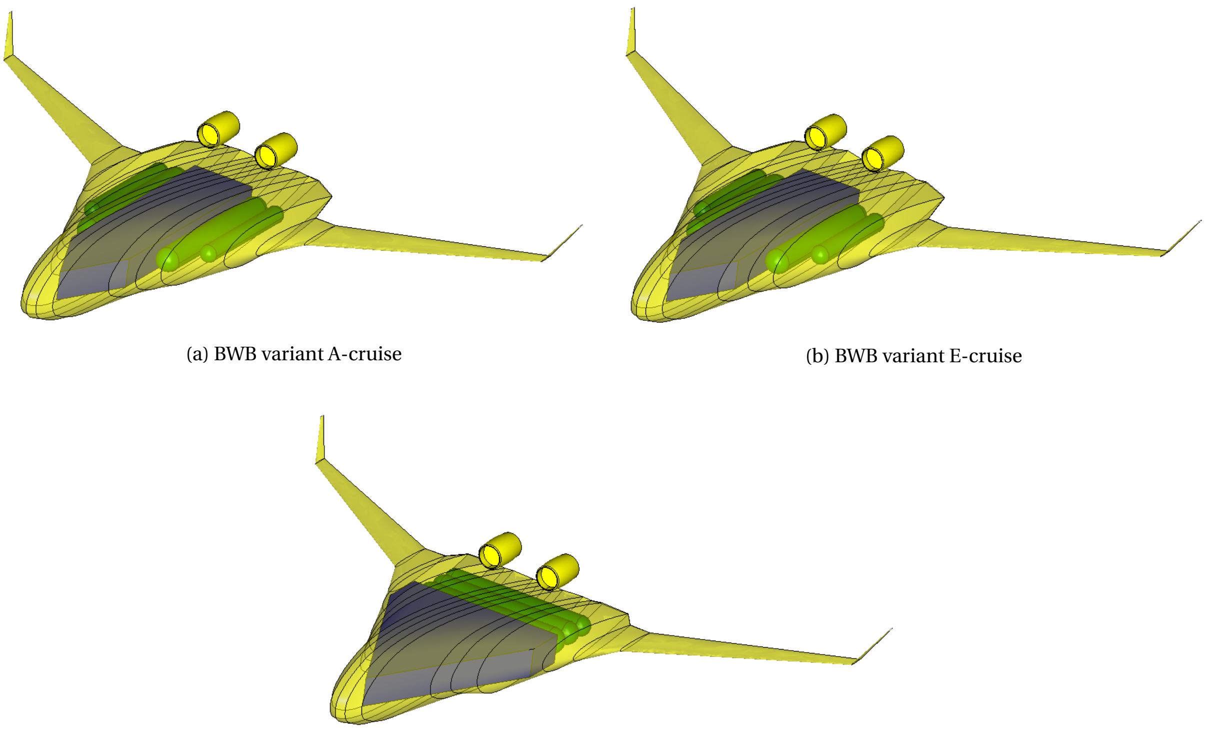

(a) BWB variant A-cruise

(b) BWB variant E-cruise

(c) BWB variant K-cruise

Figure 5.24: Isometric view renders of the cruise condition optimised concepts (250pax, 7000 km)

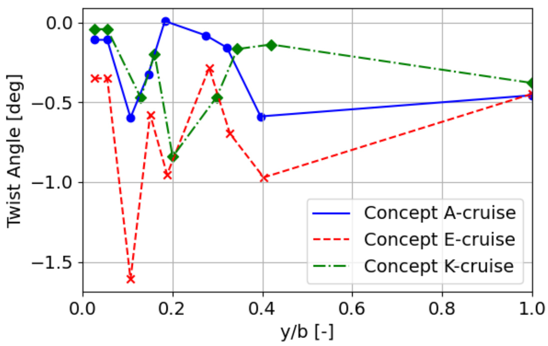

Figure 5.25: Twist angle distribution of the cruise condition optimised BWB concepts (250pax, 7000 km)

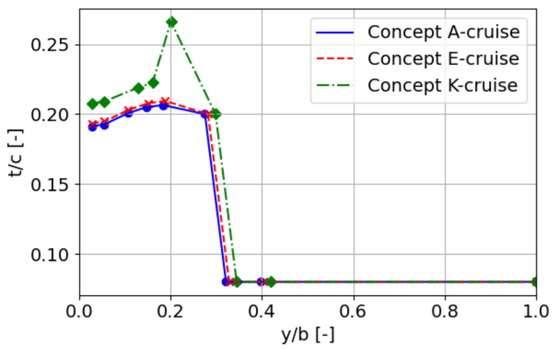

Figure 5.26: Thickness to chord ratio distribution of the cruise condition optimised BWB concepts (250pax, 7000 km)

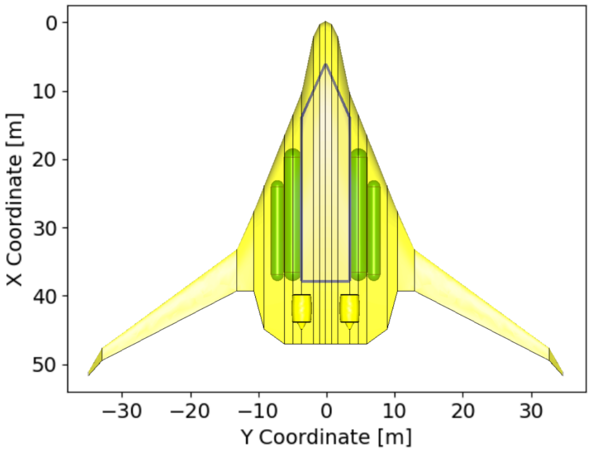

(a) BWB variant A-cruise

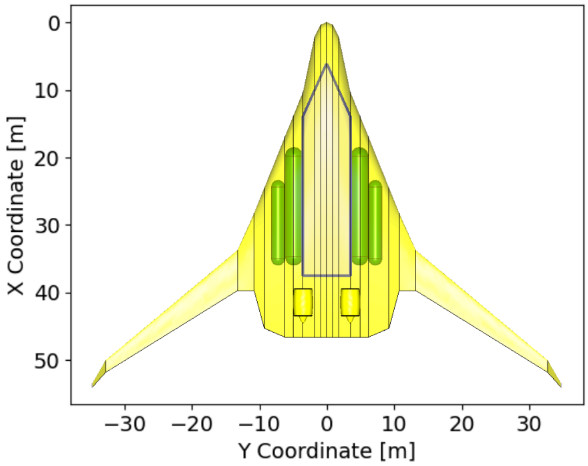

(b) BWB variant E-cruise

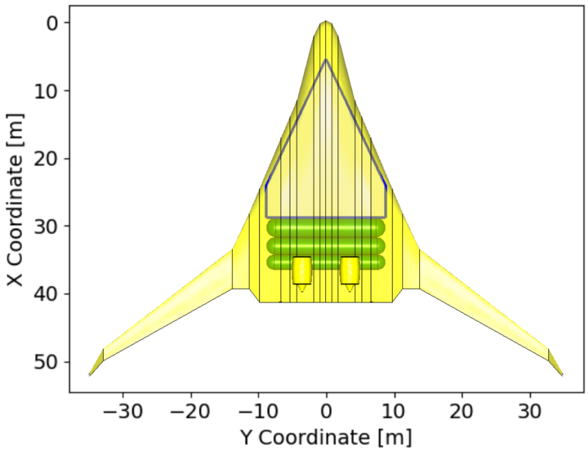

(c) BWB variant K-cruise

Figure 5.27: Planform diagrams of the cruise condition optimised concepts (250pax, 7000 km)

6
Conclusions & Recommendations

6.1. Conclusions

In this work the effect of different cabin and fuel tank layouts of hydrogen combustion BWB concepts on their aircraft level performance has been researched. It is clear that the multidisciplinary nature of LH_2 BWB concepts results in complex interactions between the different disciplines. To evaluate the sensitivity of the aircraft level performance metrics to design inputs and optimise concepts according to those metrics a conceptual design tool for LH_2 BWBs is created using the ParaPy Python package. This design tool includes a flexible parametric model that can define a large variety of BWB concepts with a limited number of inputs and generates the concepts automatically based on those inputs. The tool automatically generates the aircraft geometry and is able to output renders of the concepts. The design tool has verified and validated analysis models and methods with sufficient fidelity for the purpose of the study. The limitations of the design tool are taken into account when interpreting results from the tool. Finally, the design tool is able to compute the performance metric sensitivities and optimise BWB concepts within a reasonable computational time.

To evaluate different cabin layouts three different exit options were considered. Exit option 1 has additional doors at the leading edge of the cabin and no rear doors, exit option 2 has ventral exits at the rear of the cabin and exit option 3 imposes a sidewall length constraint on the cabin. In the planform optimisation it is found that concepts with narrow cabins are the best performing concepts. For a capacity of 350 passengers and a design cruise range of 10 000 km a cabin with exit option 1 (additional LE doors) and 3 cabin bays resulted in the lowest fuel burn for the design mission. This concept has roughly 45 % of the hydrogen fuel next to the cabin. For a capacity of 250 passengers and a design cruise range of 7000 km a cabin with exit option 2 (ventral exits) and 3 cabin bays resulted in the lowest fuel burn. This optimal concept has roughly 40 % of the hydrogen fuel next to the cabin. This means for both TLR points a cabin with 3 bays and just under half of the fuel next to the cabin yielded the optimal fuel burn for the respective design missions. The optimal concepts all had a large cabin leading edge sweep angle (this sweep angle also applies to the outer centerbody and transition region) of around 66°. For both TLR points exit option 3 (sidewall length constraint) resulted in the highest fuel burn.

The spread in performance between the best and worst performing concepts is evaluated as well. All the cabin designs resulted in a feasible concept according to the performance constraints set in this work. For the 350 passenger TLR point the difference in fuel burn between the best and worst exit options (so between their respective optimal concepts) is found to be 3.6 %. For the 250 passenger TLR point this difference is 1.3 %. When considering the spread in fuel burn between the absolute best and worst concepts (considering the optimised concepts for all the cabin designs), a larger spread in fuel burn is observed for the 350 passenger concepts than for the 250 passenger concepts. The largest difference in maximum L/D that is observed is 2 %, which means the spread in maximum L/D is smaller between the concepts. This largest difference of 2 % is observed for the 350 passenger BWB concepts. In terms of OEM the differences are higher, which is caused by the concepts with wide cabins having a significantly higher cabin mass. The largest difference observed here is 8.4 %, also for the 350 passenger concepts. As the largest differences in performance are observed for the 350 passenger concepts, the internal layout seemingly has a larger effect on the performance of those concepts, compared to the 250 passenger concepts. It can also be concluded that the internal layout has a significant effect on the fuel burn and OEM of long range hydrogen BWBs, but a smaller effect on the maximum L/D.

When optimising the cruise conditions for minimum fuel burn high optimal cruise altitudes are found, which is due to the low wing loading of the BWB concepts. This low wing loading causes lower lift coefficients than the optimal lift coefficient for maximum L/D. Flying higher means the cruise lift coefficient is increased, closer to the optimum. For the 250 passenger concepts the optimal cruise altitude is higher (48 000 ft, which is on the bound set during the optimisation) than for the 350 passenger concepts (41 000 - 46 000 ft). For both TLR points a high cruise Mach number of 0.84 is found to be the optimum, which is on the bound set during the optimisation. It must be noted that due to limitations of the model those results give an indication of what the optimal cruise conditions are. The wave drag estimation used in this work has limitations, meaning the Mach number in the optimisations is limited to 0.84. For the cruise altitude, cabin pressurisation, time to climb and engine efficiency effects are not taken into account. For the 350 passenger concepts optimisation of the cruise conditions resulted in a reduction in fuel burn of around 10 % for all three exit options, compared to the planform optimised concepts flying at constant cruise conditions. For the 250 passenger concepts this reduction is found to be almost 20 % for all three exit options. For the 250 passenger concepts a larger reduction in fuel burn is therefore expected when optimising the cruise conditions. The spread in fuel burn between the absolute best and worst designs after the cruise condition optimisations is also evaluated. For the 350 passenger TLR point the spread is 18.4 %, while for the 250 passenger TLR point the spread is 8.5 %. The difference in L/D of the optimal concepts for each exit option did not change significantly compared to the planform optimised concepts. The maximum L/D difference for the 250 passenger concepts increased slightly, while the difference in OEM decreased. For the 350 passenger concepts the differences in OEM and L/D are comparable. Based on this it can be concluded that the spread in performance does not change significantly when optimising the cruise conditions.

The sensitivities of the performance metrics (OEM, maximum L/D, cruise L/D, fuel burn and static margin) to the planform design inputs of the concepts are also evaluated. This is done for three BWB variants with drastically different fuel tank distributions, to also evaluate any internal layout effects on the sensitivity. Out of the design variables considered it is found that the cabin leading edge sweep angle has the largest effect on all the performance metrics, for all the BWB variants. For the side tank variant the magnitude of the sensitivities is the largest. For a 10 % change in the planform parameters the sensitivity of all the metrics have a magnitude of 3 to 6 %, while this is around 2 % for the mixed fuel variant and around 5 % for the aft fuel variant. For all the variants the static margin has a large sensitivity to the cabin sweep angle. The nature of the L/D and OEM sensitivities is different between the variants. The side fuel and mixed fuel variants show the same interactions, however the aft fuel variant shows different interactions. The effects of different cabin sweep angles are governed by changes in wave drag for the aft fuel variant, with only a small effect on OEM (while OEM effects are larger for the other two variants). Due to the uncertainty in the wave drag estimation method the sensitivities of the aft fuel performance metrics to the cabin sweep angle are also evaluated when excluding the wave drag. This resulted in similar interactions as the other two variants.

The design variable having the second largest sensitivity for all three variants is found to be the outer wing leading edge sweep angle. For all three variants the magnitude of the sensitivities of the OEM and cruise L/D to the outer wing sweep angle is around 1 %. The static margin sensitivity is around 0.5 %. The sensitivity of the fuel mass is not larger than 0.5 %. The magnitude of the sensitivities to the outer wing thickness is comparable to those of the outer wing sweep angle, except for the static margin. This sensitivity is very low. The side fuel ratio has a large effect on the performance metrics as well, with sensitivities as large as 5 % for a change in side fuel ratio of 10 % with respect to the baseline ratio. The effect of the tank gravimetric efficiency on the performance metrics is as expected. A lower gravimetric efficiency results in a higher OEM and fuel mass. On the other hand, as the required cruise lift coefficient increases, the cruise lift coefficient increases causing a higher cruise L/D for lower gravimetric efficiencies. Airfoil section twist angle changes of 2° resulted in a large sensitivity of the cruise L/D to those twist angles, with sensitivities around 1 to 2.5 %. The sensitivity of the static margin to the twist angles is small (< 0.05 %). It is clear the cabin leading edge sweep angle and side fuel ratio are crucial design parameters for the performance of hydrogen BWBs. Both those parameters influence the shape of the centerbody, while the wave drag over the centerbody is neglected in this work. It is therefore hard to draw conclusions on the sensitivity of those parameters with a high level of certainty. For this a high fidelity analysis of the wave drag would be required.

The effect of changing the cruise conditions is identified in this work as well. It is found that the cruise altitude has a very large effect on the cruise L/D, with sensitivities as large as 11 % for a change in altitude of 3000 ft. The sensitivity of the fuel burn to the cruise altitude is estimated to be as high as 9 %. The effects of the altitude on the cruise lift coefficient and the maximum L/D amplify each other, resulting in large changes in cruise L/D and fuel mass. The sensitivity of the cruise L/D to the cruise Mach number is lower, with magnitudes as high as 5.5 %. The cruise L/D and velocity effects on the fuel burn are conflicting, meaning the fuel mass sensitivity to the cruise Mach number is lower. Sensitivities not higher than 3.5 % are computed. It can be concluded that optimising the cruise altitude is crucial for hydrogen BWBs, due to the low wing loading of the concepts. This causes the concepts to fly at lift coefficients considerably lower than the optimal lift coefficient.

6.2. Recommendations

As explained in section 3.10, a number of assumptions have been made in this work. Based on these assumptions several recommendations for future work can already be made. Firstly, including the low speed aerodynamic characteristics of the BWB concepts can impose limits on the design variables that are based on physical phenomena. A clear example would be the cabin leading edge sweep angle, which is now bound with a maximum value based on literature. Including the low speed performance could impose a physics based limit on this variable. Another limitation resulting from the aerodynamic analysis method in this work is the wave drag estimation. No dedicated low fidelity wave drag estimation methods exist for the centerbody and transition region of a BWB aircraft. The creation of such a low fidelity method specifically for BWBs could aid tremendously in future conceptual studies on BWB aircraft, especially in designing the centerbody.

Generally, more detailed modelling of several disciplines considered in this work can improve the quality of the results. This includes a time integration based mission analysis, detailed engine model, inclusion of the lateral and dynamic stability characteristics of the BWB concepts, detailed pressure evolution in the hydrogen tanks and effects of the cabin pressurisation on the cabin structural weight. The detailed engine model, time integration mission analysis and cabin pressurisation effects can cause significant improvements in the quality of the cruise condition optimisation results. Modelling and placement of smaller components in the interior of the concepts is also recommended. Examples of these smaller components are the landing gear and balance of plant components for the hydrogen propulsion system. A detailed pressure evolution of the tanks could provide a better physical basis for the sizing of the insulation layer, as in this work it is sized based on a required boil-off rate which is determined based on data for a tank with a dormancy time of 12 hours.

In this work it became clear no validated low fidelity methods exist for estimating the structural weight of the regions of the centerbody where hydrogen tanks are placed. To aid in future conceptual work on hydrogen BWB aircraft the creation and validation of a low fidelity method to estimate the structural weight of those parts of a BWB aircraft is highly recommended.

As only cylindrical tanks with hemispherical end caps are considered in this work, it is recommended to research other shapes in future work, such as oval tanks. Splitting of the hydrogen tanks is also not considered in this work. Constraints on the shift in center of gravity during flight can result in tank splitting being required. Additionally, tank splitting can in some cases result in an improvement in tank gravimetric efficiency. In this work the tank diameters are determined based on the cabin height (including cargo hold) and an outer tank region wall height. In future work it is recommended to investigate the effect of increasing this height. On the one hand it is expected this would lead to a thicker centerbody, however the gravimetric efficiency will improve. It is expected a balance between those two effects would be found.

For the optimisation of the planform parameters only a limited number of design variables were considered, to reduce computational times. For future work it is recommended to expand the optimisation by including more design variables, such as the outer wing span, outer wing taper ratio, outer wing thickness and the height of the outboard wall of the side tank region. Airfoil profile optimisations are also recommended. Another concession that was made in the optimisations is the range being maximised for a constant fuel mass, after which the Class 1 – Class 2 iterations are performed one time to find the new fuel mass for the design range. It is expected more optimal results can be obtained if the

Class 1 – Class 2 iterations are performed for each function evaluation, with the objective to minimise the fuel mass for a certain design range.

Bibliography

[1] NASA, “Carbon Dioxide,” 2025, https://climate.nasa.gov/vital-signs/carbon-dioxide/?intent=121 [Last accessed on 13-03-2025].

[2] NASA, “Global Temperature,” 2024, https://climate.nasa.gov/vital-signs/global-temperature/?intent=121 [Last accessed on 13-03-2025].

[3] EUROCONTROL, “EUROCONTROL Data Snapshot # on CO2 emissions by flight distance,” 2021, https://www.eurocontrol.int/publication/eurocontrol-data-snapshot-co2-emissions-flight-distance [Last accessed on 13-05-2025].

[4] H. Ritchie, “What share of global CO2 emissions come from aviation?” 2024, https://ourworldindata.org/global-aviation-emissions [Last accessed on 13-03-2025].

[5] EUROCONTROL, “EUROCONTROL Aviation Long-Term Outlook: Flights and CO2 emissions forecast 2024 – 2050,” 2024, https://www.eurocontrol.int/sites/default/files/2024-12/eurocontrol-aviation-long-term-outlook-flights-co2-forecast-2024-2050.pdf [Last accessed on 13-03-2025].

[6] S. Boggia and A. Jackson, “Some Unconventional Aero Gas Turbines Using Hydrogen Fuel,” in *ASME Turbo Expo 2002: Power for Land, Sea, and Air*, Amsterdam, The Netherlands, 2002, pp. 683–690.

[7] D. Brewer, *Hydrogen Aircraft Technology*. Boca Raton, FL, USA: CRC Press, 1991.

[8] E. J. Adler and J. R. Martins, “Hydrogen-powered aircraft: Fundamental concepts, key technologies, and environmental impacts,” *Progress in Aerospace Sciences*, vol. 141, p. 100922, 2023.

[9] D. Roman, J. Allen, and R. Liebeck, “Aerodynamic design challenges of the Blended-Wing-Body subsonic transport,” in *18th Applied Aerodynamics Conference*, Denver, CO, USA, 2000, p. 4335.

[10] R. H. Liebeck, “Design of the Blended Wing Body Subsonic Transport,” *Journal of Aircraft*, vol. 41, no. 1, pp. 10–25, 2004.

[11] N. Qin, A. Vavalle, A. Le Moigne, M. Laban, K. Hackett, and P. Weinerfelt, “Aerodynamic considerations of blended wing body aircraft,” *Progress in Aerospace Sciences*, vol. 40, no. 6, pp. 321–343, 2004.

[12] J. I. Hileman, Z. S. Spakovszky, M. Drela, M. A. Sargeant, and A. Jones, “Airframe Design for Silent Fuel-Efficient Aircraft,” *Journal of Aircraft*, vol. 47, no. 3, pp. 956–969, 2010.

[13] NACRE, “Final Activity Report 2005 – 2010,” Sixth Framework programme Priority 4 Aeronautics and Space, Technical Report, 2011.

[14] D. Paulus, T. Salmon, B. Mohr, C. Roessler, Ö. Petersson, F. Stroscher, H. Baier, and M. Hornung, “Configuration selection for a 450-passenger ultraefficient 2020 aircraft,” *Progress in Flight Dynamics, Guidance, Navigation, Control, Fault Detection, and Avionics*, vol. 6, pp. 601–618, 2013.

[15] M. Kozek and A. Schirrer, “Modeling and control for a blended wing body aircraft,” *Advances in industrial control*, pp. 1–308, 2015.

[16] M. Smith, “Design of a Long Range Hydrogen Powered Transport,” Ph.D. dissertation, San Jose State University, 2016.

[17] S. Karpuk, Y. Ma, and A. Elham, "Design Investigation of Potential Long-Range Hydrogen Combustion Blended Wing Body Aircraft with Future Technologies," *Aerospace*, vol. 10, no. 6, p. 566, 2023.

[18] E. J. Adler and J. R. R. A. Martins, "Blended Wing Body Configuration for Hydrogen-Powered Aviation," *Journal of Aircraft*, vol. 61, no. 3, pp. 887–901, 2024.

[19] J. L. Chan, Y. Sun, and H. Smith, "Conceptual Designs of Blended Wing Body Aircraft for the Application of Alternative Fuels," in *AIAA AVIATION FORUM AND ASCEND 2024*, Las Vegas, NV, USA, 2024, p. 3989.

[20] O. C. V. Chung, K. Alsamri, J. L. Huynh, and J. Brouwer, "Design Methodology of Hydrogen Solid Oxide Fuel Cells Propulsion System in Blended Wing Body Aircraft," in *AIAA AVIATION FORUM AND ASCEND 2024*, Las Vegas, NV, USA, 2024, p. 3664.

[21] E. Nguyen Van, J. Gauvrit-Ledogar, C. Julien, B. Paluch, J. L. Ruan, and F. Moens, "Impact of hydrogen fuel on overall design of transport aircraft," in *34th Congress of the International Council of the Aeronautical Sciences*, Florence, Italy, 2024.

[22] S. Patel, E. Ragauss, J. Ahuja, J. C. Gladin, and D. N. Mavris, "Development of a Regional Blended Wing Body Aircraft with Distributed Hybrid Hydrogen-Electric Propulsion," in *AIAA SCITECH 2024 Forum*, Orlando, FL, USA, 2024, p. 0282.

[23] S. S. Jagtap, P. R. Childs, and M. E. Stettler, "Conceptual design-optimisation of a subsonic hydrogen-powered long-range blended-wing-body aircraft," *International Journal of Hydrogen Energy*, vol. 96, pp. 639–651, 2024.

[24] R. Wood and X. Bauer, "Flying wings/flying fuselages," in *39th Aerospace Sciences Meeting and Exhibit*, Reno, NV, USA, 2001, p. 311.

[25] IEEE Aerospace and Electronic Systems Society, "History Column: Horten Ho-229," 2021, https://ieee-aess.org/post/blog/history-column-horten-ho-229 [Last accessed on 19-11-2024].

[26] Leigh-Howarth, Jake, "Northrop YB-35/XB-35 – The Flying Wing Failure," 2023, https://planehistoria.com/northrop-yb-35-xb-35/ [Last accessed on 19-11-2024].

[27] National Museum of the United States Air Force, "Northrop YB-49 Fact Sheet," 2024, https://www.nationalmuseum.af.mil/Visit/Museum-Exhibits/Fact-Sheets/Display/Article/858861/northrop-yb-49/ [Last accessed on 19-11-2024].

[28] United States Air Force, "B-2 Spirit Fact Sheet," 2024, https://www.af.mil/About-Us/Fact-Sheets/Display/Article/104482/b-2-spirit/ [Last accessed on 19-11-2024].

[29] P. Okonkwo and H. Smith, "Review of evolving trends in blended wing body aircraft design," *Progress in Aerospace Sciences*, vol. 82, pp. 1–23, 2016.

[30] R. Maier, "ACFA 2020 Summary of Achievements," *EADS Innovation Works, TR Deliverable D*, 2014.

[31] Y. Liu, "Assessment of surface roughness for a 'silent' aircraft," *The Aeronautical Journal*, vol. 117, no. 1189, pp. 283–298, 2013.

[32] O. V. Salazar, J. Weiss, and F. Morency, "Development of blended wing body aircraft design," in *CASI 62nd Aeronautics Conference and AGM*, Montréal, Canada, 2015.

[33] E. Torenbeek, *Advanced aircraft design: conceptual design, analysis and optimization of subsonic civil airplanes.* John Wiley & Sons, 2013.

[34] A. Sgueglia, "Sizing and optimisation priorities applied to a Blended Wing-Body with distributed electric ducted fans," PhD Thesis, Université de Toulouse, 2019.

[35] R. Liebeck, "Blended wing body design challenges," in *AIAA International Air and Space Symposium and Exposition: The Next 100 Years*, Dayton, OH, USA, 2003, p. 2659.

[36] J. Ehlers, D. Niedermeier, and D. Leißling, "Verification of a flying wing handling qualities analysis by means of in-flight simulation," in *AIAA Atmospheric Flight Mechanics Conference*, Portland, OR, USA, 2011, p. 6540.

[37] S. Tiwari, M. J. Pekris, and J. J. Doherty, "A review of liquid hydrogen aircraft and propulsion technologies," *International Journal of Hydrogen Energy*, vol. 57, pp. 1174–1196, 2024.

[38] D. Verstraete, "The Potential of Liquid Hydrogen for long range aircraft propulsion," Ph.D. dissertation, Cranfield University, 2009.

[39] J. Huete and P. Pilidis, "Parametric study on tank integration for hydrogen civil aviation propulsion," *International Journal of Hydrogen Energy*, vol. 46, no. 74, pp. 37 049–37 062, 2021.

[40] G. Dannet, "Integration of cryogenic tanks and fuel cells for future hydrogen-powered aircraft," Master's thesis, Linköping university, 2021.

[41] P. Rompokos, A. Rolt, D. Nalianda, T. Sibilli, and C. Benson, "Cryogenic Fuel Storage Modelling and Optimisation for Aircraft Applications," in *ASME Turbo Expo 2021: Turbomachinery Technical Conference and Exposition*, Virtual, Online, 2021, p. V006T03A001.

[42] T. W. Reynolds and S. Weiss, "Experimental study of foam-insulated liquified-gas tanks," National Advisory Committee for Aeronautics, Cleveland, OH, USA, Technical Report RM E56K08a, 1957.

[43] G. Onorato, P. Proesmans, and M. F. M. Hoogreef, "Assessment of hydrogen transport aircraft: Effects of fuel tank integration," *CEAS Aeronautical Journal*, vol. 13, no. 4, pp. 813–845, 2022.

[44] D. Pratt, K. Allwine, and P. Malte, "Hydrogen as a turbojet engine fuel- technological, economical and environmental impact," in *2nd International Symposium on Air Breathing Engines*, Sheffield, England, 1974.

[45] R. Mulready, "Liquid hydrogen engines," *Technology and Uses of Liquid Hydrogen*, pp. 149–180, 1964.

[46] R. Witcofski, "Potentials and problems of hydrogen fueled supersonic and hypersonic aircraft," in *Proceedings of the 7th Intersociety Energy Conversion Engineering Conference*, San Diego, CA, U.S.A, 1972, pp. 1349–1354.

[47] Airbus, "Airbus and CFM International to pioneer hydrogen combustion technology," 2022, https://www.airbus.com/en/newsroom/press-releases/2022-02-airbus-and-cfm-international-to-pioneer-hydrogen-combustion [Last accessed on 22-11-2024].

[48] G. Corchero and J. L. Montañés, "An approach to the use of hydrogen for commercial aircraft engines," *Proceedings of the Institution of Mechanical Engineers, Part G: Journal of Aerospace Engineering*, vol. 219, no. 1, pp. 35–44, 2005.

[49] J. Brand, S. Sampath, F. Shum, R. Bayt, and J. Cohen, "Potential Use of Hydrogen In Air Propulsion," in *AIAA International Air and Space Symposium and Exposition: The Next 100 Years*, Dayton, OH, USA, 2003, p. 2879.

[50] G. Dahl, "Engine control and low-NOx combustion for hydrogen fuelled aircraft gas turbines," *International Journal of Hydrogen Energy*, vol. 23, no. 8, pp. 695–704, 1998.

[51] D. Maniaci, "Relative Performance of a Liquid Hydrogen-Fueled Commercial Transport," in *46th AIAA Aerospace Sciences Meeting and Exhibit*, Reno, NV, USA, 2008, p. 152.

[52] H. Abedi, C. Xisto, I. Jonsson, T. Grönstedt, and A. Rolt, "Preliminary Analysis of Compression System Integrated Heat Management Concepts Using LH2-Based Parametric Gas Turbine Model," *Aerospace*, vol. 9, no. 4, p. 216, 2022.

[53] J. Gauvrit-Ledogar, A. Tremolet, F. Moens, M. Méheut, S. Defoort, R. Liaboeuf, F. Morel, and B. Paluch, "Multidisciplinary design analysis and optimization process dedicated to blended wing body configurations," in *33rd Congress of the International Council of the Aeronautical Sciences*, Stockholm, Sweden, 2022.

[54] T. Nieuwenhuizen, "Conceptual Design of a Flying V Aircraft," Ph.D. dissertation, TU Delft, 2021.

[55] F. Faggiano, "Aerodynamic Design Optimization of a Flying V Aircraft," Master's thesis, TU Delft, 2016.

[56] V. W. Versprille, "Aerodynamic Shape Optimization of a Liquid-Hydrogen-Powered Blended-Wing-Body," Ph.D. dissertation, TU Delft, 2022.

[57] Drela, M. and Youngren, H., "AVL Aerodynamic Analysis," 2022, https://web.mit.edu/drela/Public/web/avl/ [Last accessed on 27-11-2024].

[58] M. Brown, "Conceptual Design of Blended Wing Body Airliners," Ph.D. dissertation, TU Delft, 2017.

[59] F. Moens, "A L0 Aerodynamic Model for Aircraft Multidisciplinary Design and Optimization Process," in *56th 3AF International Conference AERO2022*, Toulouse, France, 2022.

[60] J. Roskam, *Airplane design. 6: Preliminary calculation of aerodynamic, thrust and power characteristics*. Lawrence, KS, USA: DARcorporation, 2008.

[61] D. Howe and G. Rorie, *Aircraft conceptual design synthesis*. Professional Engineering Publishing London, UK, 2000.

[62] C. A. Kays, "Multidisciplinary methods for performing trade studies on blended wing body aircraft," Ph.D. dissertation, Massachusetts Institute of Technology, 2013.

[63] R. S. Shevell and F. P. Bayan, "Development of a method for predicting the drag divergence mach number and the drag due to compressibility for conventional and supercritical wings," Stanford University, Stanford, CA, USA, Technical Report SUDAAR-522, 1980.

[64] R. C. Feagin and W. D. Morrison, "Delta method, an empirical drag buildup technique," Lockheed, Burbank, CA, USA, Technical Report N79-17801, 1978.

[65] H. Hefazi, A. Vore, and D. Dougherty, "High lift flap design and testing for a tailless transport aircraft," in *51st AIAA Aerospace Sciences Meeting including the New Horizons Forum and Aerospace Exposition*. Grapevine (Dallas/Ft. Worth Region), TX, USA: American Institute of Aeronautics and Astronautics, 2013.

[66] E. Torenbeek, *Synthesis of Subsonic Airplane Design*. Delft, The Netherlands: Springer, 1982.

[67] J. Roskam, *Airplane design. 5: Component weight estimation*. Lawrence, KS, USA: DARcorporation, 2003.

[68] K. Bradley, "A Sizing Methodology for the Conceptual Design of Blended-Wing-Body Transports," Ph.D. dissertation, George Washington University, 2004.

[69] D. Raymer, *Aircraft design: a conceptual approach*. American Institute of Aeronautics and Astronautics, Inc., 1992.

[70] D. Wells, B. Horvath, and L. McCullers, "The Flight Optimization System Weights Estimation Method," NASA, Hampton, VA, USA, Technical Report NASA/TM-2017-219627/VOL.1, 2017.

[71] D. Howe, “Blended wing body airframe mass prediction,” *Proceedings of the Institution of Mechanical Engineers, Part G: Journal of Aerospace Engineering*, vol. 215, no. 6, pp. 319–331, 2001.

[72] E. S. Hendricks and J. S. Gray, “pyCycle: A tool for efficient optimization of gas turbine engine cycles,” *Aerospace*, vol. 6, no. 8, p. 87, 2019.

[73] B. Cantwell, *Aircraft and Rocket Propulsion.* Stanford, CA, USA: Stanford University, 2022.

[74] N. Tarbah, “Developing a Framework for the Design of Hydrogen Fuel Cell Supply Architectures,” Ph.D. dissertation, TU Delft, 2024.

[75] G. Palaia, K. Abu Salem, and E. Carrera, “Preliminary Performance Analysis of Medium-Range Liquid Hydrogen-Powered Box-Wing Aircraft,” *Aerospace*, vol. 11, no. 5, p. 379, 2024.

[76] J. Roskam, *Airplane design. 1: Preliminary sizing of airplanes.* Lawrence, KS, USA: DARcorporation, 2005.

[77] T. W. Lukaczyk, A. D. Wendorff, M. Colonno, T. D. Economon, J. J. Alonso, T. H. Orra, and C. Ilario, “Suave: an open-source environment for multi-fidelity conceptual vehicle design,” in *16th AIAA/ISSMO Multidisciplinary Analysis and Optimization Conference*, Dallas, TX, USA, 2015, p. 3087.

[78] L. Jenkinson, P. Simpkin, and D. Rhodes, *Civil Jet Aircraft Design.* American Institute of Aeronautics and Astronautics, Inc., 1999.

[79] EASA, *Easy Access rules for Large Aeroplanes (CS-25).* European Union, 2023.

[80] Airbus S.A.S., “A350 Aircraft Characteristics Airport and Maintenance Planning,” 2024, https://ourworldindata.org/global-aviation-emissions [Last accessed on 14-03-2025].

[81] R. T. Kawai, “Acoustic prediction methodology and test validation for an efficient low-noise hybrid wing body subsonic transport,” NASA, Hampton, VA, USA, Technical Report NF1676L-14465, 2011.

[82] J. van Dommelen and R. Vos, “Conceptual design and analysis of blended-wing-body aircraft,” *Proceedings of the Institution of Mechanical Engineers, Part G: Journal of Aerospace Engineering*, vol. 228, no. 13, pp. 2452–2474, 2014.

[83] J. Roskam, *Airplane design. 3: Layout design of cockpit, fuselage, wing and empennage: cutaways and inboard profiles.* Lawrence, KS, USA: DARcorporation, 2002.

[84] Boeing, *727 Airplane Characteristics: Airport Planning.* Boeing, 1985.

[85] K. Chen, X. Wang, P. Li, and J. Xie, “Modeling and evaluating passenger evacuation and risk in blended wing body aircraft using continuous displacement agents,” *Discover Applied Sciences*, vol. 7, no. 1, pp. 1–17, 2025.

[86] O. Gur, W. H. Mason, and J. A. Schetz, “Full-Configuration Drag Estimation,” *Journal of Aircraft*, vol. 47, no. 4, pp. 1356–1367, 2010.

[87] W. Mason, “Analytic models for technology integration in aircraft design,” in *Aircraft design, systems and operations conference*, 1990, p. 3262.

[88] G. R. Inger, “Application of Oswatitsch’s theorem to supercritical airfoil drag calculation,” *Journal of Aircraft*, vol. 30, no. 3, pp. 415–416, 1993.

[89] M. A. Sargeant, T. P. Hynes, W. R. Graham, J. I. Hileman, M. Drela, and Z. S. Spakovszky, “Stability of Hybrid-Wing-Body-Type Aircraft with Centerbody Leading-Edge Carving,” *Journal of Aircraft*, vol. 47, no. 3, pp. 970–974, 2010.

[90] Z. Lyu and J. R. R. A. Martins, "Aerodynamic Design Optimization Studies of a Blended-Wing-Body Aircraft," *Journal of Aircraft*, vol. 51, no. 5, pp. 1604–1617, 2014.

[91] M. Bauccio, *ASM Metals Reference Book*. Materials Park, OH, USA: ASM International, 1993.

[92] M. Aziz, "Liquid hydrogen: A review on liquefaction, storage, transportation, and safety," *Energies*, vol. 14, no. 18, p. 5917, 2021.

[93] A. J. Colozza and L. Kohout, "Hydrogen storage for aircraft applications overview," NASA, Brook Park, OH, USA, Technical Report NASA/CR-2002-211867, 2002.

[94] Jane's UK Group Ltd., "Janes Database," 2025, https://customer.janes.com/ [Last accessed on 26-02-2025].

[95] P. P. C. Okonkwo, "Conceptual design methodology for blended wing body aircraft," Ph.D. dissertation, Cranfield University, 2016.

[96] F. Healy, H. Gu, D. Rezgui, and J. Cooper, "Conceptual design of hydrogen-powered aircraft: High aspect ratio wings and floating wingtips," in *34th Congress of the International Council of the Aeronautical Sciences*. Florence, Italy: ICAS, 2024.

[97] M. Taflan, H. Smith, and J. Loughlan, "Structural sizing and mass estimation of transport aircraft wings with distributed, hydrogen, and electric propulsions," *The Aeronautical Journal*, vol. 129, no. 1333, pp. 690–716, 2025.

[98] J. Roskam, *Airplane design. 2: Preliminary configuration design and integration of the propulsion system*. Lawrence, KS, USA: DARcorporation, 2004.

[99] T. Vogeltanz, "Application for calculation of mean aerodynamic chord of arbitrary wing planform," in *International Conference of Numerical Analysis and Applied Mathematics 2015*. Rhodes, Greece: American Institute of Physics, 2016.

A
Additional Sensitivity Analysis Results

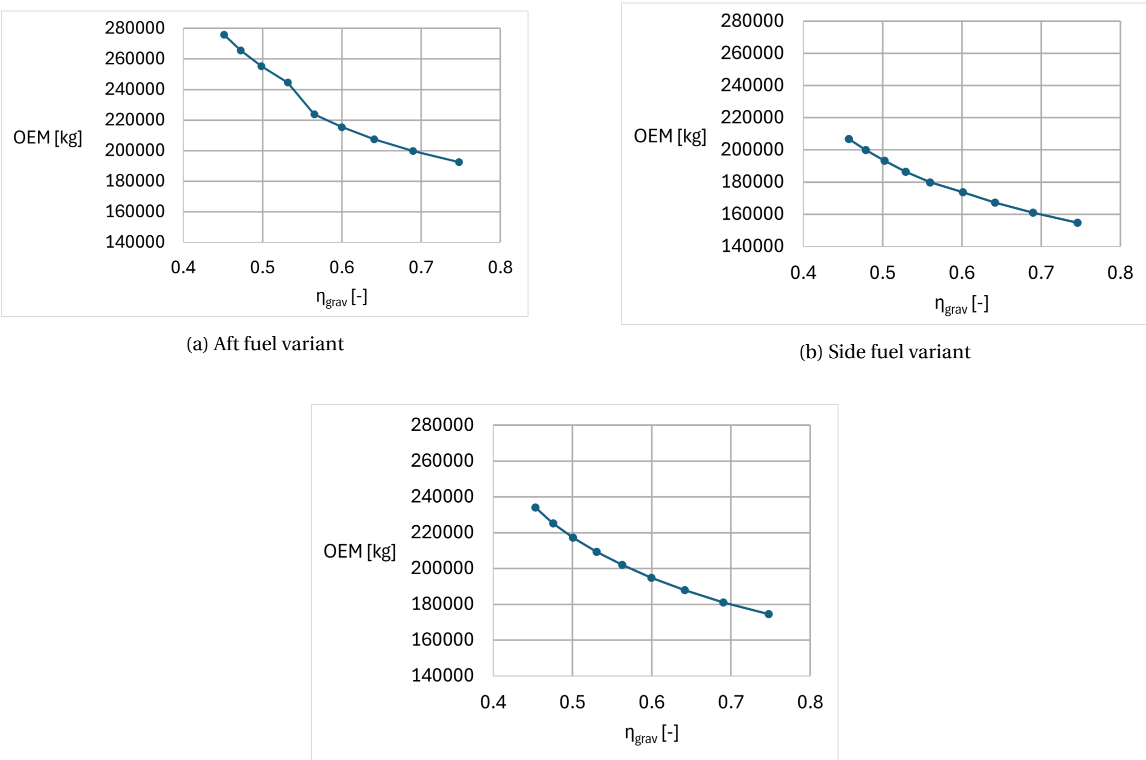

(a) Aft fuel variant

(b) Side fuel variant

(c) Mixed fuel variant

Figure A.1: OEM sensitivity to the tank gravimetric efficiency for the BWB variants

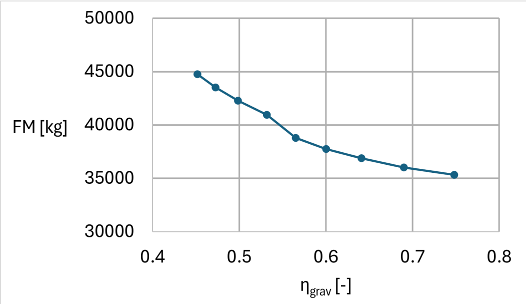

(a) Aft fuel variant

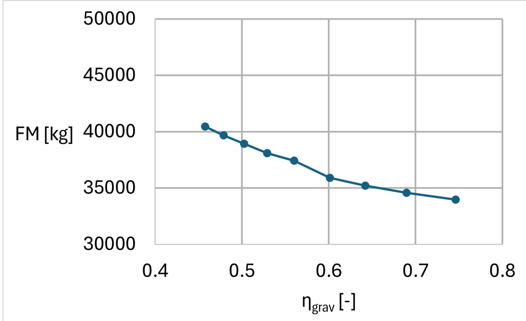

(b) Side fuel variant

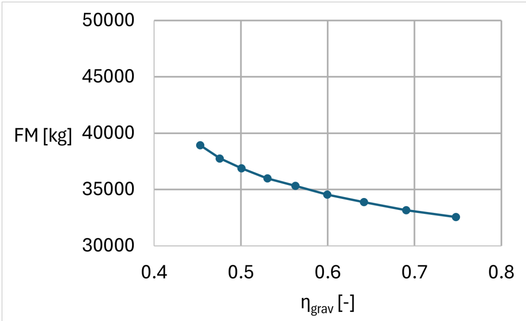

(c) Mixed fuel variant

Figure A.2: Fuel mass sensitivity to the tank gravimetric efficiency for the BWB variants

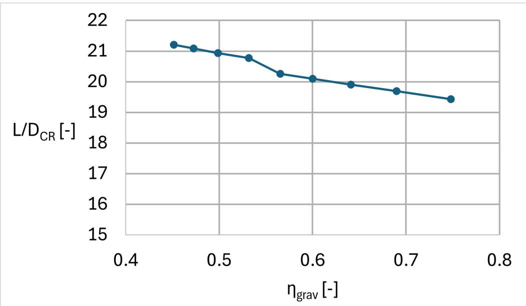

(a) Aft fuel variant

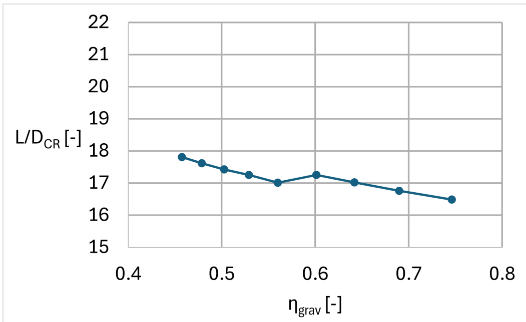

(b) Side fuel variant

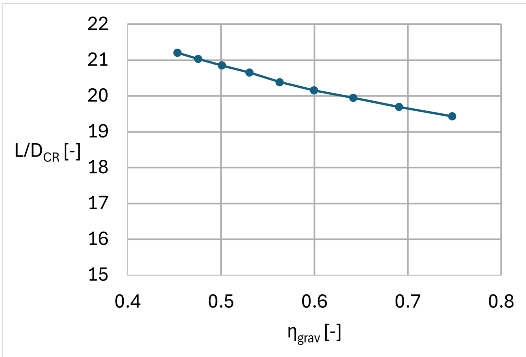

(c) Mixed fuel variant

Figure A.3: Cruise L/D sensitivity to the tank gravimetric efficiency for the BWB variants